Unconstrained Global Optimization of Molecules on Surfaces

From globally optimized structures to scanning-probe data

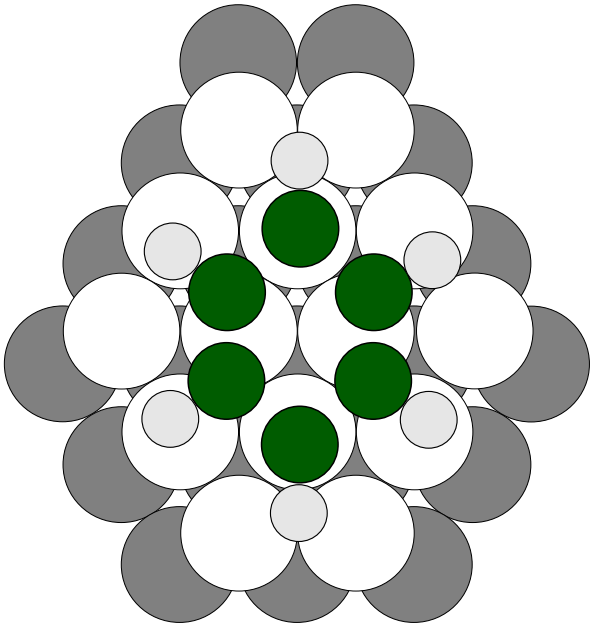

Dissertation

in partial fulfillment of the requirements for the degree
Dr. rer. nat.

of the Faculty of Mathematics and Natural Sciences at
Kiel University

submitted by
Christopher Witt

Kiel, 2020

Faculty director:	Prof. Dr. Frank Kempken
First referee:	Prof. Dr. Bernd Hartke
Second referee:	Prof. Dr. Swetlana Schauermann
Date of oral examination:	12.01.2021

Abstract

The adsorption of molecules on a surface plays a vital role in heterogeneous catalysis. For a proper unterstanding of the reaction mechanisms involved, the adsorption geometry of the molecules on the surface needs to be known. So far, experimental data from tunneling microscopes and spectroscopy, such as STM and IRAS are the main ways to obtain such knowledge. Due to the vast search space of adsorption geometries, especially for oligomers, optimizations using *ab initio* methods can be used to confirm the experimental data only if good initial guesses are available. Global optimization can serve two purposes in these situations. On the one hand it allows for a thorough investigation of the given search space, which can provide good initial guesses for subsequent high-level structural refinements. On the other hand, given a known reaction mechanism, it could also be used to find catalysts that influence e.g. the relevant bonds.

With respect to this idea the topic of this thesis is to find a local optimization method cheap enough such that the total computational cost of global optimization does not exceed availability and yet good enough that the results are meaningful to the problem at hand. With this in mind multiple force field and semiempirical methods have been tested and evaluated mainly on benzene, acetophenone and ethyl pyruvate on Pt(111) surfaces. Some other adsorbates have also been tested shortly. In addition to these global optimization results, DFT geometry optimizations of ethyl pyruvate on Pt(111) have been performed and the structures of the best adsorption geometry from global optimization and from DFT are compared. Furthermore, from the DFT data STM images have been calculated that are compared to experimental results. The theoretical and experimental STM images agree well.

Kurzzusammenfassung

Die Adsorption von Molekülen auf einer Oberfläche spielt eine essentielle Rolle in der heterogenen Katalyse. Zum vernünftigen Verständnis der involvierten Reaktionsmechanismen muss die Adsorptionsgeometrie der Moleküle auf der Oberfläche bekannt sein. Bisher sind experimentelle Daten von Tunnelmikroskopen und Spektroskopie, wie STM und IRAS, die Hauptwege solches Wissen zu erlangen. Aufgrund des großen Suchraums an Adsorptionsgeometrien, besonders für Oligomere, können *ab initio*-Methoden nur genutzt werden, wenn gute Startstrukturen verfügbar sind. Globale Optimierungsmethoden können hier Abhilfe verschaffen und unter anderem zwei Zwecken dienen. Einerseits ermöglicht sie eine gründliche Erforschung des gegebenen Suchraums, wodurch gute Startstrukturen für folgende hochqualitative Strukturoptimierungen zur Verfügung gestellt werden können. Andererseits kann sie aber beispielsweise auch bei einem bekannten Reaktionsmechanismus dazu genutzt werden Katalysatoren zu finden, die bspw. die relevanten Bindungen beeinflussen. Daraus ergibt sich als Thema dieser Dissertation das Finden einer Methode zur lokalen Optimierung, die günstig genug ist, sodass der Gesamtrechenaufwand der globalen Optimierung nicht den Rahmen sprengt und dennoch gut genug ist, sodass die Resultate bedeutungsvoll für die untersuchte Fragestellung sind. Vor diesem Hintergrund wurden mehrere Kraftfelder und Semiempiriemethoden hauptsächlich an Benzol, Acetophenon und Ethylpyruvat auf Pt(111) Oberflächen getestet und evaluiert. Zusätzlich zu diesen Resultaten der globalen Optimierung wurden Geometrieoptimierungen von Ethylpyruvat auf Pt(111) Oberflächen auf DFT-Niveau durchgeführt und mit den besten Strukturen aus der globalen Optimierung verglichen. Darüberhinaus wurden aus den DFT-Daten STM-Bilder berechnet, die mit experimentellen Daten verglichen werden. Die theoretischen und experimentellen STM-Bilder stimmen gut überein.

Contents

List of Figures

List of Tables

1 | Introduction

The elucidation of catalytic reaction mechanisms, especially in heterogeneous catalysis, has long been an interesting topic in physical chemistry [1–4]. The basic idea of catalysis is that the energy barrier of a reaction can be energetically lowered by the presence of a catalyst. In the case of a heterogeneous catalyst, this can be explained by the surface, of e.g. a metal, interacting with the reactants through adsorption. This would lower the energy barrier for the reaction towards the products, for example by weakening a specific bond in a molecule. An additional condition to a successful catalyst is that neither the reactants nor the products may bind to the catalyst too strongly. This does not mean that covalent bonds may not form, they do have to break relatively easily after the reaction, though. A schematic picture of these processes is shown in Fig. 1.1. The schema shows the uncatalyzed reaction from reactants to intermediates and then to the products. The energy barrier for this reaction, E_g is much higher than for the catalyzed reaction. The catalyzed reaction has multiple steps, all of which have lower barriers. First the reactants get adsorbed to the surface, then the catalyzed reaction happens, and finally the products are desorbed from the surface. For catalysis to occur, the correct part of a molecule must interact with the surface. It is therefore important to learn more about and understand the precise interaction between molecules and the underlying surface. Different adsorption positions on a surface obviously mean different surface environments and therefore different interactions with surface atoms. This leads to different energy barriers for different sites, such that some sites will be favored. A general schematic of possible adsorption sites on an fcc-crystal(111) surface is given by Fig. 1.2. Four distinct positions that can be differentiated between, without considering the adsorbate, are: directly on top of a surface atom (Atop), on a line between to surface atoms (Bridge), and in a triangle between three of these surface atoms (Hollow). The hollow sites can be differentiated further due to the underlying second layer. Half of the hollow sites are underlaid by an atom of the second layer (Hollow-hcp), while the other half is not (Hollow-fcc). All of these positions can interact with any part of a molecule in different ways. The number of possible adsorption positions and the number of interactable parts of a molecule can be considered as a combinatorial problem then. For the goal of finding adsorption sites for molecules of interest theoretical chemistry can supply very detailed adsorption geometries that can otherwise only be observed indirectly. Typical experimental methods of attaining information about the structure of an adsorbate are tunneling microscopy [6] and spectroscopy experiments like infrared (IR) spectroscopy [7] or Raman spectroscopy [8]. Schematic images of an STM measurement (Fig. 1.3a) and a spectroscopy (Fig. 1.3b) are shown to illustrate the

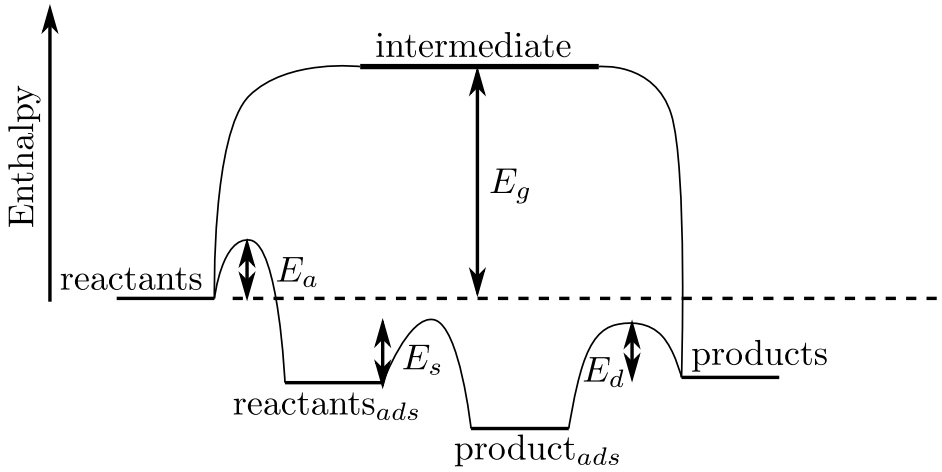

Figure 1.1: Schematic image of a surface catalyzed reaction in comparison to the equal gas phase reaction. The energy barrier (E_g) for the gas phase reaction is much higher than the barriers for the adsorption (E_a), (E_s) for the surface catalyzed reaction and (E_d) and the desorption barrier. Adapted after Ref. 5 p. 8.

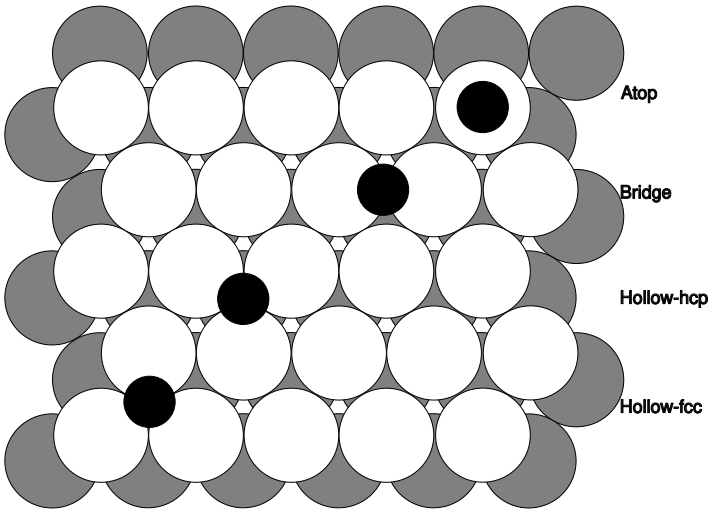

Figure 1.2: A schematic depiction of different adsorption positions on a (111) surface of an fcc-crystal. The difference between the two types of hollow sites is that there is an atom in the second layer underneath for the hollow-hcp site, but not for the hollow-fcc site.

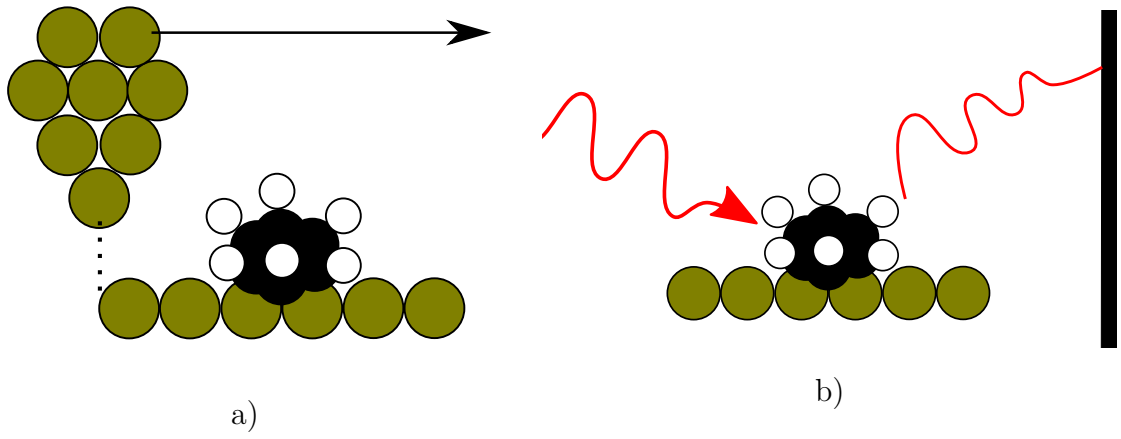

Figure 1.3: Schematic illustrations of a) STM and b) spectroscopic techniques for surface investigation. In a) a probe tip is moving across the surface, measuring the tunneling current, in b) a molecule on a surface is irradiated and the radiation coming back from the molecule is detected.

experimental side of the investigation into the adsorption of (catalytically interesting) molecules. Combining information from physical and theoretical chemistry can be highly advantageous in this field [7,9]. The main advantage of computational methods here is in the resolution, since the geometry of an adsorbed molecule and the exact part of the molecule that is interacting can be determined by theoretical calculations, while the experiments can not deliver this kind of resolution. Now, in the real world there will be a lot of molecules on a catalyst, and the temperatures allow for a wide range of motion, such that a lot of minima may be available. Finding these by standard optimization methods would at the very least be tedious due to the vast amount of possibilities. This is where global optimization can show its strength in aiding with this aim.

Global optimization[1], with its capability to find energetically low adsorption geometries, can be beneficial towards learning about the adsorption geometries of surface adsorbed molecules [10,11]. This has previously already been shown for the gas phase [12]. The supporting information to Ref. 10 contains a detailed survey of surface global optimization studies that will briefly be described and expanded upon in the following section. The following sections will give additional introductions into some of the relevant topics.

[1] A longer explanation of global optimization and specifically the methods used in this thesis are given in section 2.2.

1.1 Global Optimization approaches to molecular adsorption on surfaces

There are several different global optimization approaches that can generally be summarized into two groups:

1. Basin-Hopping (BH) or Simulated-Annealing (SA) strategies
2. Swarm-Optimization strategies and global/evolutionary algorithms (GA/EA)

Chemistry-related global optimization is mostly oriented towards finding the global minimum structure of a given system. This means finding the deepest minimum on a potential energy surface (PES) that has as many dimensions as there are degrees of freedom (DOF) in the system. The search space scales exponentially with system size. Assuming that the number of minima scales linearly with the search space, the number of minima also scales exponentially with system size. The exact scaling, however, of course almost certainly is dependent on the specific system in question. Due to this exponential scaling of search space a deterministic investigation of the entire space is not feasible and therefore non-deterministic global optimization is necessary. The BH and SA strategies are based on the idea of giving the system enough energy to cross barriers between minima and then slowly reducing the energy to trap the system in the new minimum, much like the tempering of a metal in a forge, which is where the term annealing comes from. In practice there are often Monte-Carlo-like moves involved that move one or multiple particles directly from one position to another [13, 14]. In the case of SA the calculation starts with a high temperature which is then slowly reduced. Doing this very (or infinitely) slowly, this would be guaranteed to reach the global minimum. However, this is not feasible since it would create very (or infinitely) long trajectories. For BH this is technically realized by Monte-Carlo-like moves to get out of one minimum and subsequent local optimization to find the next minimum. Doing this repeatedly, one can find a variety of minima and determine the best one among these. Additionally doing this from different starting points on the PES, the global minimum should eventually be among the ones visited. This is illustrated in Fig. 1.4. Theoretically, the global minimum does not have to be the last point in an MC optimization, it could also be visited at some point inbetween. In contrast to this, GA/EA and Swarm-Optimization strategies start from a variety of starting points on the PES in parallel and utilize this to exchange information between these points to find new ones. This is often combined with local optimization at each step to ensure that a minimum is found. More detail on these different approaches will be given in the theory section.

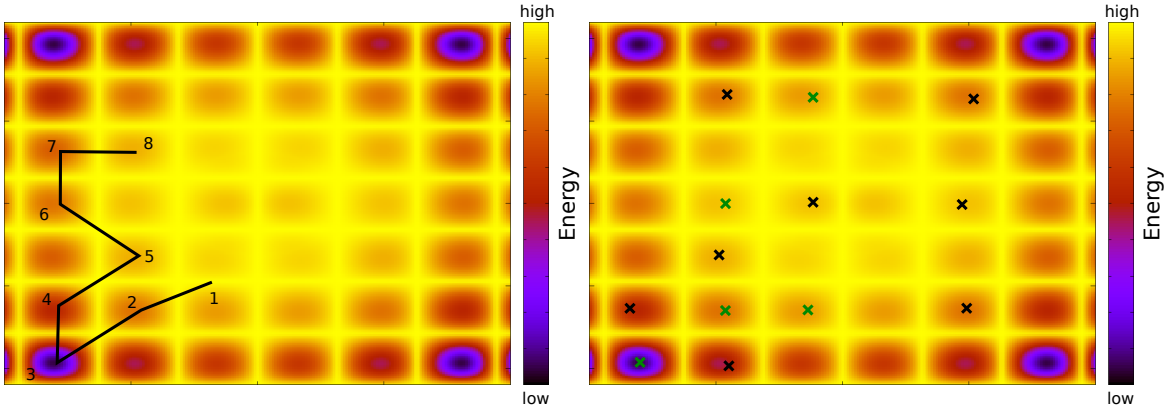

a) b)

Figure 1.4: Schematic visualization of the two optimization variants described here and in section 2.2. In a) only one starting point exists, from which different neighboring minima can be reached through MCM steps. This eventually leads to one of the global minima. In b) the black crosses represent the inital starting points, the green crosses represent the points after one iteration of recombinations. The function used as a stand-in for the PES is the Holder table function.

A short description of previous works related to this field should be given - a thorough list can be found in the supporting information of Ref. 10 and citations therein, but a short account of these shall be given here, too. Then some additional works in this area of research from recent years are added. Of the previous studies described in Ref. 10 two of them have used basin-hopping like strategies [15, 16], some others have used density functional theory (DFT) to calculate molecular structures and charges, then a force-field-molecular-dynamics (MD) to find low-energy adsorption sites and in a final step metadynamics in order to find low-energy lattices formed by the adsorbate [17, 18]. In another paper molecular assembly has been simulated with an extremely simple force field and no global optimization scheme at all [19]. Monte-Carlo (MC) methods are also employed [20–22]. MC approaches have also been used, however, with the limitation of a hexagonal lattice of adsorption positions [22]. Coarse-graining of molecules has also been applied to MD approaches, thus enabling very large time steps which allow for longer simulations which, in turn, allow for assembly to take place [23]. MC steps can also be combined with other methods named here, e.g. MC-simulated-annealing (MC-SA) [24]. Simple, very coarse force-fields have also been applied to the 2D-packing of a molecule layer on a surface [25]. Periodic DFT as a local optimization with a few different 2D-cell sizes and starting positions has also been applied [26]. *Schön et al.* compiled a list of literature regarding molecules on surfaces and classified them according to their optimization model [27]. Interestingly, none of the mentioned studies has done full global optimization on a larger number

of molecules, investigating the self-assembly of these molecules. This concludes the list of publications described in the supporting information of Ref. 10. It should be noted that Ref. 10 itself is a publication in which the self-assembly of triazatriangulene molecules on an Au(111) surface has been explored by the same types of algorithms as employed in this present work. Only a few more publications have come out in the past few years since the literature survey from Ref. 10, but those should also be mentioned here. Outside of molecular assembly of molecules on surfaces there are quite a few publications on the global optimization of metal clusters on surfaces, e.g. by *Bazhenov et al.* who optimized rhodium and platinum clusters on a zirconia(111) surface [28] using genetic algorithms (GA) in combination with projector augmented wave (PAW) DFT and effective core potentials. In a similar fashion *Sun et al.* used the grand canonical genetic algorithm (GCGA) to optimize Pt_8 clusters under hydrogen pressure on different alumina surfaces (γ-$Al_2O_3(100)$ and α-$Al_2O_3(0001)$) using multiple PAW-DFT variants with different basis set sizes [29], effectively optimizing mixed Pt_8H_x clusters. Closer to the subject *Gorbunov et al.* used a lattice gas model to describe the molecular assembly of organic monolayers of an abstract molecule, defined only by a functional group capable of forming a hydrogen bond [30]. The optimization took place using an MC method. *Su et al.* used stochastic-tunneling BH with the Dreiding force field to simulate discrete molecular dynamics of terephthalic acid on a buffer layer of stearic acid on graphene [31, 32]. The buffer layer was optimized by the same method. *Fejer* described the modeling of entire virus capsids via coarse-grained force fields using discrete molecular dynamics [33]. This is, however, just a case of molecular assembly without a surface, which is only interesting due to the system size involved. To the authors knowledge no other global optimization approaches for the assembly of molecular systems on surfaces have been published in recent years.

The global optimization approach that has been applied in this thesis is based on evolutionary algorithms, which start from multiple different points on the potential energy hypersurface (PES). For the local optimization a variety of methods have been tested during this thesis. All optimizations do, however, have a few things in common. The molecules are all fully flexible and not constrained in any way, the surface itself, however, is kept rigid. A similar approach has been applied in the already mentioned publication by *Freibert et al.* [10], the main difference here is in the employed backends (local optimization methods), since in that publication the molecule-surface interaction is only described by van-der-Waals interactions within the OPLS-aa force field (section 2.3), which appears to be a good description for the interactions of benzene on gold, where it is loosely bound, but not for benzene on platinum, where the interaction is much stronger. More details about this can be found in chapter 4.

1.2 Aim of this work

The goal of this work is to utilize Global Optimization techniques in order to find adsorption geometries and positions of molecules on surfaces. These globally optimal adsorption geometries can in turn aid in elucidating reactions that take place on heterogeneous catalytic surfaces. Since most global optimization approaches utilize a local optimization in each global optimization step, a local optimization method is required that is capable of accurately describing the qualitative properties of molecules on surfaces while not being computationally expensive. This is due to the fact that during a global optimization a large number of local optimizations have to take place. While for global optimizations of smaller gas phase clusters *ab initio* methods may be feasible [34, 35], one would have to use a rather small piece of a surface to optimize a molecule on top of it, e.g. utilizing a software capable of describing periodic systems. Using computationally cheaper methods like semi-empirical models or force fields, one can easily describe a decent piece of the surface and multiple adsorbates. With this step delivering good candidates for adsorption structures, further optimizations on a higher level of theory can follow and additional data can be extracted from these. A full workflow could have the following steps:

- Global optimizations of the molecule in question (also dimers, trimers etc.)
- Identifying probable candidates for adsorption structures and positions
- Local optimization on a higher level of theory
- Postprocessing to obtain e.g. STM or IR data
- Compare to experiment

In the following chapter the theoretical background of the methods used will be detailed.

2 | Theory

In this chapter, theoretical topics important to the core of this work will be detailed. More specifically, local and global optimization are explained – the latter with a focus on genetic algorithms – and then the methods that have been chosen are being shown. The methods have been chosen in hope to be able to describe the desired molecule-surface systems.

2.1 Local Optimization

Local Optimization is usually being done by determining the gradient for a system and then moving along the direction of said gradient (or rather into the inverse direction of the gradient), leading to the next minimum in that direction. For example, in the case of the steepest descent algorithm, which is probably the simplest algorithm, the search direction is the inverse of the gradient (since the objective is to minimize and the gradient vector points to the nearest maximum). This is given by $d = -g$. This is sure to work (an even guaranteed to work in quadratic potentials), but the consecutive steps will be orthogonal to each other. An improvement to the steepest descent are the conjugate gradient (CG) methods. In CG methods, the step is modified to include the previous step scaled by a factor β_i (Eq. 2.1).

$$d_i = -g_i + \beta_i \cdot d_{i-1} \tag{2.1}$$

Depending on the step width one can overshoot in that direction. Therefore many different formulas for calculating the step size have been presented. One of these is the Fletcher-Reeves formula (Eq. 2.2).

$$\beta_i^{PR} = \frac{d_{i+1}^T d_{i+1}}{d_i^T d_i} \tag{2.2}$$

The algorithm that has mainly been used in this thesis is the L-BFGS algorithm, which is a limited-memory version of BFGS, named after *Broyden*, *Fletcher*, *Goldfarb* and *Shanno*[1] [36–39]. As a quasi-Newton method it avoids calculation of the full Hessian by approximating it iteratively. It is a widely used method due to its error tolerance with regards to step size control. Quasi-Newton methods generally work by using a quadratic expansion around the current position. The step direction is then chosen based on the previous steps – not unsimilar to the CG methods. The step size is chosen such that the area where the quadratic approximation is valid is not exited.

[1] An interesting bit about this algorithm is that the four people it is named after came up with it independently in the same year.

2.2 Global Optimization

The idea of global optimization is to find the best configuration for a given setup within its entire search space. In chemistry - where the property in question is often the lowest total energy - any given problem, consisting of more than a few atoms, contains a lot of degrees of freedom and therefore has a complicated and high-dimensional energy landscape. Since traversing this landscape completely is generally not feasible, several algorithms that utilize stochastic heuristic rules have been applied to these types of problems. Within this work evolutionary algorithms are used. The naming of these algorithms takes inspiration from nature in the way that there is a population of individuals that get assigned a fitness value and are recombined with another individual based on this fitness. Therefore the fittest individuals get to pass on their information more often than less fit ones. The idea of mutation is also taken from nature and realized by making changes to an existing individual. However, it should be noted that this usage of nature inspired terms may actually be hindering the improvement of global optimization algorithms by making them seemingly less comparable. A more neutral phrasing of the ingredients that is at least as descriptive is possible and should be used [14]. It can also be argued that the "survival of the fittest" is actually not a global optimization at all, since the goal it strives for is rather "being good enough to survive" while not expending too much energy in the process[2] instead of actually optimizing a feature fully. Mutation, crossover and individuals can also easily be named by more neutral descriptors of what they are actually supposed to achieve, in order to make it easier to compare different algorithms and even different types of global optimization techniques. The population is basically a set of points in search space, which is usually the potential energy surface (PES) if one wants to find the most stable structure. This set of points can be changed towards better results in a fitness function, where fitness, again, shows this reminiscence of "survival of the fittest", a more neutral name would be objective function. The two types of operations on the points are the crossover and mutation. For crossover two points are taken and their attributes are recombined to form two new potential solutions that have then to be evaluated against the objective function (see Fig. 2.1). Mutation is a specific manipulation of only a small part (e.g. a single atom in an atomic cluster) that is randomly relocated (see Fig. 2.2). Systematically applying these steps in combination with local optimization (locopt) of every newly created individual is typically being done to ensure that only minima are being found. The reason for this is the fact that

[2] From the authors experience global optimization is also often concerned with keeping computational cost down, which may bear a different kind of likeness to evolution.

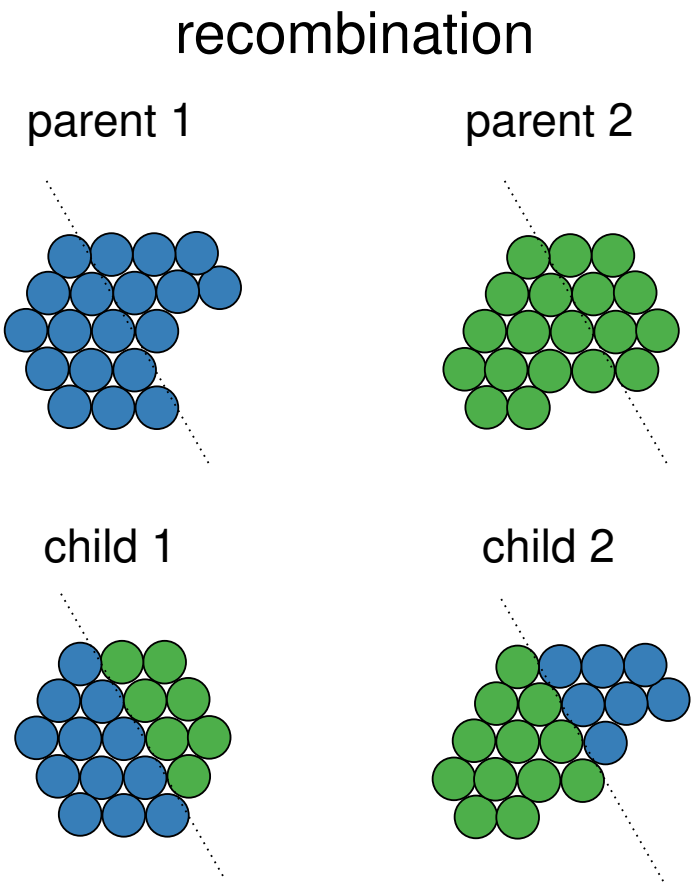

Figure 2.1: An example for the recombination of two individuals in 2D space.

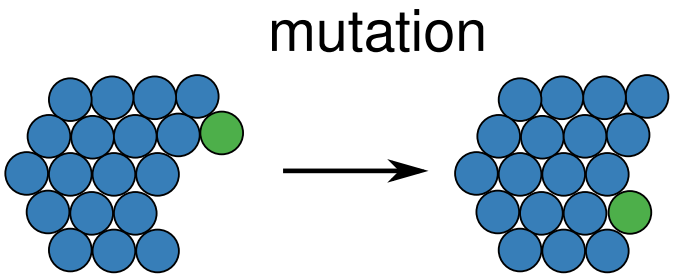

Figure 2.2: An example for the mutation of an individual in 2D space.

global optimization alone is very inefficient at getting to the minimum of a funnel-like potential well quickly, whereas this is exactly what local optimization algorithms are designed for. In the case of cluster optimization recombination can actually be applied in 3D space, by cutting clusters along a plane and recombining parts from different clusters as described above. Obviously the amount of atoms or molecules in the cluster must stay the same, so the cutting planes have to be chosen carefully. Since this approach does not systematically scan the entire potential energy surface, there is no way to be certain about the global optimum, one can however be reasonably confident, when the same optimum structure is being found by multiple optimization runs. Within our workgroup the global optimization program OGOLEM [40] has been developed by *Johannes M. Dieterich* and *Bernd Hartke*, which deploys a pool-based evolutionary algorithm as used in this work. A schematic image describing a pool-based optimization algorithm is shown by Fig. 2.3. The initial population is a set of randomly generated points in search space that are optimized and evaluated according to their objective function value. Out of this pool individuals are chosen based on the objective function value and then recombined. With a certain percentage a mutation may occur on any of the recombined individuals. These are then each locally optimized and if they are sufficiently different from the individuals in the pool – either by energy or other criteria to maintain structural diversity –, then they are added to the pool, otherwise the new solutions will be discarded. After a stop criterion (usually a number of recombination steps) is reached, the optimization finishes. The key advantage of this pool-based algorithm over generational algorithms is that it avoids the bottleneck that occurs near the end of each generation, when most of the CPU cores would be idling until new individuals are created and distributed and thus wasting CPU time.

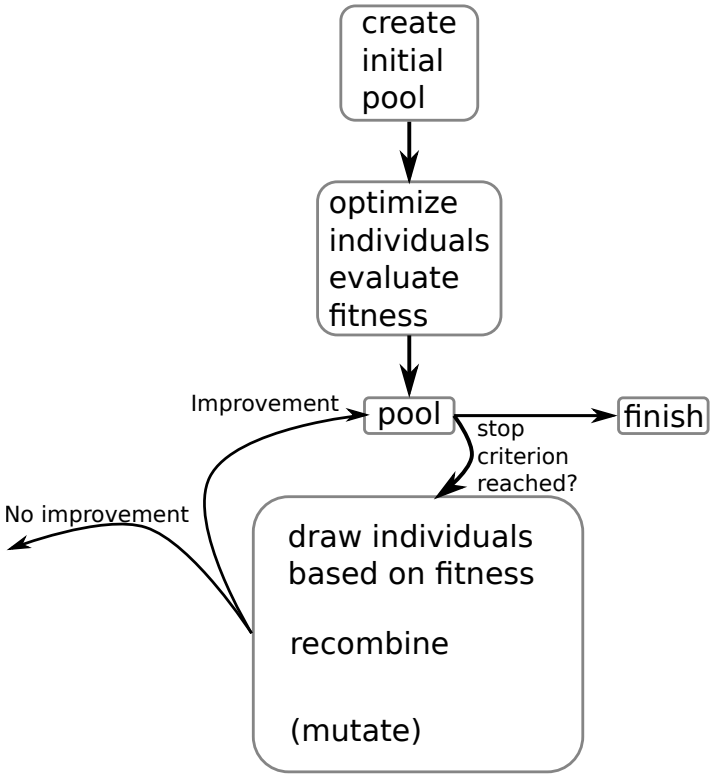

Figure 2.3: Scheme showing the process of a pool based global optimization scheme.

2.3 Force Fields

In general, force fields (FF) describe the interaction of particles (atoms), often by different contributions to a total energy. Their simple nature enables calculations for large numbers of atoms - e.g. the CHARMM force field for proteins [41,42], while their accuracy is only limited by the quality of the parametrization and the functional form of the force field. One such force field is the so-called OPLS-aa force field by *Jorgensen et al.* [43], which will be described here as an example for force fields in general. This force field is described by

$$E = E_{ab} + E_{bond} + E_{angle} + E_{torsion} \tag{2.3}$$

where E_{ab} are the nonbonded interactions described by Coulomb and Lennard-Jones terms:

$$E_{ab} = \sum_{i}^{on\,a} \sum_{j}^{on\,b} \left[\frac{q_i q_j e^2}{r_{ij}} + 4\epsilon_{ij} \left(\frac{\sigma_{ij}^{12}}{r_{ij}^{12}} - \frac{\sigma_{ij}^{6}}{r_{ij}^{6}} \right) \right] f_{ij}. \tag{2.4}$$

These equations are also being applied to intramolecular interactions between atoms that are more than three bonds apart. Here q_i and q_j are charges on atoms i and j, r_{ij} is the distance between i and j and f_{ij} is a scaling factor that is only $\neq 1$

for 1,4-interactions, where $f_{ij} = 0.5$. Mixing rules are being applied and therefore $\sigma_{ij} = \sqrt{\sigma_{ii}\sigma_{jj}}$ and $\epsilon_{ij} = \sqrt{\epsilon_{ii}\epsilon_{jj}}$. It is worth noting that this geometric mean rule differs from the frequently used Lorentz-Berthelot mixing rules [44,45][3], where $\sigma_{ij} = \frac{\sigma_i + \sigma_j}{2}$. The rule presented here is also known as the Good-Hope rule [46]. The bond stretching is described as quadratic terms in Eq. 2.5 with the equilibrium distance r_{eq} and distance r. Similarly the angle bending in Eq. 2.6 is also a quadratic term with angles θ and equilibrium angles θ_{eq} with the force constants K_r and K_θ.

$$E_{bond} = \sum_{bonds} K_r \left(r - r_{eq}\right)^2 \tag{2.5}$$

$$E_{angle} = \sum_{angles} K_\theta \left(\theta - \theta_{eq}\right)^2 \tag{2.6}$$

Lastly the dihedral angle, or torsion, is described by a Fourier expansion in Eq. 2.7. There ϕ_i is the dihedral angle, V_1, V_2 and V_3 are Fourier coefficients, and $f1$, $f2$ and $f3$ are phase angles[4].

$$E_{torsion} = \sum_i \frac{V_1^i}{2}\left[1 + \cos(\phi_i + f_i 1)\right] + \frac{V_2^i}{2}\left[1 - \cos(2\phi_i + f_i 2)\right] + \frac{V_3^i}{2}\left[1 + \cos(3\phi_i + f_i 3)\right] \tag{2.7}$$

Obviously, depending on these equations means that the bond information can not change on-the-fly during an optimization, since a quadratic bond equation could never describe bond breakage. The OPLS-aa torsional angles were parametrized against RHF/6-31G* reference data, while the bond stretching and angle bending terms have been taken from the AMBER AA force field [48, 49]. Additionally, OPLS-aa has been validated against MC simulations of liquids, from which many properties (e.g. intermolecular and intramolecular energies, vaporization enthalpies, volumes and densities) were derived and compared to the FF results. Another force field that has been used is the GFN-FF based on the semiempirical GFN methods. This will be explained later in section 2.6 due to the development being based on the semiempirical methods.

2.4 ReaxFF

The obvious advantage of ReaxFF [50] compared to force fields like OPLS or AMBER is its ability of bond formation and bond breakage. Its inital version has been introduced

[3]Even though this appears the most common citation for the Berthelot rule, in written form it can be found on page 1856 in a letter from *van der Waals* and in a note from Berthelot on page 1858 of the same issue. These seem to reference the cited note, but since the publications appeared in french this was all the author could understand from them.

[4]These phase angles are 0 for all the molecules presented in Ref. 43 and the Lammps implementation apparently also does not include them [47].

by *van Duin et al.* in 2001 and was created specifically for hydrocarbons. For ReaxFF the total energy can be written as a sum of terms for bonds (E_{bond}), overcoordination penalty (E_{over}), undercoordination penalty (E_{under}), valence angles (E_{val}), a penalty term for valence angles (E_{pen}), torsion (E_{tors}), a conjugation term (E_{conj}), and van-der-Waals and Coulomb terms ($E_{vdWaals}$ and $E_{Coulomb}$).

$$E_{system} = E_{bond} + E_{over} + E_{under} + E_{val} + E_{pen} + E_{tors} + E_{conj} + E_{vdWaals} + E_{Coulomb} \quad (2.8)$$

When comparing Eq. 2.8 to Eq. 2.3 one can easily see that the ReaxFF energy contains additional terms related to over- and undercoordination and valence. This change is necessary for changing bond orders, which is required in order to describe reactions. Therefore the main concept of ReaxFF hinges on the bond order BO'_{ij} of an atom pair. In Eq. 2.9 this is written as the sum of three exponential functions, one per bond type, in the case of carbon.[5]

$$BO'_{ij} = \exp\left[p_{bo,1} \cdot \left(\frac{r_{ij}}{r_0}\right)^{p_{bo,2}}\right] + \exp\left[p_{bo,3} \cdot \left(\frac{r_{ij}}{r_{0,\pi}}\right)^{p_{bo,4}}\right] + \exp\left[p_{bo,5} \cdot \left(\frac{r_{ij}}{r_{0,\pi\pi}}\right)^{p_{bo,6}}\right] \quad (2.9)$$

This allows for any and all bonds of a carbon atom to be a single, double or triple bond. This generally can lead to an overestimation of the bond order that needs to be corrected. This is being done by multiplication with correction factors described by Eq. 2.10-2.15[6]

$$BO_{ij} = BO'_{ij} \cdot f_1(\Delta'_i, \Delta'_j) \cdot f_4(\Delta'_i, BO'_{ij}) \cdot f_5(\Delta'_j, BO'_{ij}) \quad (2.10)$$

$$f_1(\Delta'_i, \Delta'_j) = \frac{1}{2} \cdot \left(\frac{Val_i + f_2(\Delta'_i, \Delta'_j)}{Val_i + f_2(\Delta'_i, \Delta'_j) + f_3(\Delta'_i, \Delta'_j)} + \frac{Val_j + f_2(\Delta'_i, \Delta'_j)}{Val_j + f_2(\Delta'_i, \Delta'_j) + f_3(\Delta'_i, \Delta'_j)}\right) \quad (2.11)$$

$$f_2(\Delta'_i, \Delta'_j) = \exp\left(-\lambda_1 \cdot \Delta'_i\right) + \exp\left(-\lambda_1 \cdot \Delta'_j\right) \quad (2.12)$$

$$f_3(\Delta'_i, \Delta'_j) = \frac{1}{\lambda_2} \cdot \ln\left\{\frac{1}{2} \cdot \left[\exp\left(-\lambda_2 \cdot \Delta'_i\right) + \exp\left(-\lambda_2 \cdot \Delta'_j\right)\right]\right\} \quad (2.13)$$

$$f_4(\Delta'_i, BO'_{ij}) = \frac{1}{1 + \exp\left(-\lambda_3 \cdot \left(\lambda_4 \cdot BO'_{ij} \cdot BO'_{ij} - \Delta'_i\right) + \lambda_5\right)} \quad (2.14)$$

$$f_5(\Delta'_j, BO'_{ij}) = \frac{1}{1 + \exp\left(-\lambda_3 \cdot \left(\lambda_4 \cdot BO'_{ij} \cdot BO'_{ij} - \Delta'_j\right) + \lambda_5\right)} \quad (2.15)$$

[5] This equation has been altered slightly from the cited publication, in order to correct the π and $\pi\pi$ subscripts in accordance with the given parameters within the same publication [50].

[6] Another correction was made to Eq. 2.15, which included Δ'_i even though f_5 is a function of Δ'_j.

Val_i is the valency of an atom i, depending on the kind of atom, Δ'_i is the difference between the calculated bond order and the valency of any given atom, which can be written as Eq. 2.16. The λ_n variables are general parameters.

$$\Delta'_i = \sum_{j=1}^{nbond} BO'_{ij} - Val_i. \tag{2.16}$$

With all these corrections to the bond order, the bond energy can be expressed as Eq. 2.17.

$$E_{bond} = -D_e \cdot BO_{ij} \cdot \exp\left[p_{be,1}\left(1 - BO_{ij}^{p_{be,1}}\right)\right] \tag{2.17}$$

Since there may still be residual overcoordination, the energy penalty term E_{over} was introduced with Eq. 2.18.

$$E_{over} = p_{over} \cdot \Delta_i \cdot \left(\frac{1}{1 + \exp\left(\lambda_6 \cdot \Delta_i\right)}\right) \tag{2.18}$$

Since an atom could also be undercoordinated - a simple example would be something like a carbene CH_2, there is also the undercoordination energy term in Eq. 2.19 with the bond order correction function f_6 in Eq. 2.20.

$$E_{under} = -p_{under} \cdot \frac{1 - \exp\left(\lambda_7 \cdot \Delta_i\right)}{1 + \exp\left(-\lambda_8 \cdot \Delta_i\right)} \cdot f_6\left(BO_{ij,\pi}, \Delta_j\right) \tag{2.19}$$

$$f_6\left(BO_{ij,\pi}, \Delta_j\right) = \frac{1}{1 + \lambda_9 \cdot \exp\left(\lambda_{10} \cdot \sum_{j=1}^{neighbors(i)} \Delta_j \cdot BO_{ij,\pi}\right)} \tag{2.20}$$

The angle terms have to behave similarly to the bond terms in that they both have to vanish as the bonds dissociate and the bond order goes to zero. Also similar is the fact that the equilibrium angle Θ_0 is depending on the sum of π-bond orders (SBO) as written in Eqs. 2.21-2.31.

$$E_{val} = f_7(BO_{ij}) \cdot f_7(BO_{jk}) \cdot f_8(\Delta_j) \cdot \left\{k_a - k_a \exp\left[-k_b\left(\Theta_0 - \Theta_{ijk}\right)^2\right]\right\} \tag{2.21}$$

$$f_7(BO_{ij}) = 1 - \exp\left(-\lambda_{11} \cdot BO_{ij}^{\lambda_{12}}\right) \tag{2.22}$$

$$f_8(\Delta_j) = \frac{2 + \exp\left(-\lambda_{13} \cdot \Delta_j\right)}{1 + \exp\left(-\lambda_{13} \cdot \Delta_j\right) + \exp\left(p_{v,1} \cdot \Delta_j\right)} \cdot \left[\lambda_{14} - \left(\lambda_{14} - 1\right) \cdot \frac{2 + \exp(\lambda_{15} \cdot \Delta_j)}{1 + \exp\left(\lambda_{15} \cdot \Delta_j\right) + \exp\left(-p_{v,2} \cdot \Delta_j\right)}\right] \tag{2.23}$$

$$SBO = \Delta_j - 2 \cdot \left\{1 - \exp\left[-5 \cdot \left(\frac{1}{2}\Delta_j\right)^{\lambda_{16}}\right]\right\} + \sum_{n=1}^{neighbors(j)} BO_{jn,\pi} \tag{2.24}$$

$$\Delta_{j,2} = \Delta_j \quad \text{if} \quad \Delta_j < 0 \tag{2.25}$$

$$\Delta_{j,2} = 0 \quad \text{if} \quad \Delta_j \geq 0 \tag{2.26}$$

$$SBO2 = 0 \quad \text{if} \quad SBO \leq 0 \tag{2.27}$$

$$SBO2 = SBO^{\lambda_{17}} \quad \text{if} \quad 0 < SBO < 1 \tag{2.28}$$

$$SBO2 = 2 - (2 - SBO)^{\lambda_{17}} \quad \text{if} \quad 1 < SBO < 2 \tag{2.29}$$

$$SBO2 = 2 \quad \text{if} \quad SBO > 2 \tag{2.30}$$

$$\Theta_0 = \pi - \Theta_{0,0} \cdot \{1 - \exp\left[-\lambda_{18} \cdot (2 - SBO2)\right]\} \tag{2.31}$$

The E_{pen} energy term is used to reproduce the stability of linear systems like the carbon atoms in an allene molecule (Eqs. 2.32 and 2.33).

$$E_{pen} = \lambda_{19} \cdot f_9(\Delta_j) \cdot \exp\left[-\lambda_{20} \cdot (BO_{ij} - 2)^2\right] \cdot \exp\left[-\lambda_{20} \cdot (BO_{jk} - 2)^2\right] \tag{2.32}$$

$$f_9(\Delta_j) = \frac{2 + \exp\left(-\lambda_{21} \cdot \Delta_j\right)}{1 + \exp\left(-\lambda_{21} \cdot \Delta_j\right) + \exp\left(\lambda_{22} \cdot \Delta_j\right)} \tag{2.33}$$

The torsion angles have to be treated properly with respect to the bond order as well (Eqs. 2.34-2.36).

$$\begin{aligned} E_{tors} = & f_{10}(BO_{ij}, BO_{jk}, BO_{kl}) \cdot \sin\left(\Theta_{ijk}\right) \cdot \sin\left(\Theta_{jkl}\right) \\ & \cdot \left[\frac{1}{2} V_2 \cdot \exp\left\{p_l \left(BO_{jk} - 3 + f_{11}\left(\Delta_j, \Delta_k\right)\right)^2\right\}\right. \\ & \left. \cdot \left(1 - \cos\left(2\omega_{ijkl}\right)\right) \cdot \frac{1}{2} V_3 \cdot \left(1 + \cos\left(3\omega_{ijkl}\right)\right)\right] \end{aligned} \tag{2.34}$$

$$\begin{aligned} f_{10}\left(BO_{ij}, BO_{jk}, BO_{kl}\right) = & \left[1 - \exp\left(-\lambda_{23} \cdot BO_{ij}\right)\right] \cdot \left[1 - \exp\left(-\lambda_{23} \cdot BO_{jk}\right)\right] \\ & \cdot \left[1 - \exp\left(-\lambda_{23} \cdot BO_{kl}\right)\right] \end{aligned} \tag{2.35}$$

$$f_{11}\left(\Delta_j, \Delta_k\right) = \frac{2 + \exp\left[-\lambda_{24} \cdot \left(\Delta_j + \Delta_k\right)\right]}{1 + \exp\left[-\lambda_{24} \cdot \left(\Delta_j + \Delta_k\right)\right] + \exp\left[\lambda_{25} \cdot \left(\Delta_j + \Delta_k\right)\right]} \tag{2.36}$$

Furthermore, the energy contribution of conjugated electrons is described in Eqs. 2.37 and 2.38[7].

$$E_{conj} = f_{12}\left(BO_{ij}, BO_{jk}, BO_{kl}\right) \cdot \lambda_{26} \cdot \left[1 + \left(\cos^2\left(\omega_{ijkl}\right) - 1\right) \cdot \sin\left(\Theta_{ijk}\right) \cdot \sin\left(\Theta_{jkl}\right)\right] \tag{2.37}$$

$$\begin{aligned} f_{12}\left(BO_{ij}, BO_{jk}, BO_{kl}\right) = & \exp\left[-\lambda_{27} \cdot \left(BO_{ij} - \frac{3}{2}\right)^2\right] \cdot \exp\left[-\lambda_{27} \cdot \left(BO_{jk} - \frac{3}{2}\right)^2\right] \cdot \\ & \exp\left[-\lambda_{27} \cdot \left(BO_{kl} - \frac{3}{2}\right)^2\right] \end{aligned} \tag{2.38}$$

[7]The author has taken the liberty of changing the mixed fractions to proper fractions.

Finally there are the van der Waals and Coulomb interactions that are being described by a Morse-potential (Eqs. 2.39 and 2.40) and the interaction of point charges (Eq. 2.41), respectively.

$$E_{vdWaals} = D_{ij} \cdot \left\{ \exp\left[\alpha_{ij} \cdot \left(1 - \frac{f_{13}\left(r_{ij}\right)}{r_{vdW}}\right)\right] - 2 \cdot \exp\left[\frac{1}{2} \cdot \alpha_{ij} \cdot \left(1 - \frac{f_{13}\left(r_{ij}\right)}{r_{vdW}}\right)\right]\right\} \tag{2.39}$$

$$f_{13}\left(r_{ij}\right) = \left[r_{ij}^{\lambda_{29}} + \left(\frac{1}{\lambda_w}\right)^{\lambda_{28}}\right]^{\frac{1}{\lambda_{28}}} \tag{2.40}$$

$$E_{Coulomb} = C \cdot \frac{q_i \cdot q_j}{\left[r_{ij}^3 + \left(\frac{1}{\gamma_{ij}}\right)^3\right]^{\frac{1}{3}}} \tag{2.41}$$

A more recent version of the force field description has been made by *Chenoweth et al.* [51], but most of the equations have remained the same and the changes are not of relevance here. The changes mainly concern differences in how the bond orders are calculated. All in all this means that ReaxFF requires 28 general parameters and 26 atom-specific parameters, which is a multiple of the parameters in, e.g., OPLS-aa. The vast amount of parameters in ReaxFF makes creating a parameter set for any given problem a global optimization problem itself [52, 53]. With regards to using ReaxFF in global optimization this means that one must proceed with caution, since the global optimization algorithms may produce structures that are far away from any optimal structures and even though the PES should be well behaved in regions where reference data was used for fitting, outside of these areas the quality of the description is unknown. Here the number of parameters means, that overfitting of the parameters may produce great results around the reference while producing erratic results elsewhere. Even more recently there has been an approach by *Furman et al.* to smoothen some of the described functions in order to allow for better ReaxFF molecular dynamics [54, 55]. This approach uses additional Hermite tapering polynomials to achieve the behavior improvement.

The parametrization in the case of the parameters used in this thesis has been intended for combustion reactions on PtNi-alloy surfaces [56]. Towards this goal the platinum and nickel parameters have first been adjusted to accurately describe the formation energy of the alloy within 80%-120% of the optimal volume. Furthermore, the adsorption energies of various species relevant to combustion have been used for parametrization as well. These species are C, H, O, CO, CH, CH_2, CH_3, OH and H_2O, which are all much smaller than anything the parameters will be applied to in the results section of this thesis, however the previously developed parameters for organic molecules were

used as a starting point for this parametrization. Long-range interactions, valence angles and bonded interactions were specifically considered during the parametrization of this parameter set.

2.5 Semiempirical Approaches

In the field of semiempirical methods there are many quantum mechanical (SEQM) methods that are widely applied. These methods are classified by their degree of neglect of the differential overlap between atomic orbitals, which is the main reason for their computational savings. Some semiempirical methods have been derived from density functional theory, namely DFTB (see next section) in 1995 [57]. This method later inspired the GFN-xTB set of methods [58, 59], which in turn resulted in a new force field, GFN-FF, introduced in late 2019 [60]. In the following subsections, DFTB and GFN-xTB will be described.

2.5.1 DFTB

The acronym DFTB stands for **D**ensity **F**unctional-based **T**ight **B**inding. Based on different, older tight-binding schemes [61] it has been introduced by *Porezag et al.* in 1995 [57]. In this method, Kohn-Sham DFT orbitals ψ_i are expressed by atom-centered localized basis functions ϕ_μ (Eq. 2.42).

$$\psi_i\left(\mathrm{r}\right) = \sum_\nu C_{\nu i}\phi_\nu\left(\mathrm{r} - R_k\right) \tag{2.42}$$

The Kohn-Sham DFT equations in an effective one-particle potential $V_{eff}\left(r\right)$ can be written as Eq. 2.43.

$$\hat{H}\psi_i\left(\mathrm{r}\right) = \epsilon_i\psi_i\left(\mathrm{r}\right), \quad \hat{H} = \hat{T} + V_{eff}\left(\mathrm{r}\right) \tag{2.43}$$

This gives a sum of algebraic terms (Eq. 2.44), or the Hartree-Fock equations.

$$\sum_\nu C_{\nu i}\left(H_{\mu\nu} - \epsilon_i S_{\mu\nu}\right) = 0, \quad \forall\mu, i \tag{2.44}$$

This contains the Hamiltonian matrix $H_{\mu\nu}$ and the overlap matrix $S_{\mu\nu}$, which are calculated by Eq. 2.45.

$$H_{\mu\nu} = \left\langle\phi_\mu|\hat{H}|\phi_\nu\right\rangle, \quad S_{\mu\nu} = \langle\phi_\mu|\phi_\nu\rangle \tag{2.45}$$

The total energy E_{tot} is approximated as a sum over the band-structure energy E_{BS} and a repulsive potential E_{rep} (Eq. 2.46).

$$E_{tot}\left(\{R_k\}\right) = E_{BS}\left(\{R_k\}\right) + E_{rep}\left(\{|R_k - R_l|\}\right) = \sum_i n_i \epsilon_i\left(\{R_k\}\right) + \sum_k \sum_{<l} V_{rep}\left(|R_l - R_k|\right) \tag{2.46}$$

Here n_i is the occupation number of an orbital i. The band structure energy is the sum of eigenvalues of all occupied orbitals. The pseudoatomic wave functions are defined as Slater-type orbitals and spherical harmonics (Eq. 2.47).

$$\phi_\nu\left(\mathrm{r}\right) = \sum_{n,\alpha,l_\nu,m_\nu} a_{n\alpha} r^{l_\nu+n} e^{-\alpha r} Y_{l_\nu m_\nu} \frac{\mathrm{r}}{r} \tag{2.47}$$

The basis consists of five values for α and the range of n is 0 to 3. These functions are then used to self-consistently solve modified Kohn-Sham equations (Eqs. 2.48 and 2.49).

$$\left[\hat{T} + V^{psat}\left(r\right)\right] \phi_\nu\left(\mathrm{r}\right) = \epsilon_\nu^{psat} \phi_\nu\left(\mathrm{r}\right) \tag{2.48}$$

$$V^{psat}\left(r\right) = V_{nucleus}\left(r\right) + V_{Hartree}\left[n\left(r\right)\right] + V_{XC}^{LDA}\left[n\left(r\right)\right] + \left(\frac{r}{r_0}\right)^N \tag{2.49}$$

The solutions ϕ_ν can be used in an LCAO approach. The effective one-electron potential V_{eff} can be written as a sum of spherical atomic terms (Eq. 2.50).

$$V_{eff}\left(\mathrm{r}\right) = \sum_k V_0^k\left(|\mathrm{r} - R_k|\right) \tag{2.50}$$

Here V_0 is the Kohn-Sham potential of a neutral pseudoatom that is being compressed by its surrounding. This approach has shown to be advantageous for integration and specifically for describing condensed matter applications [57]. The Hamiltonian matrix can be simplified by quite a few entries (Eq. 2.51).

$$H_{\mu\nu} = \begin{cases} \epsilon_\mu^{\text{free atom}} & \text{if} \quad \mu = \nu \\ \left\langle \phi_\mu^A \left| \hat{T} + V_0^A + V_0^B \right| \phi_\nu^B \right\rangle & \text{if} \quad A \neq B \\ 0 \quad \text{otherwise} \end{cases} \tag{2.51}$$

With the Hamiltonian completely defined, only the repulsive potential V_{rep} is left. V_{rep} can be written as the difference between the total energy from the self consistent calculation and the band stucture energy E_{BS}, by rearranging Eq. 2.46 resulting in Eq. 2.52.

$$V_{rep}\left(R\right) = E_{LDA}^{sc}\left(R\right) - E_{BS}\left(R\right) \tag{2.52}$$

The repulsive potential can then be rewritten as a sum of polynomials (Eq. 2.53).

$$V_{rep}(R) = \begin{cases} \sum_n^{NP} d_n (R_c - R)^n & \text{if } (R < R_c) \\ 0 \quad \text{otherwise} \end{cases} \tag{2.53}$$

In this equation R_c is a cutoff distance at which the repulsive potential smoothly vanishes to zero, NP is the highest exponent of the sum of polynomials and has empirically been found to be sufficient when $NP = 5$. More recent advances and rewrites of this tight-binding approach have been made [62, 63].

2.5.2 GFN-xTB methods

The GFN-xTB methods by *Grimme et al.* [58, 59] have been motivated by the performance of the previously introduced sTDA-xTB [64]. GFN stands for the intention to deliver accurate **G**eometries, **F**requencies and **N**oncovalent interactions. The extensions (x in xTB) stand for extensions to the atomic orbital (AO) basis set and the form of the Hamiltonian. The total energy consists of the electronic energy E_{el}, atomic repulsion E_{rep}, dispersion E_{disp} and halogen-bonding E_{XB} (Eq. 2.54).

$$E = E_{el} + E_{rep} + E_{disp} + E_{XB} \tag{2.54}$$

The electronic energy is given by equation 2.55.

$$E_{el} = \sum_i^{occ.} n_i \langle \psi_i | H_0 | \psi_i \rangle + \frac{1}{2} \sum_{A,B} \sum_{l(A)} \sum_{l'(B)} p_l^A p_{l'}^B \gamma_{AB,ll'} + \frac{1}{3} \sum_A \Gamma_A q_A^3 - T_{el} S_{el} \tag{2.55}$$

Here ψ_i are the valence molecular orbitals, n_i are the occupation numbers and H_0 is the zeroth-order Hamiltonian. The sum terms are the self-consistent charge (SCC) contributions, where q_A is the Mulliken charge of atom A, Γ_A is the charge derivative of the Hubbard parameter η_A. The triple sum is over all shells l and l' on atoms A and B where p_l^A is the charge distributed over the orbital shells with angular momentum l located at atom A (Eq. 2.56).

$$p_l^A = p_l^{A_0} - \sum_\nu^{N_{AO}} \sum_{\mu \in A, \mu \in l} S_{\mu\nu} P_{\mu\nu} \tag{2.56}$$

N_{AO} is the total number of atomic orbitals, $p_l^{A_0}$ is the reference occupation for the free atom. $S_{\mu\nu}$ is the overlap matrix, while $P_{\mu\nu}$ is the population matrix. These shell

atomic charges can be summed up to the atomic partial charges (Eq. 2.57).

$$q_A = \sum_{l \in A} p_l^A \tag{2.57}$$

The distance dependence of the Coulomb interactions in Eq. 2.55 is given by Eq. 2.58.

$$\gamma_{AB,ll'} = \left(\frac{1}{R_{AB}^{k_g}} + \eta^{-k_g} \right)^{-\frac{1}{k_g}} \tag{2.58}$$

R_{AB} is the interatomic distance, k_g is a global parameter and η is the average chemical hardness of the atoms A and B, not to be confused with η_A in Eq. 2.55. η is defined by Eq. 2.59.

$$\eta = 2 \left(\frac{1}{\left(1 + \kappa_A^l\right) \eta_A} + \frac{1}{\left(1 + \kappa_B^{l'}\right) \eta_B} \right)^{-1} \tag{2.59}$$

Here η_A and η_B are element-specific parameters, and κ_A^l and $\kappa_B^{l'}$ are also element-specific scaling factors. The orbital occupations in Eq. 2.55 do not have to be natural numbers, fractional occupations are allowed. Due to these the electronic temperature T_{el} multiplied with the electronic entropy S_{el} term was added. The electronic temperature is used as an adjustable parameter. The orbital occupations for the spin molecular orbital ψ_i are given by Eq. 2.60.

$$n_i \left(T_{el}\right) = \frac{1}{\exp\left[\left(\epsilon_i - \epsilon_F\right) / \left(k_B T_{el}\right)\right] + 1} \tag{2.60}$$

Here ϵ_i is the orbital energy of ψ_i, while ϵ_F is the Fermi-level. The orbitals ψ_i are expressed as a linear combination of atomic orbitals (LCAO) as in equation 2.61.

$$\psi_i = \sum_{\mu}^{N_{AO}} c_{\mu i} \phi_\mu \left(\zeta, \text{STO-mG}\right) \tag{2.61}$$

Changing the coefficients $c_{\mu i}$ such that the electronic energy becomes minimal leads to the eigenvalue problem that can be written as Eq. 2.62.

$$FC = SC\epsilon \tag{2.62}$$

With the Fock matrix F, the overlap matrix S, and the MO coefficients C and eigenvalues ϵ. The AOs ϕ are Slater-Type-Orbitals (STO) comprised of Gaussian functions. The exponents ζ are element-specific parameters. The matrix elements of the Hamil-

tonian are calculated by an SCC-method similar to DFTB3 (Eq. 2.63).

$$\begin{aligned}\langle \phi_\mu | F | \phi_\nu \rangle = \langle \phi_\mu | H_0 | \phi_\nu \rangle + \frac{1}{2} S_{\mu\nu} \sum_C \sum_{l''} \left(\gamma_{AC,ll''} + \gamma_{BC,l'l''}\right) p^C_{l''} \\ + \frac{1}{2} S_{\mu\nu} \left(q_A^2 \Gamma_A + q_B^2 \Gamma_B\right) \quad (\mu \in l(A), \nu \in l'(B))\end{aligned} \tag{2.63}$$

The indices μ and ν describe AOs on atoms A and B with corresponding angular momenta l and l' as before. Additionally the second term sums over all atoms C and their shells l''. The H_0 one electron elements are given by equation 2.64.

$$\begin{aligned}\langle \phi_\mu | H_0 | \phi_\nu \rangle = K_{AB} \frac{1}{2} \left(k_l + k_{l'}\right) \frac{1}{2} \left(h_A^l + h_B^{l'}\right) S_{\mu\nu} \left(1 + k_{EN} \Delta EN_{AB}^2\right) \\ \Pi\left(R_{AB,ll'}\right) \quad (\mu \in l(A), \nu \in l'(B))\end{aligned} \tag{2.64}$$

Here k_l and $k_{l'}$ are the Hückel constants as free parameters per angular momentum and h_A^l and $h_b^{l'}$ are effective atomic energy levels. ΔEN_{AB} is the difference between the electronegativity of atoms A and B, such that $\Delta EN_{AB} = EN_A - EN_B$. k_{EN} is a proportionality factor, K_{AB} is a scaling constant, that is usually 1 and only differs from that for specific element pairs. The function $\Pi\left(R_{AB,ll'}\right)$ is depending on the distance R_{AB} and angular momenta l and l' (Eq. 2.65).

$$\Pi\left(R_{AB,ll'}\right) = \left(1 + k_{A,l}^{poly} \left(\frac{R_{AB}}{R_{cov,AB}}\right)^{\frac{1}{2}}\right) \left(1 + k_{B,l'}^{poly} \left(\frac{R_{AB}}{R_{cov,AB}}\right)^{\frac{1}{2}}\right) \tag{2.65}$$

Here $R_{cov,AB}$ is the covalent distance, which is the sum of covalent atomic radii. $k_{A,l}^{poly}$ and $k_{B,l'}^{poly}$ are element-specific parameters. The effective atomic energy levels, h_A^l, are dependent on the D3[8] coordination number (CN) of atom A (Eq. 2.66).

$$h_A^l = H_A^l \left(1 + k_{CN,l} CN_A\right) \quad (l \in A) \tag{2.66}$$

Here $k_{CN,l}$ are global scaling parameters for the different (s, p, d) shells. The parts of the zero-order Hamiltonian that depend on the electronegativity, $\Pi\left(R_{AB,ll'}\right)$ and the coordination numbers CN_A and CN_B should give this TB scheme more flexibility in the covalent interactions. The fact that h_A^l is depending on the coordination number enables different hybridization of e.g. s- and p-orbitals in atoms depending on their surrounding. The repulsion energy is described by a pairwise potential (Eq. 2.67).

$$E_{rep} = \sum_{AB} \frac{Z_A^{eff} Z_B^{eff}}{R_{AB}} e^{-(\alpha_A \alpha_B)^{1/2} (R_{AB})^{k_f}} \tag{2.67}$$

[8]This means the D3 vdW-correction by *Grimme et al.* [65].

Here Z^{eff} are effective nuclear charges fitted to reference data, k_f is another global parameter, and α_A and α_B are element-specific parameters. The dispersion energy is calculated by the D3 method [65]. To alleviate some of the error within the DFTB scheme, a halogen bonding term is introduced (Eq. 2.68).

$$E_{XB} = \sum_{XB} f_{dmp}^{AXB} k_X \left(1 + \left(\frac{R_{cov,AX}}{R_{AX}}\right)^{12} - k_{X2}\left(\frac{R_{cov,AX}}{R_{AX}}\right)^{6}\right) / \left(\frac{R_{cov,AX}}{R_{AX}}\right)^{12} \tag{2.68}$$

$R_{cov,AX} = k_{XR}\left(r_{cov,A+r_{cov,B}}\right)$ is the covalent distance between A and B, k_X, k_{XR} and k_{X2} are global parameters. The damping function carries an angle dependency (Eq. 2.69).

$$f_{dmp}^{AXB} = \left(\frac{1}{2} - \frac{1}{4}\cos\left(\theta_{AXB}\right)\right)^6 \tag{2.69}$$

This ensures that the correction is only acting on linear systems. An explanation for the various errors is given in Ref. 66. In addition to this additional halogen term, the extended basis in GFN-xTB should also alleviate some of the error. The parametrization for GFN-xTB took place by RMSD (root mean square deviation) minimization with respect to reference data. Most of the reference data has been calculated at the hybrid DFT level using the PBE functional. The types of data points used were geometries in equilibrium, ΔE for distorted geometries, harmonic frequencies, atomic charges and noncovalent interaction energies. The reference structures involved in parametrization were mostly molecular structures, including some heavy metal complexes. The system size was up to about one hundred atoms. Validation took place on much larger systems, such as peptides and proteins. However, surface adsorbed structures or molecules have not played a role in the parametrization of this method.

2.6 GFN-FF

After the development of the semiempirical GFN methods, which by now comprise GFN0, GFN1 and GFN2, an additional force-field method called GFN-FF [60] has been developed by *Spicher et al.* which shall be described here as well, as it has been used extensively in this thesis due to the fact that is was the first method in this work to reliably deliver molecules reasonably adsorbed on surfaces. The total energy in GFN-FF can be written as the sum of covalent (E_{cov}) and non-covalent interactions (E_{NCI}) (Eq. 2.70).

$$E_{GFN-FF} = E_{cov} + E_{NCI} \tag{2.70}$$

The covalent interactions are mostly the same as in other force fields (Eq. 2.71).

$$E_{cov} = E_{bond} + E_{bend} + E_{tors} + E_{rep}^{bond} + E_{abs}^{bond} \tag{2.71}$$

The non-covalent interactions can be expressed by Eq. 2.72.

$$E_{NCI} = E_{IES} + E_{disp} + E_{HB} + E_{XB} + E_{rep}^{NCI} \tag{2.72}$$

Here E_{IES} is the isotropic electrostatic energy, E_{disp} is the dispersion energy, E_{HB} and E_{XB} are terms for hydrogen and halogen bonds and E_{rep}^{NCI} is the Pauli repulsion term. The bond energy term is given by a Gaussian type function, which does allow for bond dissociation in GFN-FF (Eq. 2.73).

$$E_{bond} = \sum_{bonds} -k_{str} \cdot \exp\left[-\eta_{bond}\left(1 + k_{EN}\left|\Delta EN\left(AB\right)\right|^2\right) \cdot \left(R_{AB} - R_{AB}^0\right)^2\right] \tag{2.73}$$

The way this is implemented means that bonds can dissociate and reform, but new bonds can not be established, making this a dissociative force field. R_{AB} is the interatomic distance, while R_{AB}^0 is a precomputed equilibrium value calculated by Eq. 2.75. η_{bond} and k_{EN} are global parameters. $\Delta EN = (EN_A - EN_B)$ is the difference in electronegativity between A and B, while k_{str} is the force constant of the bond (Eq. 2.74), which is a function of the coordination number (f_{CN}), the atomic charges (f_{qq}), the π-bond character (f_π), element type (f_{hvy}), and if the atoms are in a ring system (f_{rng}), k_b are element specific parameters, which are fit to reference data.

$$k_{str}\left(AB\right) = f_{CN} \cdot f_{qq} \cdot f_\pi \cdot f_{hvy} \cdot f_{rng} \cdot k_b\left(A\right) \cdot k_b\left(B\right) \tag{2.74}$$

$$R_{AB}^0 = \left(R_A^0 + R_B^0 + R_{sft}\right)\left(1 - c_1\left|\Delta EN\right| - c_2\left|\Delta EN\right|^2\right) \tag{2.75}$$

In Eq. 2.75 c_1 and c_2 are additional fitting parameters. The reference radii R_A^0 and R_B^0 are adapted from the D3 DFT correction. R_{sft} is an element specific shift to the interatomic distance. In the case of oxygen or nitrogen atoms that partake in hydrogen bonds, the exponent in Eq. 2.73 is additionally multiplied by $f_{CN_H} = (1 - 0.1CN_H)$, where CN_H is a modified coordination number from the D3 correction. The angle bending energy is given by Eq. 2.76.

$$E_{bend} = \sum_{bend} f_{dmp} k_{bnd} \begin{cases} \left(\theta^{abc} - \theta_0^{abc}\right)^2 & \theta_0 \approx \pi \\ \left(\cos\left(\theta^{abs}\right) - \cos\left(\theta_0^{abc}\right)\right)^2 & \text{else} \end{cases} \tag{2.76}$$

The case distinction allows for specific treatment of nearly linear angles and other cases. The bending force constant k_{bnd} is a function of the atomic charges f_{qq}, including small angle corrections f_{sml} and corrections for angles with metal as the central atom f_{mtl} (Eq. 2.77).

$$k_{bnd}\left(ABC\right) = f_{qq} \cdot f_{sml} \cdot f_{mtl} \cdot k_a\left(A\right) k_a\left(B\right) k_a\left(C\right) \tag{2.77}$$

k_a are element specific angle bending force constant parameters,
$f_{dmp} = f_{dmp}(AB)\, f_{dmp}(AC)$ consists of the damping functions for AB and AC respectively that are given by Eq. 2.78.

$$f_{dmp}(AB, R) = \frac{1}{1 + k_{dmp}\left(\frac{R_{AB}}{R_{AB}^{cov}}\right)^4} \tag{2.78}$$

Here the covalent distance is calculated as the sum of covalent radii $R_{AB}^{cov} = R_A^{cov} + R_B^{cov}$, k_{dmp} is a global parameter. The damping ensures that the bending energy term vanishes at large distances, which is necessary for the dissociation of a molecule, this is also applied to the torsional energy. The torsional energy is given by Eq. 2.79.

$$E_{tors} = \sum_{torsion} f_{dmp} k_{tor} \left[1 + \cos\left(n\left(\psi - \psi_0\right) + \pi\right)\right] \tag{2.79}$$

The damping factor in this case is the product of three damping functions, one for each bond. ψ_0 is the equilibrium torsion angle, while n ensures the correct periodicity for the torsional rotation, while k_{tor} is the torsional force constant that determines the barrier height for the rotational barrier. It depends on the bond character between the atoms A and B (Eq. 2.80).

$$k_{tor} = f_\sigma \cdot f_\pi \cdot f_{qq} \cdot k_t(AB) \cdot k_t(CD) \tag{2.80}$$

Here k_t are element specific torsion parameters. Since the bond term has been described by a gaussian type function, as opposed to harmonic potentials or Lennard-Jones type potentials, an additional repulsion term is being introduced by Eq. 2.81.

$$E_{rep}^{bond} = \sum_{A,B} \eta_{rep}^{bond} \frac{Z_A^{eff} Z_B^{eff}}{R_{AB}} \exp\left(-\sqrt{\alpha_A \alpha_B R_{AB}^3}\right) \tag{2.81}$$

Z_A^{eff} and Z_B^{eff} are effective nuclear valence charges and are also element specific parameters, like α_A and α_B. The parameter η_{rep}^{bond} is a global scaling parameter for the repulsion energy. GFN-FF also contains a treatment of three-body effects, which is the *Axilrod-Teller-Muto* (ATM) term [67, 68]. In this implementation it requires the participating atoms to be covalently bonded, so *A*-*B* and *B*-*C* must be connected. The ATM term is shown in Eq. 2.82.

$$E_{abc}^{bond} = \sum_{ABC} C_{abc} \frac{\left(3\cos(\theta_a)\cos(\theta_b)\cos(\theta_c) + 1\right)}{\left(R_{AB} R_{AC} R_{BC}\right)^3} \tag{2.82}$$

There $\theta_{a,b,c}$ are the internal angles of the triangle formed by the atoms A, B and C, while R_{AB}, R_{AC} and R_{BC} are the side lengths of the triangle. C_{abc} is a constant depending on the atomic charges f_q of the atoms and their scaled nuclear charges Z (Eq. 2.83).

$$C_{abc} = f_{q,a} \cdot f_{q,b} \cdot f_{q,c} \cdot \eta_{abc} \left(Z_A \cdot Z_B \cdot Z_C\right)^{\frac{1}{3}} \tag{2.83}$$

This three-body term is meant to be a correction to the covalent bonding term, which is described by many-center nuclear-electron attraction and electron-electron repulsion integrals in QM methods. The isotropic electrostatic energy contribution E_{IES} is described by Eq. 2.84.

$$E_{IES} = \sum_A \left[\chi_A q_A + \frac{1}{2} \left(J_{AA} + \frac{2\gamma_{AA}}{\sqrt{\pi}} \right) q_A^2 + \sum_{A>B} q_A q_B \frac{\operatorname{erf}\left(\gamma_{AB} R_{AB}\right)}{R_{AB}} \right] \tag{2.84}$$

Here an electronegativity equilibration (EEQ) model is used that has also been applied in the D4 correction scheme [69]. Equation 2.84 can also be expressed in matrix form (Eq. 2.85).

$$E_{IES} = \boldsymbol{q}^{\boldsymbol{T}} \left(\frac{1}{2} \mathbb{A} \boldsymbol{q} - \boldsymbol{X} \right) \tag{2.85}$$

The elements of the vector $\boldsymbol{X}$ are given by Eq. 2.86.

$$X_A = \Omega_A - EN_A \tag{2.86}$$

The elements of the matrix $\mathbb{A}_{AB}$ are given by Eq. 2.87.

$$A_{AB} = \begin{cases} J_{AA} + \frac{2\gamma_{AA}}{\sqrt{\pi}} & for A = B \\ \frac{\operatorname{erf}(\gamma_{AB} R_{AB})}{R_{AB}} & else \end{cases} \tag{2.87}$$

In this equation $\gamma_{AB} = \dfrac{1}{\sqrt{a_A^2 + a_B^2}}$ is a mixing term of the atomic radii a_A and a_B and J_{AA} is the atomic hardness, an element-specific parameter. X_A is the modified electronegativity, which is calculated from the electronegativities that have been mentioned before, and a scaled logarithmic coordination number, Ω_A (Eq. 2.88).

$$\Omega_A = \kappa_A \sqrt{\log \left(\frac{1 + \exp\left(CN_{max}\right)}{1 + \exp\left(CN_{max} - mCN_A\right)} \right)} \tag{2.88}$$

Here κ_A is an element-specific factor, while CN_{max} is the maximally possible coordination number per element and mCN_A is the modified coordination number from the

D3 correction scheme. This modified coordination number is given by equation 2.89.

$$mCN_A = \frac{1}{2}\sum_{B\neq A}\left[1+\mathrm{erf}\left(-7.5\left(\frac{R_{AB}}{R_{AB}^{cov}}-1\right)\right)\right] \tag{2.89}$$

This is implemented in order to ensure reasonable electronegativities in highly coordinated systems. The additional condition that the atomic charges need to sum up to the total charge can be used as a Lagrange multiplier (Eq. 2.90).

$$\begin{pmatrix}\mathbb{A} & 1\\ 1^T & 0\end{pmatrix}\begin{pmatrix}\boldsymbol{q}\\ \lambda\end{pmatrix} = \begin{pmatrix}\boldsymbol{X}\\ q_{tot}\end{pmatrix} \tag{2.90}$$

This gives a set of equations that can be solved in order to obtain the proper charges q_A. In GFN-FF there is an additional set of topology-dependent charges q_t where the interaction between to atoms is not calculated as their direct distance, but as the shortest path of covalent connections between the two atoms. This path is described by equation 2.91.

$$R_{AB}^{topo} = \sum_{i}^{A\rightarrow B}\eta_{topo}R_i^{'cov} \tag{2.91}$$

Here η_{topo} is another global scaling factor. This approach is a cheaper way to include interactions of the chemical environment of an atom than calculating analytical derivatives of the charges. The dispersion energy is calculated analogously to the D3 scheme again (Eq. 2.92).

$$E_{disp}^{(6,8)} = -\sum_{AB}\sum_{n=6,8}s_n\frac{C_{(n)}^{AB}}{R_{AB}^{(n)}}f_{damp}^{(n)}\left(R_{AB}\right) \tag{2.92}$$

Here the coefficients C_6^{AB} are calculated according to equation 2.93, and s_n is for scaling the multipole contributions. $f_{damp}^{(n)}$ is the *Becke-Johnson* damping function.

$$C_6^{AB,D3} = \frac{3}{\pi}\int_0^\infty \alpha^A\left(i\omega\right)\alpha^B\left(i\omega\right)\mathrm{d}\omega \tag{2.93}$$

Here $\alpha\left(i\omega\right)$ are atom specific dynamic polarizabilities, which are also atom specific parameters. These coefficients are then multiplied by charge-scaling functions (ζ) according to Eq. 2.94.

$$C_6^{AB} = \zeta^A\zeta^B C_6^{AB,D3} \tag{2.94}$$

The charge scaling function ζ is calculated from the effective charges by Eq. 2.95.

$$\zeta^A\left(z^A, z^{A,ref}\right) = \exp\left[\beta_1\left\{1-\exp\left[\gamma^A\left(1-\frac{z^{A,ref}}{z^A}\right)\right]\right\}\right] \tag{2.95}$$

Here γ^A is, again, the chemical hardness, while β_1 is a global parameter. The effective nuclear charge z^A is the sum of nuclear charges and topological partial charges $z^A = Z^A + q_t^A$. The reference charges $z^{A,ref}$ are precalculated for reference systems. For hydrogen bonds an additional correction term is introduced. The hydrogen bond energy $E_{HB} = E_{HB}^{A-H\cdots B} + E_{HB}^{A\cdots H\cdots B}$ consists of two cases, where the hydrogen is either bound to the donor A or neither to the donor nor to the acceptor B. Assuming that the hydrogen atom is bound to the donor the energy is given by equation 2.96.

$$E_{HB}^{A-H\cdots B} = -\sum_{AHB} f_{dmp}^{srt} f_{dmp}^{lng} \Upsilon_{dmp}^{out} \chi_{AHB}^{\alpha} \left(\frac{\omega_{AB}}{R_{AB}^3} + \frac{\omega_{BH}}{R_{BH}^3} \right) \tag{2.96}$$

In this equation ω_{AB} and ω_{BH} are global parameters. χ_{AHB}^{α} is used to ensure this contribution vanishes for weak donors of acceptors (Eq. 2.97).

$$\chi_{AHB}^{\alpha} = c_a^A \rho_q^A c_b^B \rho_q^B \rho_q^H \eta_{hb} \tag{2.97}$$

η_{hb} is a global scaling parameter, while c_a^A and c_b^B are global fitting parameters that can be seen as describing the acidity/basicity of A and B. The charge functions ρ_q are calculated from the topological charges and two additional global parameters k_{q1} and k_{q2} (Eq. 2.98).

$$\rho_q^{A,B} = \frac{\exp\left(-k_{q1} q_t^{A,B}\right)}{\exp\left(-k_{q1} q_t^{A,B}\right) + k_{q2}} \tag{2.98}$$

The hydrogen charge dependency is calculated by Eq. 2.99,

$$\rho_q^H = \frac{\exp\left(k_{q1} q_t^H\right)}{\exp\left(k_{q1} q_t^H\right) + k_{q2}} \tag{2.99}$$

The damping functions for short (Eq. 2.100) and long distances (Eq. 2.101) depend on global parameters η_{srt}, γ_{srt}, η_{lng} and γ_{lng} and the covalent radii of the atoms A and B.

$$f_{dmp}^{srt} = \frac{1}{1 + \left(\frac{\eta_{srt} R'^{cov}_{AB}}{R_{AB}^2} \right)^{\gamma_{srt}}} \tag{2.100}$$

$$f_{dmp}^{lng} = \frac{1}{1 + \left(\frac{R_{AB}^2}{\eta_{lng}} \right)^{\gamma_{lng}}} \tag{2.101}$$

Since hydrogen bonds are very angle dependent, an out-of-line damping function is also incorporated by Υ^{out}_{dmp} (Eq. 2.102).

$$\Upsilon^{out}_{dmp} = f^{out}_{H} \prod_{i}^{\Delta_B} f^{out}_{i} \tag{2.102}$$

The first term, f^{out}_{H}, ensures that the hydrogen bond contribution is zero for bent arrangements (Eq. 2.103).

$$f^{out}_{H} = \frac{2}{1 + \exp\left[\frac{\eta^{H}_{out}}{R'^{cov}_{A} + R'^{cov}_{B}} \left(\frac{R_{AH} + R_{BH}}{R_{AB}}\right) - 1\right]} \tag{2.103}$$

η^{H}_{out} is another global parameter. Eq. 2.102 also contains a product of damping functions for the neighbors of the hydrogen acceptor (Eq. 2.104).

$$f^{out}_{i} = \frac{2}{1 + \exp\left[-\frac{\eta^{\Delta}_{out}}{R^{cov}_{A} + R^{cov}_{B}} \left(\frac{R_{Ai} + R_{Bi}}{R_{AB}}\right) - 1\right]} - 1 \tag{2.104}$$

Again, η^{Δ}_{out} is a global parameter. The damping functions are roughly opposed to Eq. 2.103 so their contributions cancel each other out and the hydrogen bond energy becomes zero for linear arrangements with respect to the acceptor atom. This is intended to account for the location of the lone-pair electrons by geometric exclusion. For carbonyl- and nitrogen-groups the approach in Eq. 2.96 is extended by functions for torsion ($f_{tors}(\psi)$) and bending ($f_{bend}(\theta)$) (Eq. 2.105).

$$E^{A-H\cdots B}_{HB} = -\sum_{AHB} f^{srt}_{dmp} f^{lng}_{dmp} \Upsilon^{out}_{dmp} \chi^{\alpha}_{AHB} \left(\frac{\omega_{AB}}{R^3_{AB}} + \frac{\omega_{BH}}{R^3_{BH}}\right) f_{tors}(\psi)\, f_{bend}(\theta) \tag{2.105}$$

These functions allow for the correct angular location of the lone pairs, and thus hydrogen bonds, as expected for a carbonyle. The second case, where $A\cdots H\cdots B$, is built with the same damping functions (Eq. 2.106).

$$E^{A\cdots H\cdots B}_{HB} = -\sum_{AHB} f^{srt}_{dmp} f^{lng}_{dmp} f^{out}_{H} \frac{\chi^{\beta}_{AHB}}{R^3_{AB}} \tag{2.106}$$

The neighbors of the acceptor atoms are not included in the out-of-line damping in this case. In this case the acidity and basicity are given by Eq. 2.107.

$$\chi^{\beta}_{AHB} = \frac{c^{A}_{a} R^4_{BH} + c^{B}_{a} R^4_{AH}}{R^4_{AH} + R^4_{BH}} \cdot \frac{c^{A}_{b} \rho^{A}_{q} R^4_{AH} + c^{B}_{b} \rho^{B}_{q} R^4_{AH}}{R^4_{AH} + R^4_{BH}} \cdot q^{H}_{t} \tag{2.107}$$

For halogen bonds a correction term is included, just as in the semiempirical methods, and it is comprised of damping functions, basicity parameters and charge dependent scaling functions similarly to the hydrogen bond corrections (Eq. 2.108).

$$E_{XB} = -\sum_{DXY} f_{dmp}^{srt} f_{dmp}^{lng} f_X^{out} \frac{\chi_{DXY}^{\alpha}}{R_{XY}^3} \tag{2.108}$$

The strength of the interaction, given by χ_{DXY}^{α} depends only on the halogen and the acceptor (Eq. 2.109).

$$\chi_{DXY}^{\alpha} = c_b^Y \rho_q^Y c_b^X \rho_q^X \tag{2.109}$$

Here c_b are the basicity parameters and ρ_q are the charge dependent scaling functions, as before. This concludes the description of the force field equations for GFN-FF, which have mostly been taken from Ref. 60, except for some correcting modifications to the equations. More additional explanations and descriptions, which have been left out here, can be found in that publication by *Spicher* and *Grimme* [60]. The parametrization of GFN-FF has been done similarly to the SEQM methods, but reference data has been produced using the PBE and the B97 functionals. The same types of data have been used. The training set has mainly been extended to larger molecules and supramolecular structures and a special focus has been laid on highly coordinated transition metal complexes. Again, no special attention has been paid to molecular assembly on surfaces.

2.7 Density Functional Theory (DFT)

DFT is based on the theorem by *Hohenberg* and *Kohn* [70] that the energy is directly corresponding to the electron density ρ of a system. The original motivation was the idea that ρ only depends on three spatial coordinates, while the wave function's dimension increases with the number of electrons, scaling with 4N. The main issue with this idea is the fact that the functional connecting the electron density and the energy is unknown and early attempts delivered poor results. This led to the current *de-facto* standard DFT approach by *Kohn* and *Sham* (KS) [71], which uses an auxiliary set of orbitals to describe the electron density. From this the kinetic energy of the electrons can be calculated and only the exchange and correlation energy have to be described by a functional. These contribute only a fraction of the total energy, and therefore can be approximated by a relatively rough term and still deliver quite good results. In KS-DFT the Hamiltonian is split into multiple parts as described in Eq. 2.110 [72].

$$H_\lambda = T + V_{ext}(\lambda) + \lambda V_{ee} \tag{2.110}$$

The following equations can also be found in Ref. [72]. V_{ext} is an external potential operator, which is equal to the core-electron potential V_{ne} for $\lambda = 1$. For $0 < \lambda < 1$ the operator has to be adjusted so that the same density is obtained. If $\lambda = 0$ the electrons wouldn't interact, enabling an exact solution to the Schrödinger equation as a Slater determinant (Eq. 2.111).

$$T_S = \sum_{i=1}^{N_{elec}} \left\langle \phi_i \left| -\frac{1}{2}\nabla^2 \right| \phi_i \right\rangle \tag{2.111}$$

ϕ_i are molecular orbitals and ∇ is the gradient operator. Since electrons do in fact interact, this is only an approximation. The kinetic energy calculated under this approximation constitutes $\sim 99\%$ of the total kinetic energy, similar to Hartree-Fock (HF). The remaining percent of the total energy can be seen as the exchange-correlation term. The general DFT energy can then be expressed as Eq. 2.112.

$$E_{DFT}[\rho] = T_S[\rho] + E_{ne}[\rho] + J[\rho] + E_{xc}[\rho] \tag{2.112}$$

When setting this equal to the exact energy, one can write the exchange-correlation energy as Eq. 2.113.

$$E_{xc}[\rho] = \underbrace{(T[\rho] - T_S[\rho])}_{\text{kinetic correlation}} + \underbrace{(E_{ee}[\rho] - J[\rho])}_{\text{potential correlation and exchange}} \tag{2.113}$$

Therefore the difference between KS-DFT functionals is in the description of the exchange and correlation. A number of properties that are necessary for the exact functional can also be found in Ref. [72]. In the past decades an entire hierarchy of functionals has developed. First there are the local density approximation (LDA) functionals, that treat the electron density as a uniform electron gas, much like *Hohenberg* and *Kohn* initially described [70]. Generalized gradient approximation (GGA) functionals are generally considered to deliver better results than LDA functionals. The difference is that the first derivative of the electron density is included as an additional variable, and there are also additional restrictions on the integration of Fermi and Coulomb holes. One such functional is named after its' creators *Perdew-Becke-Ernzerhof* (PBE). In the case of this functional the exchange part is simply a function multiplied with the LDA exchange part (Eq. 2.115).

$$\epsilon_x^{PBE} = \epsilon_x^{LDA} F(x) \tag{2.114}$$

$$F(x) = 1 + a - \frac{a}{1 + bx^2} \tag{2.115}$$

The correlation part is an additive term to the LDA correlation part (Eq. 2.120).

$$\epsilon_c^{PBE} = \epsilon_c^{LDA} + h\left(t\right) \tag{2.116}$$

$$H\left(t\right) = cf_3^3 \ln\left[1 + dt^2\left(\frac{1 + At^2}{1 + At^2 + A^2t^4}\right)\right] \tag{2.117}$$

$$A = d\left[\exp\left(-\frac{\epsilon_c^{LDA}}{cf_3^3}\right) - 1\right]^{-1} \tag{2.118}$$

$$f_3\left(\zeta\right) = \frac{1}{2}\left[\left(1+\zeta\right)^{\frac{2}{3}} + \left(1-\zeta\right)^{\frac{2}{3}}\right] \tag{2.119}$$

$$t = \left[2\left(3\pi^3\right)^{\frac{1}{3}} f_3\right]^{-1} x \tag{2.120}$$

The parameters a, b, c and d in this functional have been derived from the aforementioned properties of the exact exchange-correlation functional. The idea of GGA over LDA can of course be extended further by including higher order derivatives of the electron density or the so-called orbital kinetic energy density τ. This results in the next order of density functionals, called meta-GGA functionals. Finally there are hybrid- or hyper-GGA functionals, which incorporate the exact exchange from Hartree-Fock theory for noninteracting electrons and add exchange and correlation terms from various functionals. All of these contributions are then prepended by some empirical factors. Arguably one of the most popular functionals of this category is the B3LYP functional [73], where the energy is calculated via Eq. 2.121.

$$E_{xc}^{B3LYP} = \left(1-a\right)E_x^{LSDA} + aE_x^{exact} + b\Delta E_x^{B88} + \left(1-c\right)E_c^{LSDA} + cE_c^{LYP} \tag{2.121}$$

Where LSDA stands for local spin density approximation, B88 is a functional by *Becke* [74] and LYP is a correlation functional by *Lee*, *Yang* and *Parr* [75]. A final category, called generalized random phase methods, uses a perturbation theory approach for describing the exchange and correlation of the electrons, much like the wavefunction-based Møller-Plesset (MP) perturbation theory [76]. Unfortunately the cost of this is also similar to MP. This concludes the description of the DFT functional hierarchy, however some concluding general remarks should be made.

- DFT delivers much better results than Hartree-Fock at little extra cost.
- DFT generally does not describe van der Waals interactions well[9].
- using supposedly better functionals does not systematically improve the results.

The following section derives the theoretical description of STM imaging from DFT.

[9]This can be improved by using the aforementioned D3 or D4 correction schemes introduced by *Grimme*

2.8 Generating STM images from DFT data

The theoretical description of the STM experiment that is commonly used today, has been introduced by *J. Tersoff* and *D.R. Hamann* [77,78]. In there the tunneling current I_{tunnel} is given as Eq. 2.122.

$$I_{\text{tunnel}} = \frac{2\pi e}{\hbar} \sum_{\mu,\nu} f\left(E_\mu\right) \left[1 - f\left(E_\nu + eV\right)\right] \left|M_{\mu\nu}\right|^2 \delta\left(E_\mu - E_\nu\right) \tag{2.122}$$

Where $f(E)$ is the Fermi function[10], V is the applied voltage, $M_{\mu\nu}$ is the tunneling matrix element between the two states ψ_μ and ψ_ν. However, ψ_μ is a state of the probe and ψ_ν is a state of the surface that is being scanned. E_μ is the energy of the state ψ_μ without tunneling. For typical experimental conditions this can be taken to the limits of small voltage and low temperature in Eq. 2.123.

$$I = \frac{2\pi}{\hbar} e^2 V \sum_{\mu,\nu} \left|M_{\mu\nu}\right|^2 \delta\left(E_\nu - E_F\right) \delta\left(E_\mu - E_F\right) \tag{2.123}$$

Here E_F is the Fermi Energy. In the limit of the tip just being a point probe - which would give the highest possible resolution - the matrix element $M_{\mu\nu}$ becomes proportional to the amplitude of ψ_ν at the position of the probe $\vec{r_0}$ (Eq. 2.124).

$$I \propto \sum_{\nu} \left|\psi_{nu}\left(\vec{r_0}\right)\right|^2 \delta\left(E_\nu - E_F\right) \tag{2.124}$$

The quantity on the right hand side of this equation is the local density of states (LDOS) at the Fermi energy, making the tunneling current proportional to the surface LDOS. Without this simplification a little more work is necessary, which mainly concerns the calculation of the matrix elements $M_{\mu\nu}$ in Eq. 2.125.

$$M_{\mu\nu} = \frac{\hbar^2}{2m} \int \cdot \left(\psi_\mu^* \vec{\nabla} \psi_\nu - \psi_\nu \vec{\nabla} \psi_\mu^*\right) d\vec{S} \tag{2.125}$$

The integral should be evaluated over all surfaces that are entirely in the vacuum region between surface and probe. The expression to be integrated, written in parentheses, is the current operator. The wave function in this expression can be expressed as Eq. 2.126.

$$\psi_\nu = \Omega_s^{-\frac{1}{2}} \sum_G a_G \exp\left[\left(\kappa^2 + \left|\vec{\kappa_G}\right|^2\right)^{\frac{1}{2}} z\right] \exp\left(i\vec{\kappa_G} \cdot \vec{x}\right) \tag{2.126}$$

[10]The Fermi function describes the probability that a given state is occupied by an electron at a given temperature.

Ω_s is the sample volume, $\vec{\kappa_G}$ is the minimum inverse decay length for the wave functions, so basically describes how far the orbitals reach into the empty space. It can be expressed by Eq. 2.127.

$$\kappa = \hbar^{-1} \left(2m\phi\right)^{\frac{1}{2}} \tag{2.127}$$

Here ϕ is the work function. $\vec{\kappa_G}$ consists of two terms, $\vec{k_{||}}$ and $\vec{G}$, which are the surface Bloch wave vector and a surface reciprocal-lattice vector, respectively. The wave functions of the tip are assumed to have asymptotic spherical shape (Eq. 2.128).

$$\psi_\mu = \Omega_t^{-\frac{1}{2}} c_t \kappa R e^{\kappa R} \left(\kappa \left|\vec{r} - \vec{r_0}\right|\right)^{-1} e^{-\kappa|\vec{r}-\vec{r_0}|} \tag{2.128}$$

Here Ω_t is the probe volume, ϕ is assumed to be the same work function as before. Expanding the wave function as for the surface, the matrix elements becomes Eq. 2.129.

$$M_{\mu\nu} = \frac{\hbar^2}{2m} 4\pi\kappa^{-1}\Omega_t^{-\frac{1}{2}} \kappa R e^{\kappa R} \psi_\nu\left(\vec{r_0}\right) \tag{2.129}$$

This can be substituted into Eq. 2.123, and then the current can be expressed as Eq. 2.130

$$I = 32\pi^3\hbar^{-1}e^2 V \phi^2 D_t\left(E_F\right) R^2 \kappa^{-4} e^{2\kappa R} \times \sum_\nu \left|\psi_\nu\left(\vec{r_0}\right)\right|^2 \delta\left(E_\nu - E_F\right) \tag{2.130}$$

D_t is the density of states per unit volume of the probe tip. This, in line with the previously given approximations, results in Eq. 2.131 for the tunneling conductance σ.

$$\sigma \approx 0.1 R^2 e^{2\kappa R} \rho\left(\vec{r_0}, E_F\right) \tag{2.131}$$

With the density of states given as Eq. 2.132

$$\rho\left(\vec{r_0}, E\right) \equiv \sum_\nu \left|\psi_\nu\left(\vec{r_0}\right)\right|^2 \delta\left(E_\nu - E\right) \tag{2.132}$$

This can now be written with physical units: σ is in Ω^{-1}, distances are in a.u. and energy is in eV. When using the Fermi energy in Eq. 2.132, $\rho\left(\vec{r}, E_F\right)$ becomes the surface LDOS at the Fermi energy level at the point $\vec{r}$. For metal tips, an additional simplification to Eq. 2.128 can be made, setting $R = 2\kappa^{-1}$. All in all this gives a simple approximation to a probe with a monoatomic tip, which is the theoretical ideal for STM experiments. For a constant current measurement the probe tip would follow a contour line of $\rho\left(\vec{r}, E_F\right)$.

3 | Publication: Cluster structures influenced by interaction with a surface

3.1 Scope of the project

The scope of this project was to test OGOLEM and its capabilities of global optimization in the context of a cluster on top of a surface. Since Lennard-Jones clusters are well studied systems and common test cases for global optimization they had been chosen as test system. The influence of certain parameters has been investigated, for example the depth of the pairwise potential has been changed to show the influence on the cluster structure. As a less direct effect the distance of the surface atoms has also been investigated. This constitutes the first step into the intended direction of this Thesis.

3.2 Publication Data and Reprint

Reference: C. Witt, J. M. Dieterich, B. Hartke, Physical Chemistry Chemical Physics (Incorporating Faraday Transactions) 2018, 20, 15661–15670.

Submitted: 27.04.2018

Accepted: 23.05.2018

Contribution: Implementation of strain calculation to clusters on surfaces, calculations of homoatomic clusters. Major contributions to the text.

Graphic: Reproduced in fig. 3.1

PCCP

PAPER

View Article Online
View Journal | View Issue

Cite this: *Phys. Chem. Chem. Phys.*, 2018, **20**, 15661

Received 27th April 2018,
Accepted 23rd May 2018

DOI: 10.1039/c8cp02694g

rsc.li/pccp

Cluster structures influenced by interaction with a surface

Christopher Witt, [a] Johannes M. Dieterich[b] and Bernd Hartke *[a]

Clusters on surfaces are vitally important for nanotechnological applications. Clearly, cluster–surface interactions heavily influence the preferred cluster structures, compared to clusters in vacuum. Nevertheless, systematic explorations and an in-depth understanding of these interactions and how they determine the cluster structures are still lacking. Here we present an extension of our well-established non-deterministic global optimization package OGOLEM from isolated clusters to clusters on surfaces. Applying this approach to intentionally simple Lennard-Jones test systems, we produce a first systematic exploration that relates changes in cluster–surface interactions to resulting changes in adsorbed cluster structures.

1 Introduction

After several decades of experimental and computational research on cluster structures and properties *in vacuo*,[1,2] there has been growing interest in clusters on surfaces in recent years. Clearly, clusters on surfaces are much closer to several application areas of current interest, ranging from heterogeneous catalysis[3] to surface-mounted molecular machines or nanotechnology in general.[4] Additionally, today's understanding of cluster structures and properties *in vacuo*, and also the available computational tools, are sufficiently advanced, so that the more difficult situation of clusters in interaction with surfaces can be tackled.

Computational studies of isolated clusters have greatly benefited from broadly shared, simplified model systems that were analyzed in overwhelming detail, for example homogeneous atomic Lennard-Jones (LJ) clusters[5] and pure neutral water clusters.[6] These model systems have served a dual purpose, both ultimately based on their stark simplicity: They were used as benchmark systems for development and refinement of computational methods, but these simplified systems themselves were also studied intensively. For example, for LJ clusters, several intriguing structural transitions as a function of cluster size were discovered. Even after many years of agreement that everything was known for LJ_n with $n < 150$, a completely new structural class was found[7] as new global minimum candidate for LJ_{98}. All these findings could be rationalized, with a varied toolbox that included simple criteria like geometric shell fillings but also more advanced analyses like steric strain,[8] disconnectivity graphs and energy differences of structural classes as a function of cluster size.[9] With the currently accepted minimum-energy structures taken as given, LJ clusters were frequently used to demonstrate performance and size-scaling of global cluster structure optimization algorithms,[10,11] or to introduce refined algorithmic treatments for even better performance.[11–15]

Likewise, pure neutral water clusters served as model system and benchmark system for molecular clusters. Size-dependent structural propensities were elucidated for the simple TIP4P water model,[16,17] and deficiencies of TIP4P in comparison to more sophisticated models were found[18] that were later confirmed by *ab initio* calculations.[19] This benchmark system was also frequently used as basis for fundamental algorithm development.[15,20,21]

The extensive knowledge gathered from these simple model systems provided a solid foundation for exploring more complicated clusters, ranging from simple solvent–solute clusters[22] and clathrate-hydrate clusters[23] all the way to complicated large-molecule clusters with biological importance[24] and to protein folding.[25]

In comparison to this advanced state concerning *in vacuo* clusters, the development for surface-supported clusters is still in its infancy. The central purpose of this Article is to trigger the establishment of simple benchmark and development systems also for clusters on surfaces, by demonstrating that this is a worthwhile goal, since (not surprisingly) due to the additional interaction with a surface there is a broader range of tunables with various interdependencies, but apparently still a chance to arrive at simple, predictive rules and understandings.

Several research groups have examined specific clusters on surfaces in recent years. In a series of papers, Johnston *et al.* have examined small nanoalloy clusters on surfaces, using non-deterministic global optimization at the DFT level, see *e.g.* ref. 26. Additionally, again at the DFT level but without global optimization, they have investigated larger clusters of similar types,[27] finding marked influences of the cluster–surface interactions on the cluster structures.

[a] *Institut für Physikalische Chemie, Christian-Albrechts-Universität, Olshausenstraße 40, D-24098 Kiel, Germany. E-mail: hartke@pctc.uni-kiel.de*
[b] *Mechanical and Aerospace Engineering, Princeton University, Princeton, NJ 08544-5263, USA*

View Article Online
Paper PCCP

Gulia Rossi, Ricardo Ferrando *et al.*[28–32] have used basin-hopping and Gupta-style model potentials to examine pure and binary transition metal clusters (Ni, Ag, Au, Pd, Pt) on MgO-surfaces. Among other phenomena, one of these studies[28] discovered size-dependent structural transitions that sensitively depend on the balance between metal–metal and metal–surface interaction strengths, and generally a strong dependence on differences in preferred atom–atom distances between cluster and surface was noted.

Ciobanu and Ho[33] have implemented evolutionary algorithm (EA) methods for finding optimal reconstructions of semiconductor surfaces. This Ciobanu-Ho EA was then also used to investigate nanowires[34] and cluster structures on surfaces.[35]

Based on this Ciobanu-Ho EA, several other groups have also implemented and/or used EA methods for clusters on surfaces. For example, Shi *et al.* have presented EA search for Pt nanoclusters on graphene,[36] using reactive bond-order potentials with LAMMPS as backend. Sierka, Sauer and Włodarczyk have also developed a similar EA strategy for structures of and on surfaces[37,38] and have used it in applications, for example to investigate water monolayers on MgO(001)[39] and water chains on CaO(001).[40]

Some of the works by Rossi and Ferrando mentioned above have used structural strain in the surface-supported clusters as a diagnostic tool. In contrast, the supporting surface itself is usually taken as a fixed, unchanged entity. There are, however, some works that mention the influence of a strained surface on cluster structures and properties.[41–43]

As indicated above, the idea we promote here is to step back from these already quite advanced but specific application cases to more abstract but also more general model systems, to establish broadly usable benchmarks and to promote understanding of surface-supported clusters by dissecting their multi-faceted interdependencies into simpler pieces. To these ends, we employ structural strain as diagnostic tool, and we modify not only the intra-cluster description but also systematically tune the supporting surface, to elucidate its influence on the clusters attached to it.

2 Computational details

2.1 Global optimization of clusters on surfaces

To find the cluster of a given atomic composition of globally minimal energy in vacuum is commonly considered to be an NP-hard optimization problem.[10,44,45] No indication exists that cluster structure optimization (CSO) on surfaces would not be NP-hard by extension. Hence, deterministic approaches can work in practice only for the smallest problem instances,[46] usually below system sizes of actual interest. To address larger systems, CSO requires the application of stochastic–heuristic algorithms able to reduce the exponential scaling to polynomial.[10] Examples of such algorithms are evolutionary algorithms,[47–49] Monte Carlo with Minimization (MCM)/basin hopping,[50,51] and simulated annealing.[52] We are using evolutionary algorithms through the OGOLEM framework for global optimization.[53] We will here only give a summary of general algorithmic properties while highlighting the ones of importance for this work and extensions thereof. For a general review, and for specific discussions, of OGOLEM algorithms we refer to ref. 20, 21, 24, 54 and 55.

OGOLEM implements an evolutionary pool algorithm[56] in a massively-parallel fashion.[53,57] A pool of solution candidates – in this case atomic arrangements on the surface – is initially filled and subsequently maintained throughout the algorithms's runtime. Two candidates are copied from the pool, one based on the Gaussian-weighted fitness – here minimal total energy – ordering, the other randomly selected. Subsequently, a phenotype crossover operation is applied to the clusters: A randomly positioned plane cuts both original clusters and their upper parts are exchanged. This operation perpetuates and recombines separable parts of existing solution knowledge. With a certain probability, subsequently one atom of the cluster is then moved using, *e.g.*, a Monte Carlo move. This operation explores new solution space. We will discuss surface-specific operations in more detail below.

Obviously, the interactions between cluster and surface depend on the position of the cluster and its orientation. We hence employ three degrees of freedom, the Cartesian components from the center of mass of the cluster to a defined reference atom in the surface. Global optimization of these variables happens simultaneously with the above cluster structure optimization. The exchange of existing knowledge employs a genotype operator, the exploration of new solution space gets a random point within a user-defined space over the surface. This space will typically be a half-sphere or parallelepiped over the center of the surface, with its size designed to avoid clusters venturing beyond the edge of the surface, which may otherwise happen without periodic boundary conditions.

To include the surface into the global cluster structure optimization, we make use of an OGOLEM feature implemented earlier, namely an immutable environment, present throughout the global optimization but with all atoms held fixed at user-predefined positions. Such an environment could be anything, *e.g.*, a cage structure around the cluster. Here we take it to be a flat surface slab with perfect single-crystal geometry, made up from one atom type only. However, it could also be a reconstructed surface, or one with terrace structures on it, or even a heterogeneous surface with nanostructures already present on it. This fixed, pre-defined, user-input surface allows us to trivially force a certain surface symmetry and compression throughout this work. It should be re-emphasized that all surface atoms are constrained, hence no surface rearrangements in response to the adsorbed cluster can occur. This simplified assumption fits into the spirit of the present study that aims at isolating various influences from each other. In real-life applications, this assumption can be avoided, either by post-relaxing the obtained solution candidates while lifting the constraints on the top surface layers (possibly also at a higher level of theory than used during CSO) or by including such a constraint-lifting already in the CSO stage.

Both resulting structures are then checked for sanity: no dissociation of the cluster, no collisions of atoms, and no dissociation of the cluster off the surface. Candidates fulfilling these requirements are locally optimized. An attempt to add the resulting minimum structure of lower total energy to the pool is

then made. Only if the candidate is lower in fitness than the highest-fitness occupant of the pool and satisfies a basic fitness-based diversity criterion, it is added to the pool, with the worst occupant being removed from it.

These operations are repeated thousands of times to arrive at a candidate for the globally minimal solution. Only if several (usually ten) independent runs of considerable length yield the same result do we accept the resulting candidate as converged to a satisfactory standard and list them below.

Most operations for the cluster-on-surface optimization problem themselves are similar to the standard cluster-in-vacuum problem. However, in line with the "no free lunch" theorem[58] for search and optimization, it is not possible to aim at a search algorithm that performs better than all other algorithms across all search problems – or conversely, for any optimization problem, significantly increased optimization efficiency results from incorporating empirical, deterministic, problem-specific knowledge into the search algorithm. Hence, we have exploited the easy adaptability of the EA framework by adding in operations that exploit the fact that we optimize clusters on surfaces. Any existing crossover operation can be made aware of environments (such as surfaces) by using the new vinland algorithm following the general protocol described above. In contrast to most of our standard crossover operators, in case of cluster-environment collisions after any crossover, vinland does not discard this candidate structure but tries to repair this situation by shifting the position of the cluster relative to the environment; this increases the probability of crossover success and hence enhances exploration. We anticipate that this new feature will be particularly valuable for global geometry optimization of 3D-confined systems, but it turns out to be beneficial already for the present situation of clusters on surfaces. For the crossover operations themselves, we use our established N-phenotype cluster crossover sweden[54] as well as a surface-specific norrbotten variant of it, with the added restriction that the cutting plane may only lie perpendicular to the *x*–*y*-plane (assuming the surface itself to lie in *x*–*y*), in order to facilitate phenotype cuts aligned with the surface.

For the mutation operations, we use both a standard mutation for the atoms in the cluster (and random point mutation as detailed above for the degrees of freedom connecting to the environment) as well as the surface-specific flatland mutation which rotates and shifts the entire cluster over the surface, to allow for better exploration of subtle differences of cluster–surface positioning (atop, bridge, hollow site, *etc.*), which turns out to be one key feature that changes in the present work, when we stretch or compress our surfaces. flatland is also employed as a crossover operation. Additionally, the standard local heat pulse mutation,[15] explicit exchange mutation,[54] and advanced graph-based directed mutation[20] are employed.

As explained in the next subsection, the present benchmark work exclusively uses the LJ pair potential built into OGOLEM. However, as described earlier,[53] OGOLEM features a broad array of interfaces to external programs that can be used as backends to supply energies, gradients and/or local optimizations to the ongoing global optimization. Besides specific interfaces to many major program packages in the areas of quantum chemistry, semiempirics and force fields, there also is a generic interface allowing users to attach any other external program as a backend to OGOLEM, for the small price of writing two simple scripts that translate and parse between the documented OGOLEM input/output and the one expected and provided by the external program. In other words, the present work is by no means confined to the very simplistic LJ pair potential but can be transferred easily to other and better levels of theory, essentially only limited by the available computational resources.

Table 1 LJ-parameters used in this work, in atomic units

Atom	σ	ε
Ar	6.434516991	0.000379384
Kr	6.803013559	0.000541524
Xe	7.747876553	0.000699857

2.2 System setup

All structures presented in this work have been globally optimized using the OGOLEM program[53] and its integrated Lennard-Jones potential. The Lennard-Jones pair potential is of standard 6-12-form:

$$v_{ij} = 4\varepsilon_{ij}\left[\left(\frac{\sigma_{ij}}{r_{ij}}\right)^{12} - \left(\frac{\sigma_{ij}}{r_{ij}}\right)^{6}\right] \quad (1)$$

Here, ε_{ij} is the potential well depth, σ_{ij} describes the width of the potential well, and r_{ij} is the distance between the atoms. Standard values[59] for ε and σ are used for pair interactions between atoms of the same type, and traditional Lorentz–Berthelot mixing rules are applied for mixed pair interactions. For completeness, we provide the pure-pair values in Table 1.

Two of the present authors have shown[54] that these traditional choices lead to a partially poor representation of actual rare-gas atom pair interactions and that the potential energy fitting capabilities of OGOLEM can be used to globally fit parameters of a more refined LJ(6,12,2) functional form such that excellent agreement with CCSD(T)/aug-cc-pV5Z reference data is achieved for all possible rare-gas atom pairs. Nevertheless, we use the simpler, traditional mixed LJ model here to allow for easier reproducibility.

Specifically, we examine pure xenon clusters and mixed xenon–krypton clusters on an argon surface. As explained in Section 1, this artificial setup was chosen on purpose, to be able to focus the study on a narrow range of fundamental interactions and tunables. The argon surface consists of three layers of atoms, held at fixed positions throughout the optimizations. This thickness is sufficient since it is beyond the cutoff distance for pair interactions of the cluster atoms, *i.e.*, adding further surface layers would not change the resulting cluster structures or energies. As a basis for this surface, a cif-file was retrieved from the Crystallography Open Database (COD).[60–64] Using the Avogadro software,[65] a (100)-surface slab of 50 by 50 Å has been created from the crystal structure information. The clusters were placed on the surface by the OGOLEM packing algorithm and subsequently optimized. For many systems, the (100)-surface is a commonly studied one in surface science, but otherwise this is an arbitrary choice, for

the present benchmark study. None of the technical ingredients depend on the surface being (100); any other surface could have been used instead. The surface slab edge length of 50 Å ensures that the clusters can be spatially accommodated (including a safety margin), even if spread out into one single layer.

For each optimization of the Xe_{20} cluster a pool of 500 individuals and 500 000 (500k) global optimization steps was employed. In order to ensure that the resulting structures were in fact global minima with a high probability, ten runs of every optimization have been performed, confirming that no lower-energy minima were located in these repeated runs and that the lowest-energy minimum was found repeatedly. Except for one case, where the global minimum candidate was only found three times (or 30%), each candidate has been found at least 5 times (50%) and even 10 times (100%) in most cases. Additionally, it could be shown that the global minimum candidates could be found with significantly less than 500 000 optimization steps. For the optimizations of Xe_{30} clusters the number of global optimization steps has been increased only to 1 000 000 (1 million), since 500k steps were more than sufficient for Xe_{20}. Only in the case of Xe_{30} there was a structure that has been harder to find. This occurred when $\varepsilon_{Xe} = \varepsilon_{Ar}$ and for a few instances where the values differed by one increment.

2.3 Strain calculation

For the present work, the strain approach by Wales *et al.*[8] has been used. It works by separating a pair potential in the following way:

$$V = -n_{nn} + E_{strain} + E_{nnn}. \quad (2)$$

n_{nn} is the number of nearest neighbors and can be written as

$$n_{nn} = \sum_{i<j, r_{ij}<r_0} 1, \quad (3)$$

where r_0 is a cutoff criterion above which interactions are no longer counted as nearest neighbors. Thus, the strain energy simply is the difference in energy between the minimum of the potential and the energy at every given pair distance, within the same cutoff distance:

$$E_{strain} = \sum_{i<j, r_{ij}<r_0} v(r_{ij}) - 1, \quad (4)$$

where 1 is the depth of the potential well (in the usual reduced LJ "units", in which energies are measured in ε and distances in σ) and $v(r_{ij})$ is the potential energy of any given pair. Everything above the distance cutoff is contained in

$$E_{nnn} = \sum_{i<j, r_{ij}\geq r_0} v(r_{ij}). \quad (5)$$

Since all clusters presented in this work are situated on a surface, a small modification of this approach was made. The strain was separated into two terms, in order to separate cluster–cluster interactions and cluster–surface interactions. This made it possible to use different distance cut-offs for cluster–cluster pairs and cluster–surface pairs. This separation would also be useful in order to calculate strain in systems of heterogeneous clusters and surfaces, since it supplies an easy workaround for the varying widths of pair potentials for different atoms.

3 Results and discussion

3.1 Varying the surface geometry

Compressing and stretching a surface changes its interaction with molecules or atoms that are placed on top. If an argon surface is strained enough, it can influence the structure of a cluster placed on top of it. The following surfaces have been compressed and stretched by as much as 20%, to induce such structural changes. We re-emphasize here that this surface stretching is not meant to mimic real-world situations directly but rather is a proxy for a cluster residing on surfaces of different materials, with different interatomic distances. Hence, this allows us to separate two different but usually intertwined influences of different surfaces on a cluster: effects of changing surface geometry and of changing cluster–surface binding energy.

Fig. 1 shows candidates for global minimum-energy structures of clusters on all surfaces that have been strained from −20% to +20% in increments of 5%. These values map to scaling factors from 0.80 to 1.20 in increments of 0.05.

The cluster on the most compressed surface is a particularly peculiar case, because its edges are parallel to the surface slab edges and not all minima of the surface, which could be

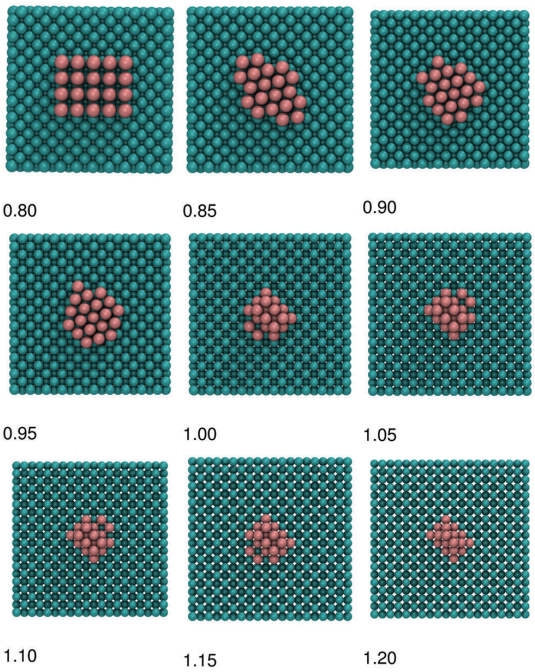

Fig. 1 Candidates for globally optimal Xe_{20} clusters (dark red) on Ar(100) surfaces (dark green) that were compressed or stretched, as indicated by the corresponding scaling factors, relative to the standard surface structure.

considered as places of adsorption, are saturated. All other clusters have a plane of symmetry aligned along a diagonal of the surface slab. Also, there are no hollow sites underneath these clusters. All clusters on the unscaled and on the stretched surfaces are 3-dimensional. While most of these structures consist of two layers, at a scaling factor of 1.2 the cluster has three layers. These layers are stacked in a pyramidal-type shape.

Obviously, stretching or compressing the surface has an influence on the distance between the argon atoms. Therefore the distance between all surface neighbors and xenon atoms on top also changes, which can trigger changes in the relative cluster–surface orientation and/or in the cluster structure. This can be observed particularly well when looking at larger stretching factors (1.0 or more). In these cases the Ar–Xe distances for Xe atoms at Ar-surface hollow sites has become less favorable than for lower stretch values, compared to Xe atoms on Xe–Xe hollow sites, hence this leads to stacking of the xenon atoms. Conversely, for stretch factors dropping below 1.0, the one-layer Xe ad-cluster remains almost unchanged at first, except for minor re-arrangements due to minimal changes in Xe–Xe distances (following the changing Ar–Ar distances in the surface) that subtly modify the energy ordering of Xe-atom locations in the outer (incomplete) 2D-shell. However, at a stretch factor of 0.8 it becomes more favorable for the Xe ad-cluster to re-arrange itself from a 2D-hexagonal form into a 2D-square one (first subpanel in Fig. 1). This 2D-square arrangement implies a Xe–Xe distance distribution shifted towards larger values, which in turn fits better to the Ar–Ar distances in the surface if the whole cluster rotates by 45°.

3.2 Varying the cluster–surface interaction strength

3.2.1 Smaller general clusters. In the previous subsection, Xe clusters on Ar(100) surfaces were examined for differing surface stretch/compression factors, while keeping the Xe–Ar potential well depth constant. Here, we vary the well depth at constant surface geometry. The well depths for both xenon and argon have been varied from 1×10^{-4} to 9×10^{-4} in steps of 1×10^{-4}. The resulting cluster strain behavior for Xe_{20} can be seen in Fig. 2. To allow for direct comparisons despite varying well depths, all strains have been normalized to a common well depths value, making the unit on the *y*-axis of the plot arbitrary.

This plot reveals a fairly regular behaviour when changing the potential well depths of argon and xenon: the graphs for each value of ε_{Ar} essentially are shifted copies of each other; in other words, the important quantity is the ratio of the two well depths.

Additionally, strain changes in Fig. 2 can be correlated with cluster structure changes: as long as the potential well depth for xenon is lower than the potential well depth for argon, a simple monolayer forms, with all its atoms on minima positions on the surface, *cf.* Fig. 3. This cluster can be seen as a continuation of the (100)-face fcc structure of the surface.

Once ε_{Xe} and ε_{Ar} are equal, the structure changes to a different type of monolayer, shown in Fig. 4. This cluster structure can be described as a (111)-face in the middle and (100)-face towards the sides. The cluster is symmetric with respect to its diagonal. With this structural change comes a relief in cluster strain and a slight increase in surface strain.

Fig. 5 shows all structures corresponding to one line in Fig. 2 from left to right and from top to bottom. After the change in the 2D cluster structure discussed above, the next step in ε_{Xe} creates 3D clusters. At first these 3D clusters show the same packing as the 2D cluster in Fig. 3. The change between these

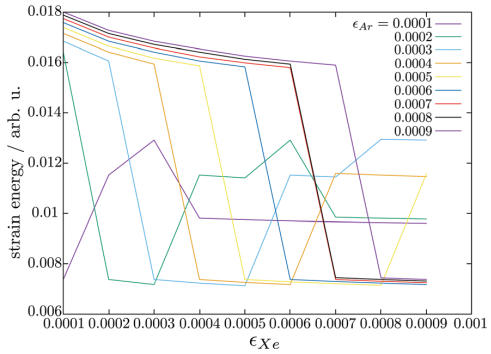

Fig. 2 Plot of strain energy within a Xe_{20} cluster *vs.* xenon potential well depth.

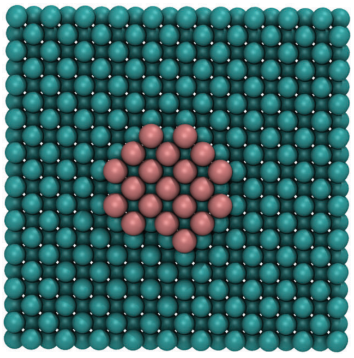

Fig. 3 Xe_{20}@Ar(100) for $\varepsilon_{Xe} < \varepsilon_{Ar}$.

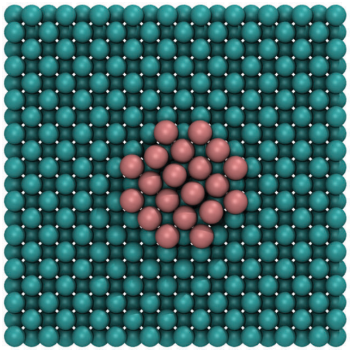

Fig. 4 Xe_{20}@Ar(100) for $\varepsilon_{Xe} = \varepsilon_{Ar}$.

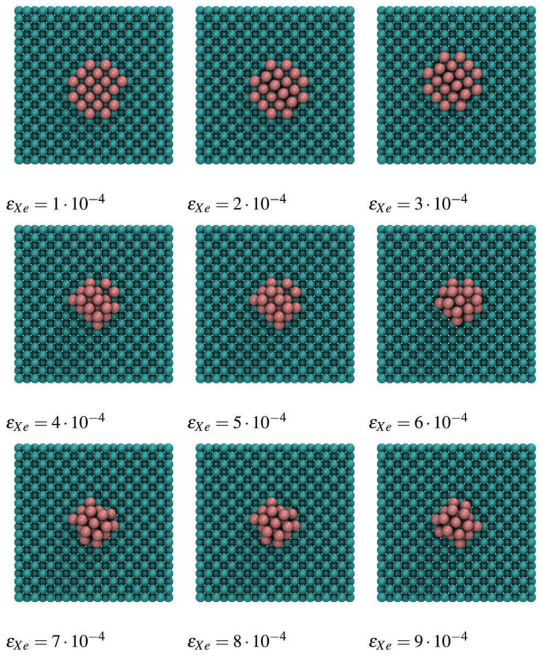

Fig. 5 Xe_{20}@Ar(100) for constant ε_{Ar} = 0.0002, and with ε_{Xe} increasing from top left to bottom right.

structures is accompanied by a huge relief in surface strain, since less cluster atoms are connected to the surface. The final structural change can be compared to the different packing between the two types of 2D clusters, since their tops also show a (100)- and a (111)-face, respectively.

The same strain calculations have been done for Xe_{30} on the same surface. As illustrated in Fig. 6, a behavior similar to that of the Xe_{20} clusters is obtained.

3.2.2 Larger clusters of special sizes. Larger Xe-clusters allow for further interesting observations: for certain cluster sizes,[10,14,51] the structure search landscape for homogeneous

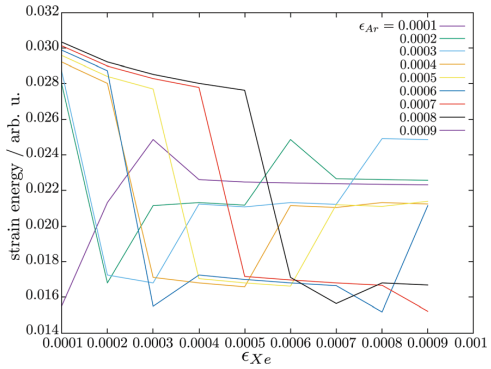

Fig. 6 Plot of strain energy within a Xe_{30} cluster *vs.* xenon potential well depth.

Lennard-Jones clusters in vacuum takes on a challenging, deceptive characteristic, with the standard icosahedral structures residing in a funnel dominating most of the landscape, while the truly global minimum resides in a smaller-volume funnel, separated by high-energy barriers. Cluster size n = 38 is the smallest one with such a challenging landscape, but there the minor funnel containing the global minimum hosts fcc structures that are inherently compatible with attachment to a surface. For n = 75, however, both the large icosahedral funnel and the small decahedral funnel (containing the global minimum) feature 5-fold symmetry axes that are not commensurable with surface attachment.

Hence, we have examined which global minimum-energy structures are attained by a Xe_{75} cluster on an Ar(100) surface if again the Xe and Ar LJ well depths are detuned away from their standard values. Fig. 7 illustrates the main findings: for a

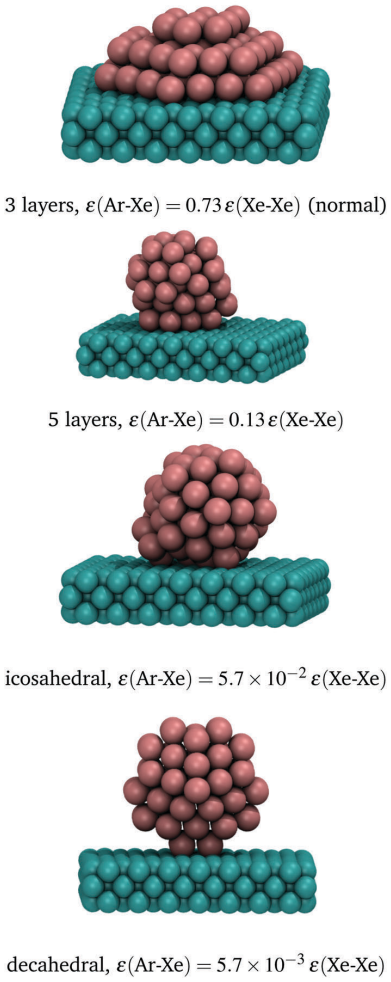

Fig. 7 Xe_{75} on Ar(100), for varying Lennard-Jones well-depth ratios (Ar–Xe) : (Xe–Xe). View angles deliberately differ slightly between the four panels, to make the Xe cluster structures more obvious.

(Ar–Xe)/(Xe–Xe) well depth ratio corresponding to the standard well depths, a 3-layer structure is preferred. As to be expected, and in line with the series of Xe_{20} structures shown in Fig. 5, when the Ar–Xe well depth is made smaller, the Xe ad-cluster develops more layers, and for sufficiently small Ar–Xe well depths, Xe cluster structures resembling isolated vacuum structures arise. Interestingly, however, the first free-cluster-like structures that occur are icosahedral. Only for still significantly smaller Ar–Xe well depth, the decahedral structure is formed, corresponding to the true global minimum in vacuum. This indicates that in vacuum the slightly lower energy of the decahedral structure, compared to the icosahedral one, is a very delicate matter. Already attachment to a surface *via* an extraordinarily weak interaction suffices to make the ubiquitous icosahedral structure more favorable.

For heterogeneous clusters, surface-attachment may influence not only the overall structure but also the distribution of the species in the cluster. As an illustration, we show exemplary results from $Kr_{19}Xe_{19}$ on Ar(100), again for varying LJ pair potential well depths ε.

For standard ε-values, the resulting global minimum candidates exhibit structures in line with the above ones for homogeneous Xe clusters, as shown in Fig. 8. Within the cluster, Kr and Xe atoms arrange themselves in a striped pattern, which helps to relief interface strain.

Compared to the above case, when scaling down either only the Kr or only the Xe ε-value by a factor of 10, the overall 2-layer structure is retained but the stripey distribution of Kr and Xe within the ad-cluster is changed to a core–shell-like distribution, with the more weakly bond species on the outside (*cf.* Fig. 9).

If the LJ pair potential well depth is scaled down by a factor of 10 for both Kr and Xe, the cluster–surface interactions are larger and the intra-cluster interactions weaker (compared to the standard case). Hence, predictably, 1-layer structures result, as shown in Fig. 10, and again the cluster species form stripey/patchy patterns to relief strain.

In the above case, both Kr and Xe ε values were scaled down by the same amount. If the Xe ε is scaled down by 10 and the Kr ε by 100, however, the ad-cluster structure shown in Fig. 11 is obtained. The pronounced segregation in the 1D-layer-structure matches the now unsymmetrically scaled Xe–Xe, Kr–Kr and Xe–Kr interactions.

In contrast, if the ε-values for Kr and Xe are kept at their standard values and only the Ar one is scaled down by 10, the very different and surprising structure shown in Fig. 12 arises. The difference to the previous cases is that compared to the cluster–surface interactions now the Kr–Xe interaction is not scaled down and hence is comparatively stronger. This rationalizes the marked change from a 1-layer to a 3-layer structure.

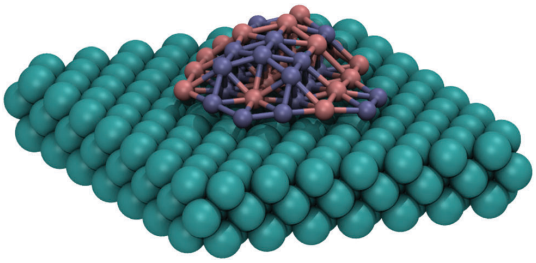

Fig. 8 $Kr_{19}Xe_{19}$ on Ar(100), for standard LJ ε values.

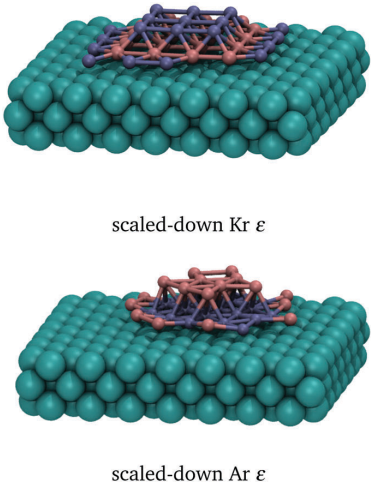

Fig. 9 $Kr_{19}Xe_{19}$ on Ar(100), with either only the Kr or the Xe ε value scaled down by a factor of 10.

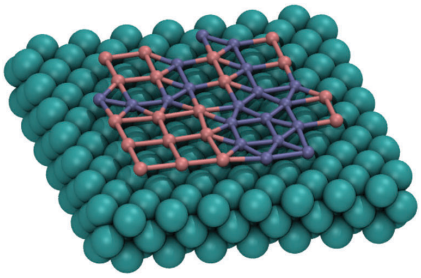

Fig. 10 $Kr_{19}Xe_{19}$ on Ar(100), for both Kr and Xe ε values scaled down by a factor of 10.

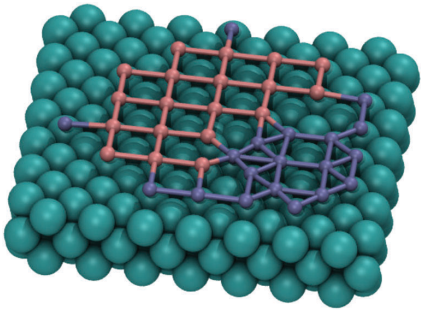

Fig. 11 $Kr_{19}Xe_{19}$ on Ar(100), for Xe ε values scaled down by 10 and Kr ε scaled down by 100.

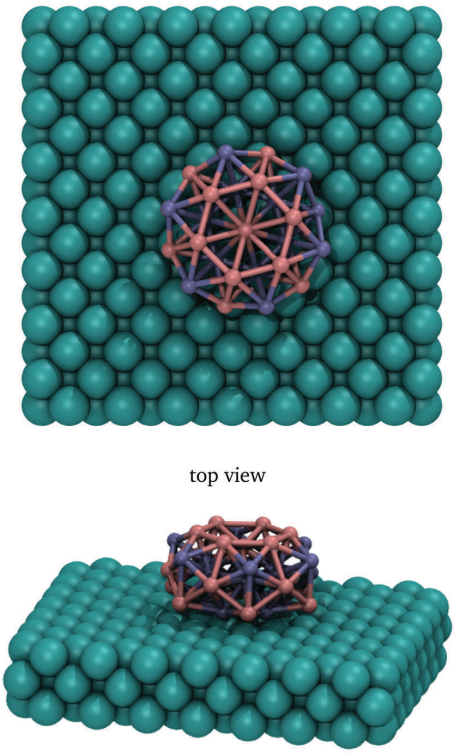

Fig. 12 $Kr_{19}Xe_{19}$ on Ar(100), with only the Ar ε value scaled down by a factor of 10. For clarity, the same structure is shown from two different viewpoints.

Scaling down the ε-values for both Kr and Ar leads to the structure shown in Fig. 13. In this setting, only the Xe–Xe interaction is unaffected, and relatively stronger than all others; hence the resulting core–shell structure with Xe inside and Kr outside is understandable. However, it is somewhat surprising that already at these comparatively small ε-detunings, the Xe core takes on an icosahedral shape (in contrast to the findings shown in Fig. 5). Apparently, this is a combined effect of a

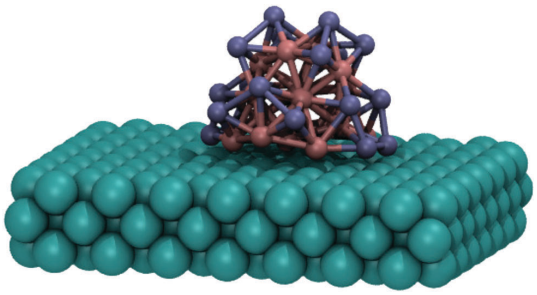

Fig. 13 $Kr_{19}Xe_{19}$ on Ar(100), for Kr and Ar ε values scaled down by a factor of 10.

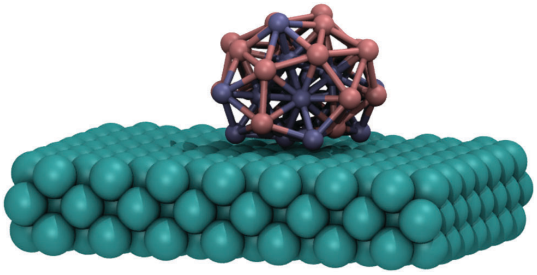

Fig. 14 $Kr_{19}Xe_{19}$ on Ar(100), for an Ar ε value scaled down by a factor of 100.

weaker Xe–Ar interaction (*via* the Lorentz–Berthelot mixing rules) and of the Kr shell helping to prevent the Xe icosahedron from collapsing into a more surface-commensurate 2- or 3-layer structure without partial 5-fold symmetry axes.

A similar icosahedral structure results if only the Ar ε value is scaled down by a factor of 100 (*cf.* Fig. 14). Since now the Xe and Kr well depth both are at their original values, the core–shell structure is now punctured by stripe/patch-like species alternations. Additionally, now Kr is inside and Xe outside, due to the larger size of the latter (in isolated, homogeneous icosahedral structures, the core is compressed and the hull elongated, so there is more room on the outside than on the inside).

4 Conclusions and outlook

In a deliberately simple and abstract setting of pure Xe and mixed Xe/Kr clusters on Ar surfaces, we have shown how systematic detuning of surface atom distances (stretching/compressing the surface) and of LJ pair potential well depths change the structures of the adsorbed clusters. These changes can be rationalized with straightforward tools like strain analysis and (in this simple setting) with human insight. Nevertheless, already for these abstract test cases, the range of different structures and phenomena is very wide. Hence we are confident that fundamental studies of the present kind will greatly help to elucidate and understand the even broader variability of cluster–surface interactions in real-life applications. Real-life applications of the computational technology presented here essentially encompass anything that revolves around molecular structures on surfaces, for example generating patterned and/or functionalized surfaces by attaching nano-sized entities to surfaces *via* molecular tethers, or elucidating structure–function relationships of arrangements of reactant and promoter molecules in heterogeneous catalysis. In fact, by including several surface layers into that part of the system that is not rigid but is included in the global optimization operations, even surface heterostructures and surface reconstructions (on themselves, or as reaction to cluster attachment) become accessible, which opens up possible application areas even further. Work along these lines is in progress in our lab.

Conflicts of interest

There are no conflicts of interest to declare.

Acknowledgements

JMD wishes to thank Dean Emily Carter for her support of his other scientific endeavours. BH gratefully acknowledges financial support by the German Science Foundation DFG under grant Ha2498/16-1.

Notes and references

1 A. W. Castleman and K. H. Bowen, *J. Phys. Chem.*, 1996, **100**, 12911.
2 A. Sanov and W. C. Lineberger, *Phys. Chem. Chem. Phys.*, 2004, **6**, 2018–2032.
3 J. Sauer and H.-J. Freund, *Catal. Lett.*, 2015, **145**, 109–125.
4 F. Klappenberger, *Prog. Surf. Sci.*, 2014, **89**, 1–55.
5 J. A. Northby, *J. Chem. Phys.*, 1987, **87**, 6166.
6 U. Buck, C. C. Pradzynski, T. Zeuch, J. M. Dieterich and B. Hartke, *Phys. Chem. Chem. Phys.*, 2014, **16**, 6859–6871.
7 R. H. Leary and J. P. K. Doye, *Phys. Rev. E: Stat. Phys., Plasmas, Fluids, Relat. Interdiscip. Top.*, 1999, **60**, R6320.
8 J. P. Doye and D. J. Wales, *Chem. Phys. Lett.*, 1995, **247**, 339–347.
9 J. P. K. Doye, M. A. Miller and D. J. Wales, *J. Chem. Phys.*, 1999, **111**, 8417.
10 B. Hartke, *J. Comput. Chem.*, 1999, **20**, 1752.
11 H. Takeuchi, *J. Chem. Inf. Model.*, 2007, **46**, 2066–2070.
12 X. Shao, X. Yang and W. Cai, *J. Comput. Chem.*, 2008, **29**, 1772–1779.
13 I. Georgescu and V. A. Mandelshtam, *J. Chem. Phys.*, 2011, **135**, 154106.
14 M. Dittner and B. Hartke, *Comput. Theor. Chem.*, 2017, **1107**, 7–13.
15 J. M. Dieterich and B. Hartke, *Inorganics*, 2017, **5**, 64.
16 D. J. Wales and M. P. Hodges, *Chem. Phys. Lett.*, 1998, **286**, 286.
17 B. Hartke, *Z. Phys. Chem.*, 2000, **214**, 1251.
18 B. Hartke, *Phys. Chem. Chem. Phys.*, 2003, **5**, 275.
19 A. Lagutschenkov, G. S. Fanourgakis, G. Niedner-Schatteburg and S. S. Xantheas, *J. Chem. Phys.*, 2005, **122**, 194310.
20 J. M. Dieterich and B. Hartke, *J. Comput. Chem.*, 2014, **35**, 1618.
21 J. M. Dieterich and B. Hartke, *Phys. Chem. Chem. Phys.*, 2015, **17**, 11958–11961.
22 F. Schulz and B. Hartke, *Theor. Chem. Acc.*, 2005, **114**, 357.
23 B. Hartke, *J. Chem. Phys.*, 2009, **130**, 024905.
24 J. M. Dieterich, U. Gerstel, J.-M. Schröder and B. Hartke, *J. Mol. Model.*, 2011, **17**, 3195.
25 F. Koskowski and B. Hartke, *J. Comput. Chem.*, 2005, **26**, 1169.
26 J. B. A. Davis, S. L. Horswell and R. L. Johnston, *J. Phys. Chem. C*, 2016, **120**, 3759–3765.
27 I. Demiroglu, T.-E. Fan, J. Yuan, T.-D. Liu, L. Piccolo and R. L. Johnston, *Faraday Discuss.*, 2018, DOI: 10.1039/C7FD00213K.
28 G. Rossi, C. Mottet, F. Nita and R. Ferrando, *J. Phys. Chem. B*, 2006, **110**, 7436–7442.
29 R. Ferrando, G. Rossi, A. C. Levi, Z. Kuntová, F. Nita, A. Jelea, C. Mottet, G. Barcaro, A. Fortunelli and J. Goniakowski, *J. Chem. Phys.*, 2009, **130**, 174702.
30 J. Goniakowski, A. Jelea, C. Mottet, G. Barcaro, A. Fortunelli, Z. Kuntová, F. Nita, A. C. Levi, G. Rossi and R. Ferrando, *J. Chem. Phys.*, 2009, **130**, 174703.
31 G. Rossi, L. Anghinolfi, R. Ferrando, F. Nita, G. Barcaro and A. Fortunelli, *Phys. Chem. Chem. Phys.*, 2010, **12**, 8564–8570.
32 D. Bochicchio, R. Ferrando, E. Panizon and G. Rossi, *J. Phys.: Condens. Matter*, 2016, **28**, 064005.
33 F. C. Chuang, C. V. Ciobanu, V. B. Shenoy, C. Z. Wang and K. M. Ho, *Surf. Sci.*, 2004, **573**, L375–L381.
34 C. V. Ciobanu, C.-Z. Wang and K.-M. Ho, *Mater. Manuf. Processes*, 2009, **24**, 109–118.
35 F.-C. Chuang, B. Liu, C.-Z. Wang, T.-L. Chan and K.-M. Ho, *Surf. Sci.*, 2005, **598**, L339–L346.
36 H. Shi, S. M. Auerbach and A. Ramasubramaniam, *J. Phys. Chem. C*, 2016, **120**, 11899–11909.
37 M. Sierka, *Prog. Surf. Sci.*, 2010, **85**, 398–434.
38 R. S. Włodarczyk, PhD thesis, HU Berlin, 2015.
39 R. Włodarczyk, M. Sierka, K. Kwapień and J. Sauer, *J. Phys. Chem. C*, 2011, **115**, 6764–6774.
40 X. Zhao, X. Shao, Y. Fujimori, S. Bhattacharya, L. M. Ghiringhelli, H.-J. Freund, M. Sterrer, N. Nilius and S. V. Levchenko, *J. Phys. Chem. Lett.*, 2015, **6**, 1204–1208.
41 R. F. Sabiryanov, M. I. Larsson, K. J. Cho, W. D. Nix and B. M. Clemens, *Phys. Rev. B: Condens. Matter Mater. Phys.*, 2003, **67**, 125412.
42 R. G. S. Pala and F. Liu, *J. Chem. Phys.*, 2004, **120**, 7720–7724.
43 G. Kim, Y. Kawazoe and K.-R. Lee, *J. Phys. Chem. Lett.*, 2012, **3**, 1989–1996.
44 L. T. Wille and J. Vennik, *J. Phys. A: Math. Gen.*, 1985, **18**, L419.
45 G. W. Greenwood, *Z. Phys. Chem.*, 1999, **211**, 105.
46 B. Hartke, *Wiley Interdiscip. Rev.: Comput. Mol. Sci.*, 2011, **1**, 879–887.
47 J. H. Holland, *Adaption in natural and artificial systems*, University of Michigan Press, Ann Arbor, MI, 1975.
48 D. E. Goldberg, *Genetic algorithms in search, optimization and machine learning*, Addison-Wesley, Reading, MA, 1989.
49 T. Weise, *Global Optimization Algorithms – Theory and Application*, 3rd edn, 2011, www.it-weise.de, accessed: 17-Aug-2014.
50 Z. Li and H. A. Scheraga, *Proc. Natl. Acad. Sci. U. S. A.*, 1987, **84**, 6611–6615.
51 D. J. Wales and J. P. K. Doye, *J. Phys. Chem. A*, 1997, **101**, 5111.
52 S. Kirkpatrick, C. D. Gellat, Jr. and M. P. Vecchi, *Science*, 1983, **220**, 671.
53 J. M. Dieterich and B. Hartke, *Mol. Phys.*, 2010, **108**, 279–291.
54 J. M. Dieterich and B. Hartke, *J. Comput. Chem.*, 2011, **32**, 1377–1385.
55 J. M. Dieterich and B. Hartke, *Appl. Math.*, 2012, **3**, 1552–1564.
56 B. Bandow and B. Hartke, *J. Phys. Chem. A*, 2006, **110**, 5809–5822.
57 J. M. Dieterich and B. Hartke, *J. Chem. Theory Comput.*, 2016, **12**, 5226–5233.
58 D. H. Wolpert and W. G. Macready, *IEEE T. Evolut. Comput.*, 1997, **1**, 67.

59 R. S. Berry, S. A. Rice and J. Ross, *Physical Chemistry*, Wiley, New York, 1980.
60 R. T. Downs and M. Hall-Wallace, *Am. Mineral.*, 2003, **88**, 247–250.
61 A. Merkys, A. Vaitkus, J. Butkus, M. Okulič-Kazarinas, V. Kairys and S. Gražulis, *J. Appl. Crystallogr.*, 2016, **49**, 292–301.
62 S. Gražulis, A. Merkys, A. Vaitkus and M. Okulič-Kazarinas, *J. Appl. Crystallogr.*, 2015, **48**, 85–91.
63 S. Gražulis, A. Daškevič, A. Merkys, D. Chateigner, L. Lutterotti, M. Quirós, N. R. Serebryanaya, P. Moeck, R. T. Downs and A. Le Bail, *Nucleic Acids Res.*, 2012, **40**, D420–D427.
64 S. Gražulis, D. Chateigner, R. T. Downs, A. F. T. Yokochi, M. Quirós, L. Lutterotti, E. Manakova, J. Butkus, P. Moeck and A. Le Bail, *J. Appl. Crystallogr.*, 2009, **42**, 726–729.
65 M. D. Hanwell, D. E. Curtis, D. C. Lonie, T. Vandermeersch, E. Zurek and G. R. Hutchison, *J. Cheminf.*, 2012, **4**, 1–17.

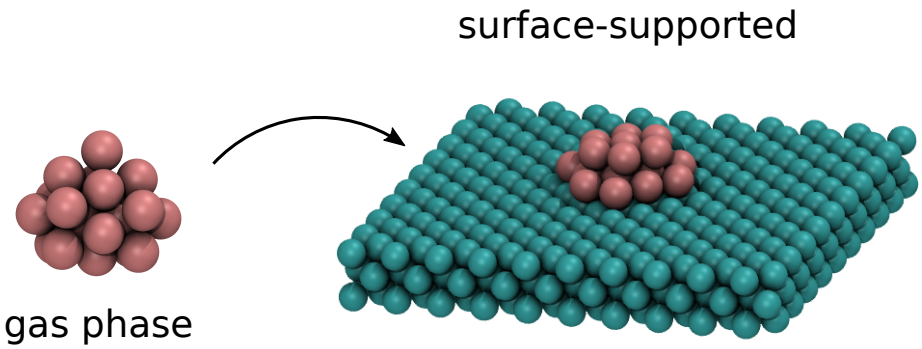

Figure 3.1: TOC graphic for the presented paper.

4 | Global Optimization of Molecules on a Surface

In order to do global optimization of molecules on a surface, one needs a good method for the local optimization steps. These methods should:

1. be fast,
2. not need static bond information (for cluster-surface interactions),
3. be stable outside of local minima,
4. be available for a large range of elements.

It needs to be reasonably fast, because a lot of local optimization cycles will occur during global optimizations. The cluster-surface interactions should not be described by static bonds, because that would severely limit the search space for the optimization, and for example not allow for a molecule to be desorbed. If the used method does not provide reasonable data outside of a narrow range around certain local minima, then a situation might arise during a global optimization run that leads to entirely wrong structures. Having a method that is available over a large range of atoms is not strictly necessary, it is just generally useful. A number of methods have been tested during the work for this thesis:

1. ReaxFF [50, 51]
2. DFTB [57, 62]
3. xtb semiempirics [58, 59] (namely GFN-1 and GFN-2)
4. OPLS-aa [43]
5. xtb GFN-FF [60]

In the following sections some of the results for each of these methods will be discussed. For all upcoming calculations shown, the surface has been optimized to the same DFT lattice parameters for bulk platinum. The surface slab has been held fixed during all local optimizations.

4.1 DFTB

DFTB has been considered as an option for the locopt backend briefly, but the lack of parameters for most metallic elements prohibited the use of this method for the considered systems. There are some parameter sets that do contain one or sometimes multiple metals, but these were often parametrized for very specific types of compounds [80, 81][1]. This method could however be very useful, if a parametrization effort was made. An attempt has however been made to see if DFTB is a viable option. An optimization of silicon on Si(100) has been done, which yielded a minimum structure where the cluster continued the pattern of the surface.

4.2 GFN-xtb semiempirics

The semiempirical extended tight binding method GFN-xtb has been tested in two of the three available variants, namely GFN1 and GFN2. However, for GFN2 the self-consistent-charge (SCC) cycle fails to converge for the metal surface slabs that have been targeted in this work. For GFN1 it could be shown that aluminum slabs can indeed be used within an optimization. One example of this is shown in Fig. 4.1, where seven aluminum atoms have been optimized on an Al(100) surface. This could e.g. be useful to investigate growth patterns of either clusters or surface layers on a surface. This and all following molecular structure images in this thesis have been generated using VMD [82].

[1] see also dftb.org/parameters for examples. For example, the pbc dataset contains parameters for C, H, N, F and O, but only in conjunction with Si thus only allowing for silicon surfaces. Similarly, the matsci parameter set has only few interactions between certain metals and C, H, O.

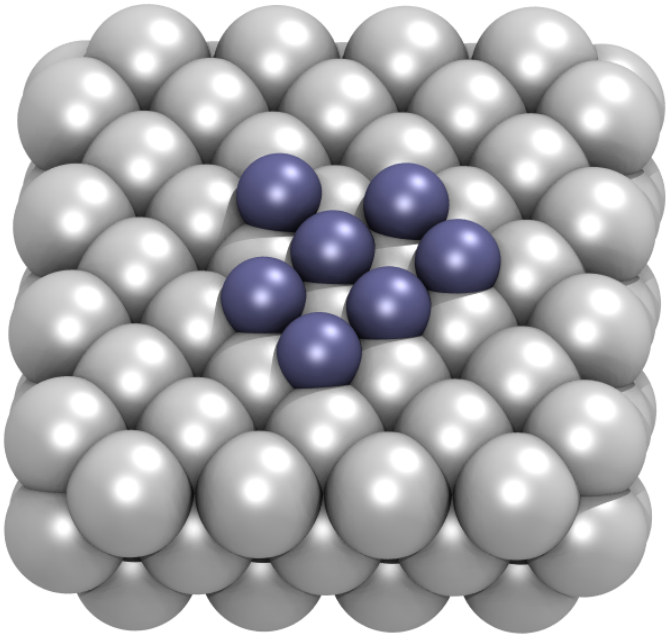

Figure 4.1: Seven aluminum atoms globally optimized on top of an Al(100) surface using OGOLEM and GFN1. (Image generated using VMD [82])

4.3 Benzene

There is a ReaxFF parameter set for platinum, nickel, carbon, hydrogen and oxygen [56]. Within Ref. 56, the parameter set has been applied to molecules or fragments that have not been larger than a methyl group. This parameter set has been tested on benzene and acetophenone by *Niklas Crome* during his Bachelor's thesis. The resulting gas phase data seemed reasonable, the data for surface adsorbed molecules, however, did not deliver expected results. In this section, there will first be a short description of the typical adsorption behavior of benzene, then the results from *Niklas Crome* will be shown and finally additional results by the author of this thesis will be added. Fig. 4.2 shows the eight high symmetry positions that are possible for a benzene molecule on an fcc-metal(111) surface. Of these positions the bri30° position has been found to be the energetically most favorable adsorption position by *Liu et al.* [83] using DFT calculations. In the calculations by *Niklas Crome* the molecule clusters were initialized too far away from the surface, resulting in poor surface adsorption. For example, in the case of only one benzene molecule the structure in Fig. 4.3 was obtained within 25k global optimization steps.

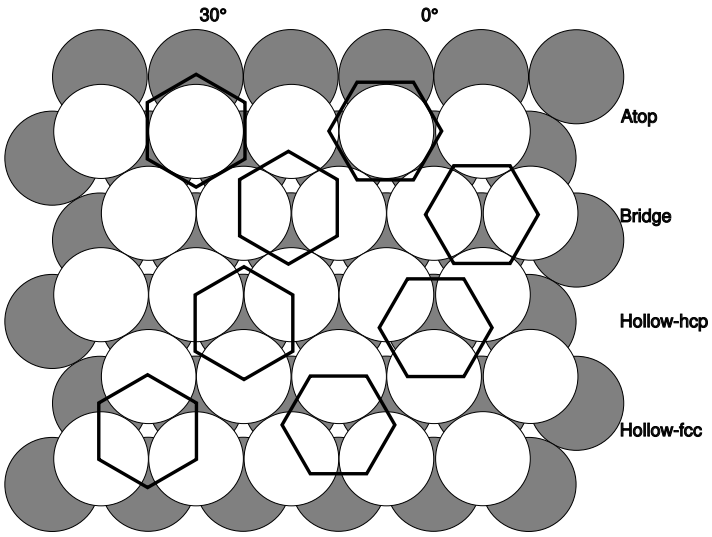

Figure 4.2: Schematic image of the 8 high symmetry adsorption positions of benzene on an fcc-metal(111) surface.

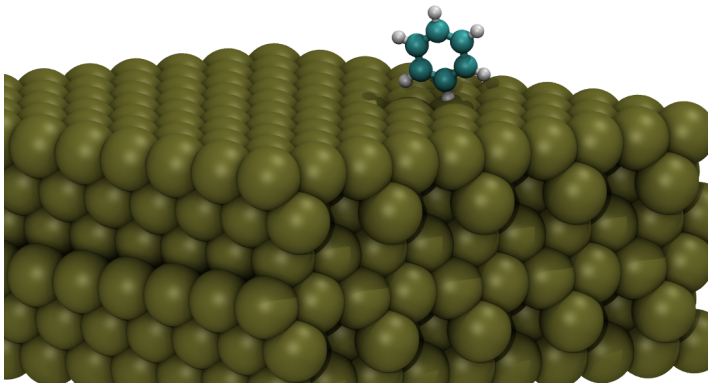

Figure 4.3: Rendered image of the optimization result for a single benzene molecule on a Pt(111) surface as obtained by *Niklas Crome*.

This optimization has been rerun by the author of this thesis where the only change to the input was the distance at which the molecules were spawned with respect to the surface. The result of this optimization run is being shown in Fig. 4.4. This adsorption geometry agrees well with the results by *Liu et al.* [84].

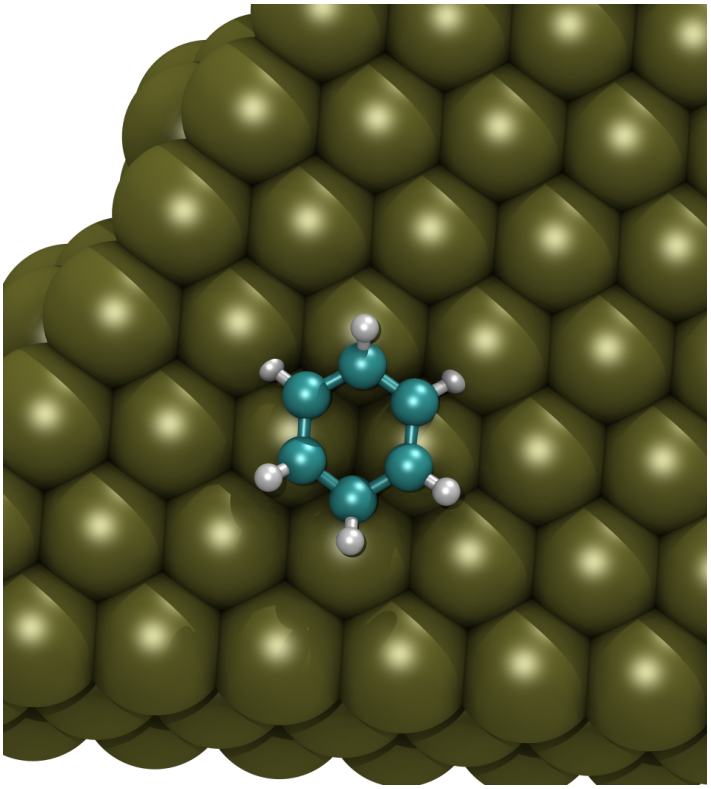

Figure 4.4: Benzene adsorbed on Pt(111) surface in bri30° position as found by global optimization with OGOLEM and ReaxFF.

Benzene dimers in the gas phase can appear in two possible configurations that only differ by about 0.15 kcal/mol according to calculations by *Hobza et al.* [85]. The global minimum is a "parallel displaced" structure where one C-H bond is positioned ontop of the other benzene rings center. The second best structure, a "T-shaped" one, has been found to be better than the "parallel displaced" one in other works on gas phase benzene clusters [86], where the 6-31G* basis set has been used. However, the previous work by *Hobza et al.* had specifically shown that diffuse basis functions are essential for correctly describing these benzene dimers, therefore the ordering of the minima as described above is considered to be the correct one. There is not much information about benzene dimers on a metal surface specifically, but *Saeys et al.* describe the dimer as one benzene molecule on a hollow site and the second molecule di-σ adsorbed and tilted on the first benzene molecule [87]. However the basis set used due to computational expense was a double-ζ basis set, which may have lead to incorrect structures due to the reasons discussed above. In figure 4.5 the best benzene dimer found by a global optimization run of 25k steps is shown. There are two benzene molecules on top of each other, similar to the gas phase "parallel displaced" configuration, with the lower benzene molecule in the top0° adsorption position. Compared to *Saeys et al.* this may

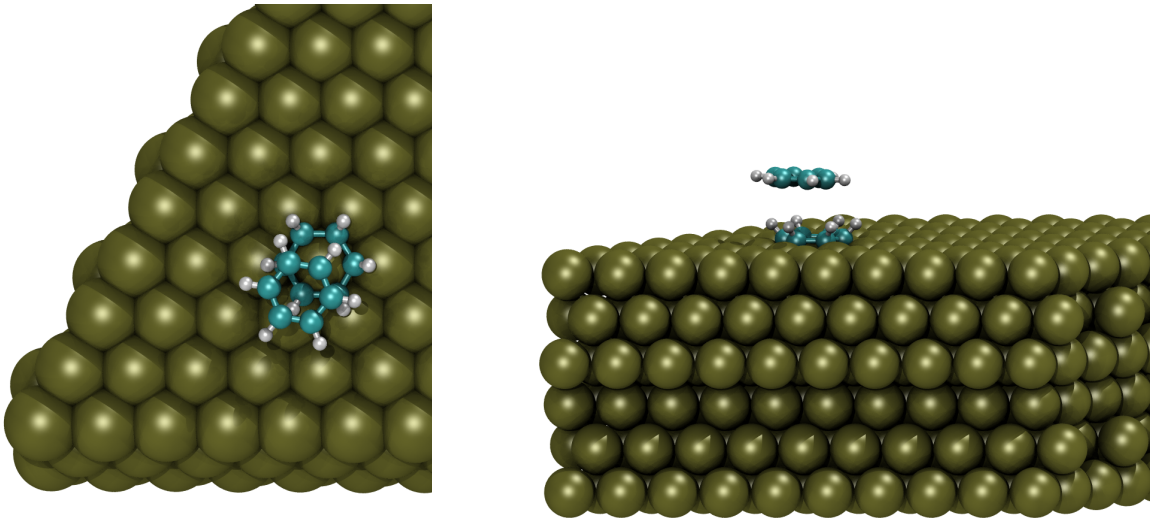

Figure 4.5: Parallel displaced benzene dimer adsorbed on Pt(111) surface as found by global optimization with OGOLEM and ReaxFF.

Table 4.1: Absolute energies of the benzene dimers that have been found using ReaxFF

structure	energy / kJ/mol
parallel displaced	-12438.67
t-shape	-12437.22
both on surface	-21628.58

indicate an overestimation of the molecule-molecule interactions over the molecule-surface interactions in the ReaxFF parametrization. Another adsorbed dimer that has been found in another optimization run was similar to the T-shaped gas phase dimer (Fig. 4.6). The energy difference between these two structures is $\Delta E = -0.44$ kcal/mol, which is in accordance with the previously discussed gas phase results. In addition to these results another run with 500k steps has been done. This resulted in the two benzene molecules, both adsorbed in bridge positions next to each other, shown in Fig. 4.7. The absolute energies of these three minima, given in Table 4.1, illustrate the strong surface interaction of the benzene ring.

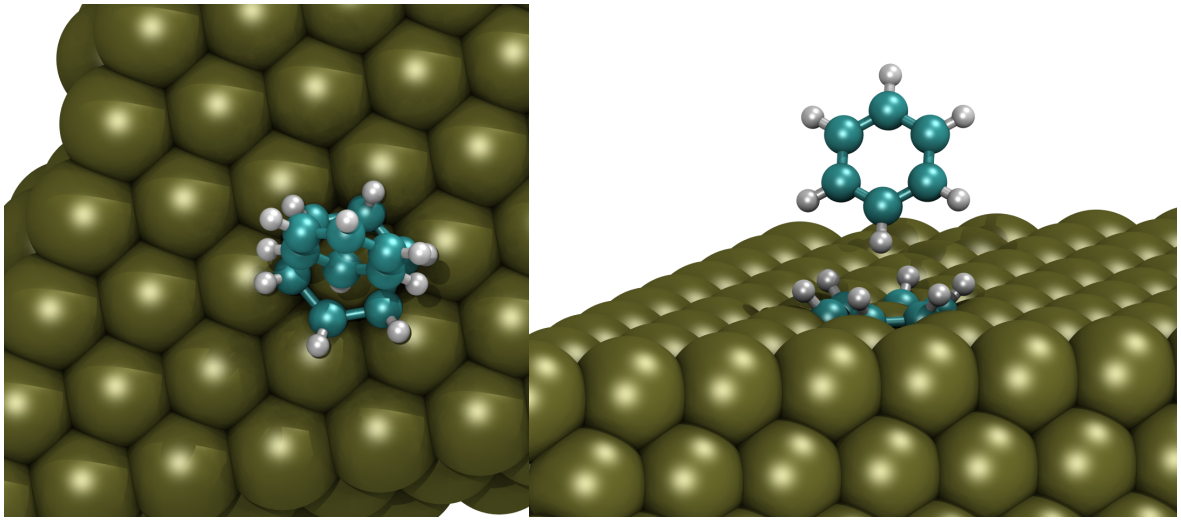

Figure 4.6: T-shaped benzene dimer adsorbed on Pt(111) surface as found by global optimization with OGOLEM and ReaxFF.

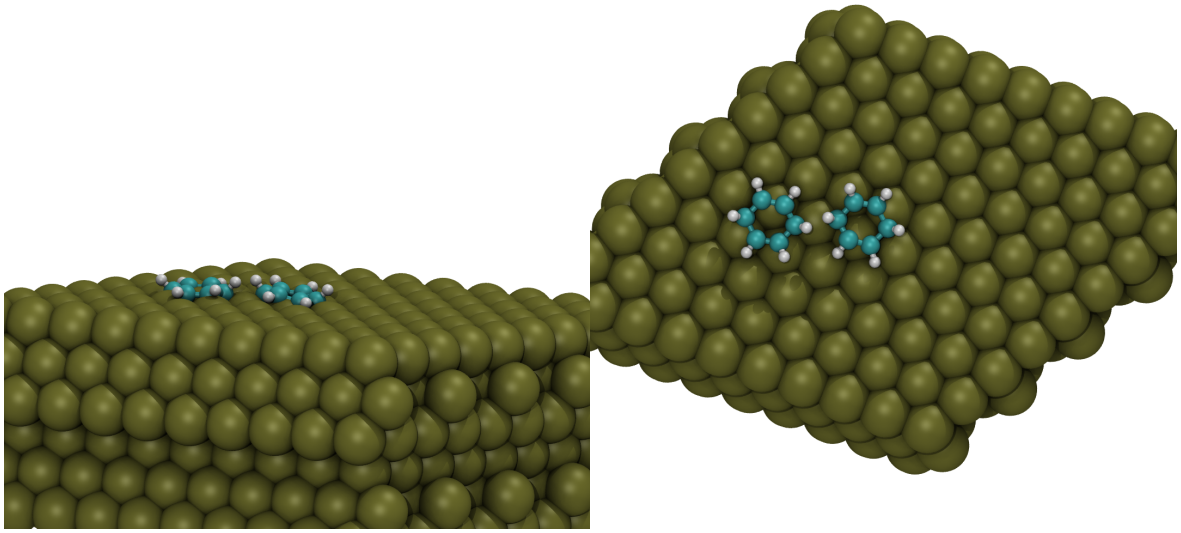

Figure 4.7: Benzene dimer obtained from a longer OGOLEM run compared to the T-shaped and parallel displaced structures with ReaxFF.

Lastly, for benzene, there has also been an attempt to use the OPLS-aa force field, which is described next. In case of gold, the molecule-surface interactions for benzene and TATA can be described as a vdW-term, as shown by *Freibert et al.* [10]. The same approach of adjusting the vdW-parameter for the metal has been applied to platinum, such that the distance between the metal surface and the benzene molecule closely matched the distance calculated by *Liu et al.* [84]. However, since the binding of benzene on a Pt(111) surface is much stronger than on gold, this approach does not work in this case. In doing so one gets the incorrect top30° adsorption position as the global optimum, with a vertical distance between the surface and the molecule of 2.24 Å. This distance is very close to the value reported by DFT calculations [83] of ~2.08 Å, which is expected since this was the reference when setting up the van der Waals parameter. Figure 4.8 shows a globally optimized adsorption geometry for four benzene rings. Here all the molecules are completely flat with respect to the surface, whereas DFT predicts the C-H bonds to be angled upwards with the hydrogen atoms further away from the surface. The angle of the hydrogen atoms ranges from ~5°-21° In short, this approach works well for weakly bound molecule-surface interactions, but fails to correctly describe more strongly bound molecule-surface interactions as exhibited by e.g. platinum. The xtb GFN-FF method is the newest member of the GFN family [60]. Its main advantage regarding this thesis is that it does work for all the surface slabs introduced into this, while the semiempirical GFN methods failed to converge the SCC cycle for transition metals. The adsorption of the benzene molecule, however, delivers the incorrect top30° adsorption position as well (Fig. 4.9). The vertical distance of the benzene ring from the surface is ~1.5 Å. However, GFN-FF still has advantages over more conventional force fields like OPLS-aa, since it does not require bond information as input. This information is being generated by the program itself after reading xyz-coordinates as input structure. This means that no atom types are needed. Furthermore, GFN-FF is parametrized for the bulk of the periodic table, spanning from hydrogen up to radon. In a global optimization run this allows for different bonding configurations per local optimization step.

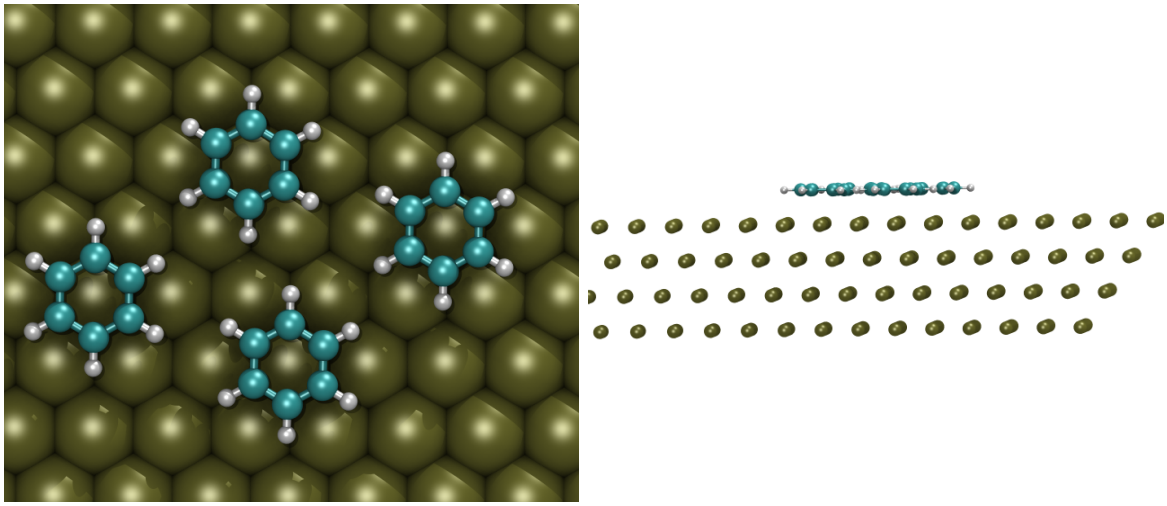

Figure 4.8: Top view and side view of four benzene molecules globally optimized on top of a Pt(111) surface using the Tinker backend.

The benzene dimer on a Pt(111) optimized with GFN-FF has both benzene rings adsorbed in top position next to each other (Fig. 4.10). Both rings are slightly angled downwards towards the direction where they are closest to each other. The approximate vertical distance of the benzene rings from the surface is 1.5 Å. In short, it has been shown for the case of benzene that of the tested methods only ReaxFF was able to correctly reproduce the adsorption position. In table 4.2 the distances between the benzene ring and the platinum surface are aggregated for the different methods. This table shows that – even though the molecule is overall closer to the surface – the relative distance between the carbon and hydrogen atoms with respect to the surface is only reproduced correctly by ReaxFF, while there is almost no difference for OPLS-aa and for GFN-FF the hydrogen atoms are closer to the surface than the carbon atoms.

Table 4.2: Benzene-surface distances for the applied methods.

	DFT [83]	ReaxFF	OPLS-aa	GFN-FF
C-surface / Å	2.08	1.59	2.08	1.50
H-surface / Å	2.51	2.01	2.06	1.11
Δ-CH / Å	0.43	0.42	-0.02	-0.39
adsorption position	bri30°	bri30°	top30°	top30°

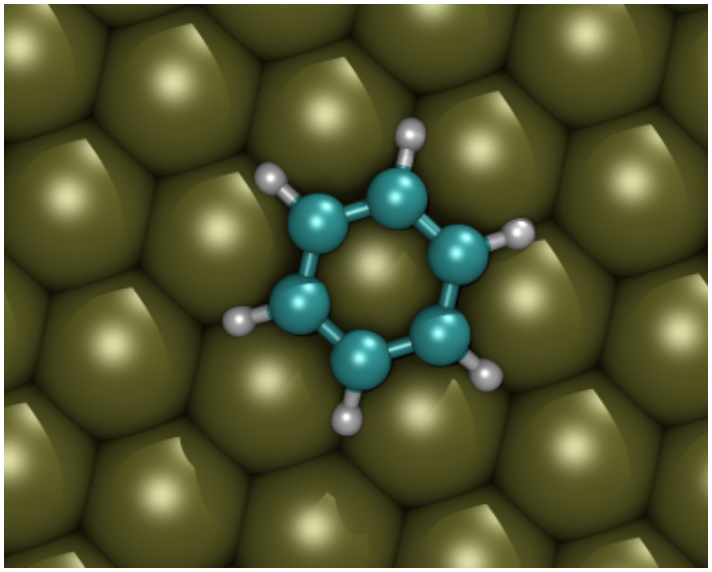

Figure 4.9: Globally optimized adsorption position of a single benzene molecule on Pt(111) resulting from optimization with the GFN-FF backend.

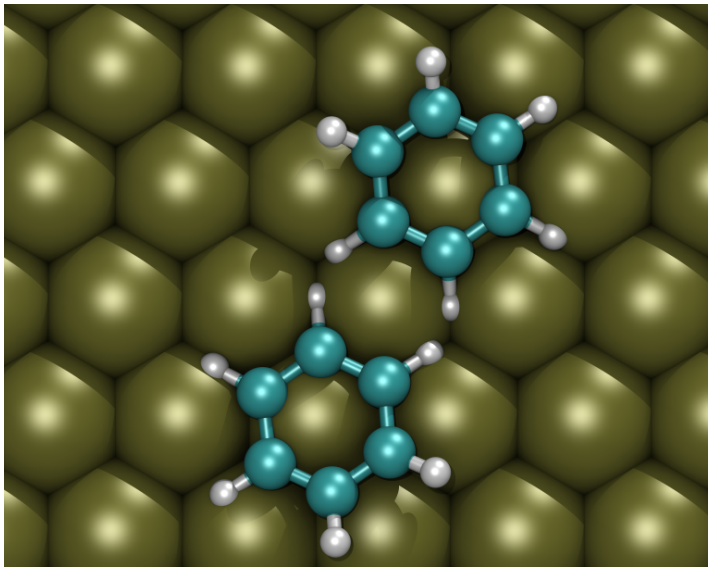

Figure 4.10: Globally optimized adsorption position of the benzene dimer on Pt(111) found by global optimization with the GFN-FF backend.

4.4 Acetophenone

Acetophenone has also been investigated by *Niklas Crome* during his Bachelor's thesis with similar issues as before. During longer optimization runs only one molecule would be adsorbed to the surface. The geometry of these adsorbed molecules was then investigated by *Crome*. Results for the dimer in the gas phase are shown in Fig. 4.11. This dimer has the two phenyl rings parallel to each other, slightly parallel displaced. The carbonyl group of each molecule is very close to the methyl group of the other acetophenone molecule. The same dimer optimized with MP2/cc-pVTZ shows similar interactions (Fig. 4.12). Here the phenyl rings are also parallel to each other, slightly parallel displaced. The distance from the carbonyl oxygen atom to the closest hydrogen atom of the methyl group is slightly longer than in the ReaxFF data, but the difference is only 0.02 Å. Therefore the gas phase structures from ReaxFF are in very good agreement with the *ab initio* data. To support this point further Fig. 4.13 shows both the ReaxFF and the MP2 result overlaid in one picture.

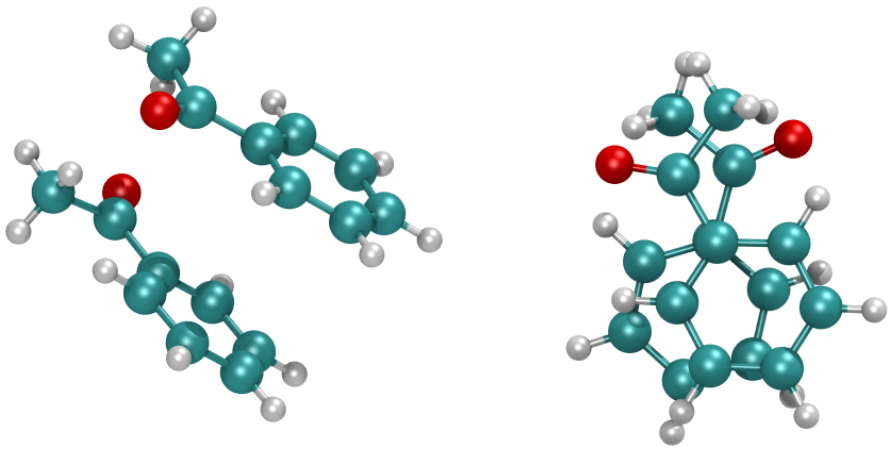

Figure 4.11: Two views of the acetophenone dimer optimized with ReaxFF.

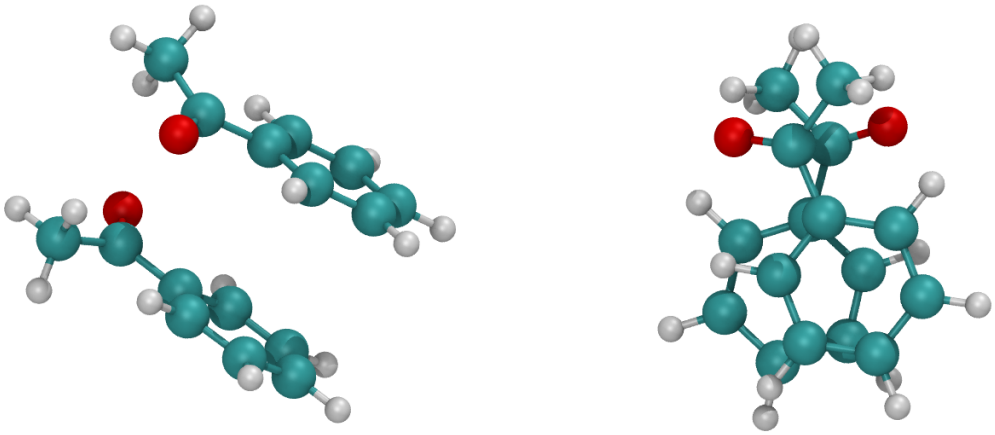

Figure 4.12: Two views of the acetophenone dimer optimized with MP2/cc-pVTZ.

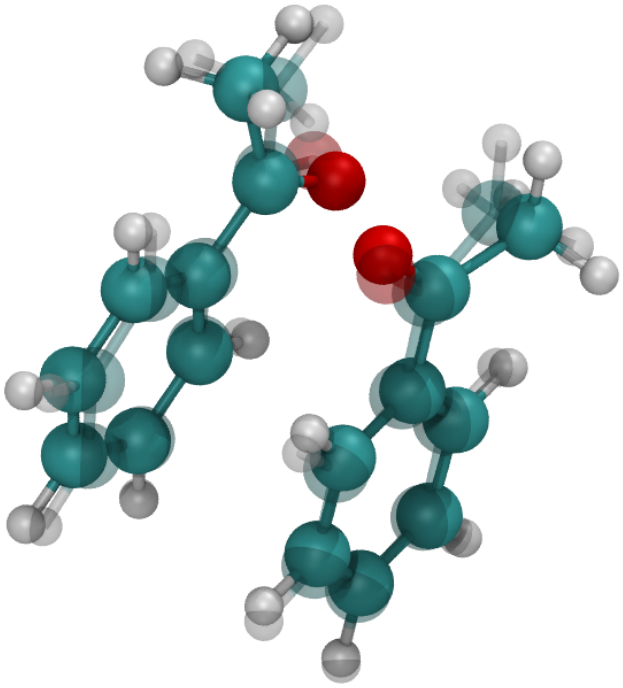

Figure 4.13: Overlay of the MP2 and ReaxFF results for the acetophenone dimer. RMSD: 0.319 Å.

In his global optimizations of acetophenone on a Pt(111) surface *Crome* decided to leave out the Pt-Pt interactions, since the platinum atoms are not allowed to move in these optimizations and their contribution would always be the same anyway. This did result in a noticeable decrease in computational cost. However, due to the above described mistake in the setup, most of the molecules did not adsorb to the surface. This can be seen in Fig. 4.14. DFT calculations of acetophenone on Pt(111) clusters have been carried out by *Vargas et al.* [88] on 2-layered Pt clusters with 19 and 31 atoms, respectively. Considering the prior discussion of the necessity of diffuse basis functions for the correct adsorption of benzene on Pt(111), larger basis sets than the ones used in Ref. 88 (DZ and DZP) would be a better reference. However, due to the lack of other references, this will be used for comparison. The DFT reference compares three adsorption types: adsorption through the carbonyl, hollow site adsorption and bridge adsorption. The carbonyl adsorption is favored over the others. In Ref. 88 it is noted that "[T]he distance from the platinum atoms is larger for [acetophenone] than for benzene" and the interaction between the phenyl ring and the surface is weaker. The globally optimized structure of the acetophenone monomer on a Pt(111) surface is shown in Fig. 4.15. In the monomer optimized with ReaxFF the carbonyl oxygen is

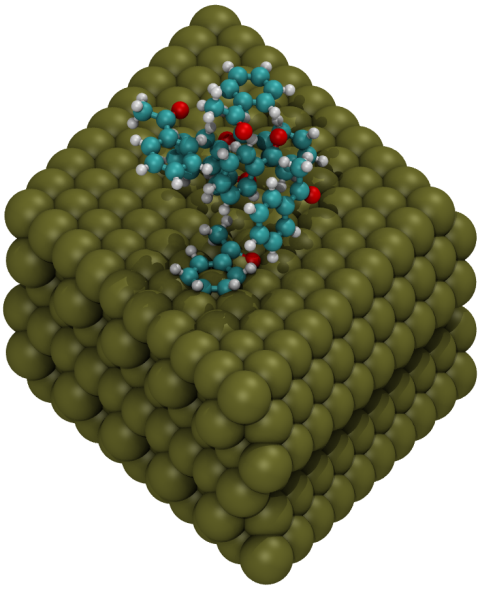

Figure 4.14: A view of the best result obtained for seven acetophenone molecules on the Pt(111) surface by *Crome* using OGOLEM and ReaxFF.

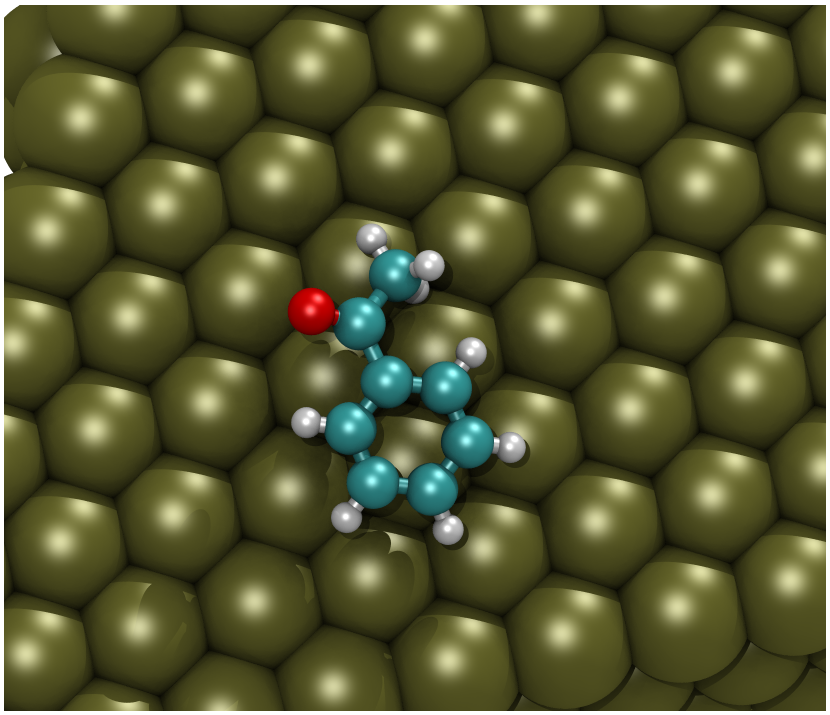

Figure 4.15: Globally optimized acetophenone monomer using OGOLEM and ReaxFF.

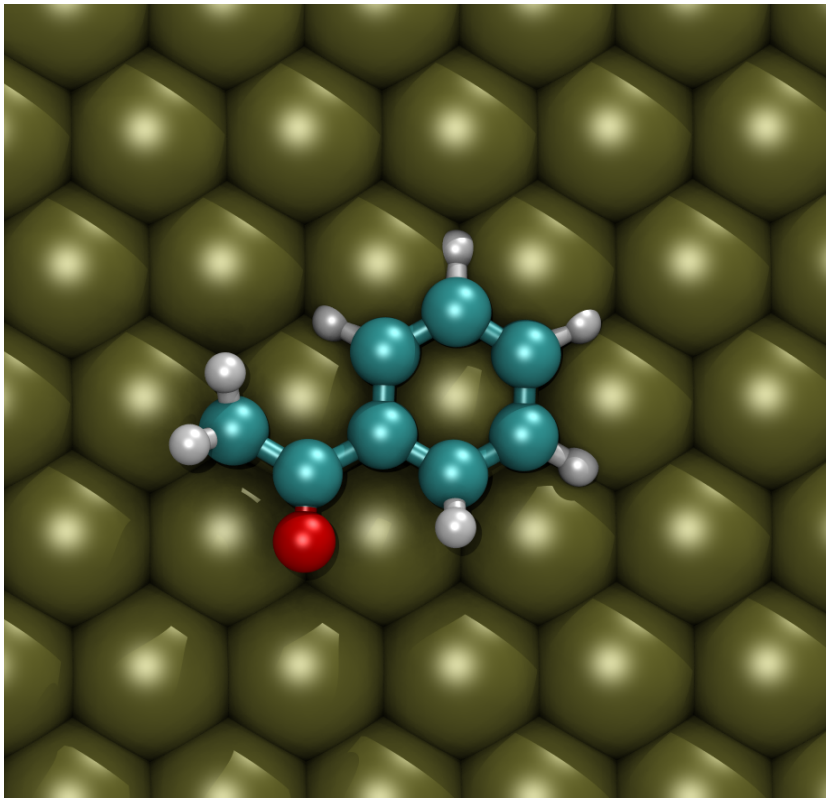

Figure 4.16: Globally optimized acetophenone monomer using OGOLEM and GFN-FF.

slightly pointing away from the surface, the phenyl ring is slightly displaced between a top and a bridge adsorption position. The structure, however, is still fairly similar to the adsorption geometries desribed in Ref. 88 and could yield a better structure after local optimization at the DFT level. Fig. 4.16 shows the resulting monomer from optimization with GFN-FF. Here the phenyl ring is in top position and slightly angled up towards the ketone while the carbonyl oxygen is also pointing away from the surface. Similarly to the ReaxFF result, this could still yield a better structure after local optimization at the DFT level.
Fig. 4.17 shows the globally optimized dimer. Here the phenyl rings are both adsorbed in top position and the carbonyl oxygen atoms are pointing towards the surface. However, experiments have shown that acetophenone dimers on a Pt(111) surface interact through their functional groups [89, 90], while the GFN-FF dimer shows the functional groups as far apart as possible. The trimer exhibits similar features as the dimer (Fig. 4.18). Interestingly, here the upwards bend of the hydrogen bonds very well visible, which had previously been described wrongly for benzene. However, regarding the positioning of the functional groups, this can not be overcome by local (post-)optimization at the DFT level.

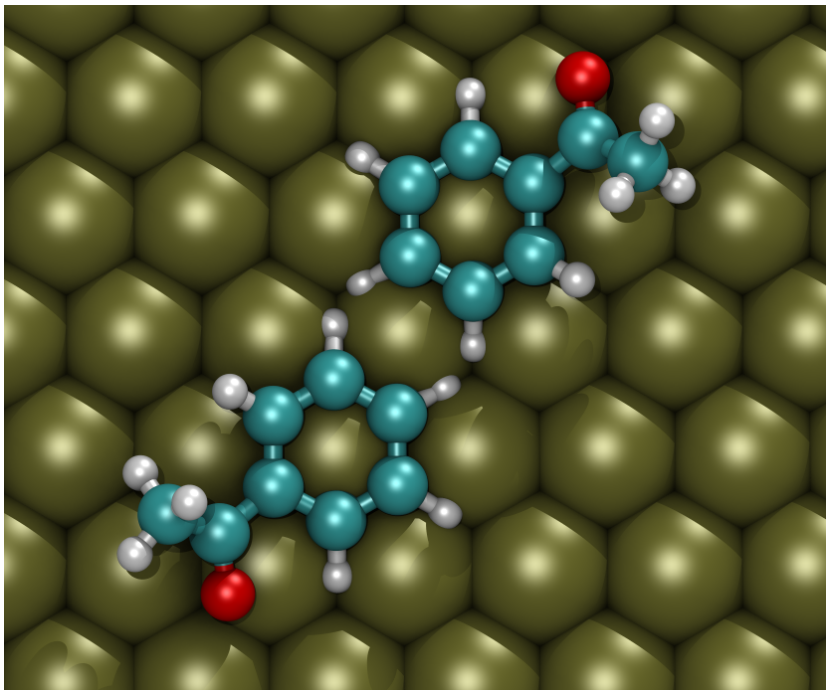

Figure 4.17: Globally optimized acetophenone monomer using OGOLEM and GFN-FF.

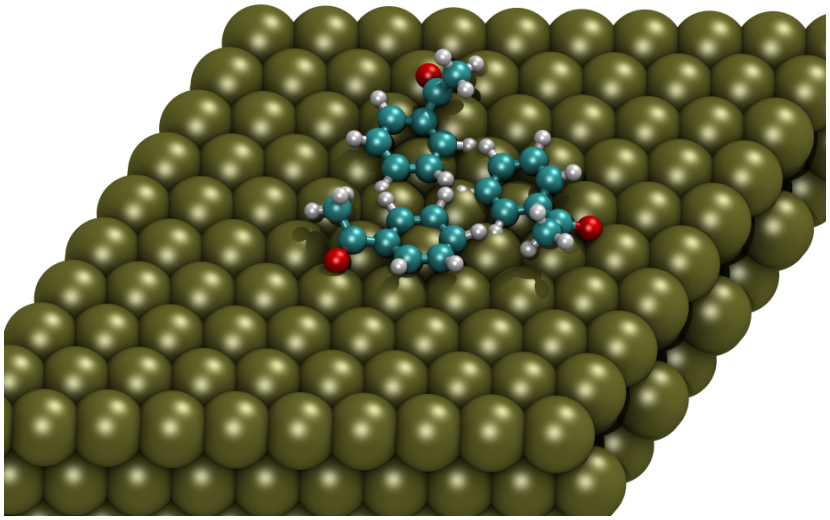

Figure 4.18: Globally optimized acetophenone trimer using OGOLEM and GFN-FF.

4.5 Ethyl Pyruvate

In the case of ethyl pyruvate most global optimization work has been done using GFN-FF, but in addition there have also been local optimizations at the DFT level using Quantum Espresso [91, 92]. But first, two isomers of ethyl pyruvate need to be differentiated (Fig. 4.19).

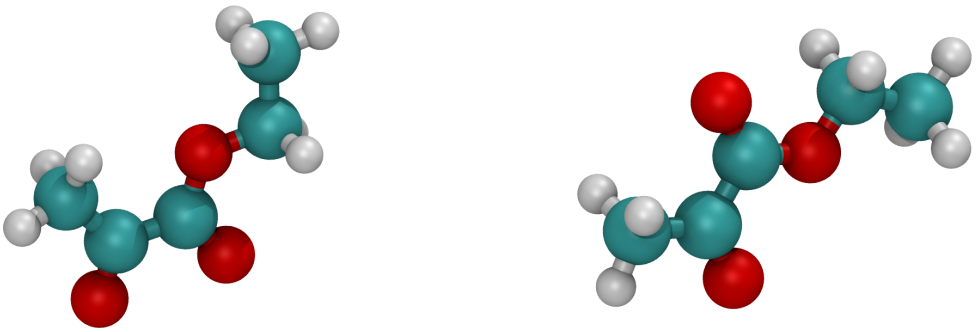

cis trans

Figure 4.19: The two isomers of ethyl pyruvate, cis- and trans- are named with respect to the OCCO-dihedral angle between the two keto oxygen atoms.

While the trans-isomer is more stable in the gas phase [93], the following results will show that the cis-isomer is preferred on the surface, due to the interaction of the carbonyl oxygen atoms with the platinum atoms. This is in agreement with the experiments and calculations by *Bürgi et al.* [94]. Fig. 4.20 shows the best found monomer from global optimization with the GFN-FF backend. This ethyl pyruvate molecule is adsorbed to the surface primarily through its carbonyl oxygen atoms, which each are positioned on a hollow site. The molecule itself is angled at approximately 35° with respect to the surface. The geometry obtained from DFT plane wave calculations is shown in Fig. 4.21. The DFT result shows the oxygen atoms each positioned on top of a platinum atom. The angle at which the molecule is inclined at approximately

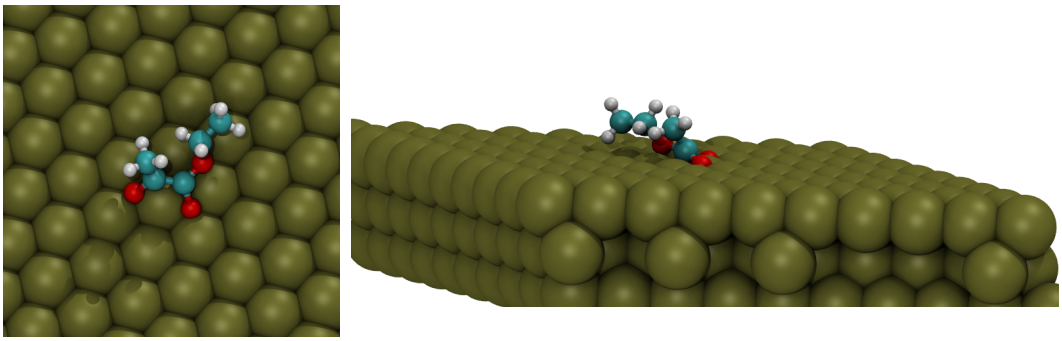

Figure 4.20: The best adsorption geometry for ethyl pyruvate on Pt(111) found by Ogolem and GFN-FF.

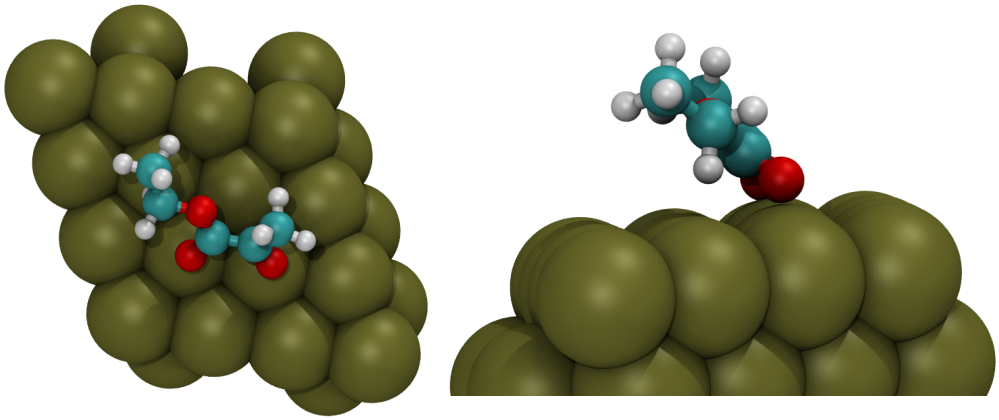

Figure 4.21: The optimized adsorption geometry for cis-ethyl pyruvate on a Pt(111) surface optimized with Quantum Espresso.

45°. While the position of the oxygen atoms shows a qualitative difference between the results from the two methods, the overall geometry of the molecule appears to be reproduced rather well. It should be noted that the GFN-FF monomer is the result of a global optimization with OGOLEM, where over six million local optimizations were performed, from a mix of random starting structures (in the initial global optimization stage) and "automated intelligent-guess" starting structures (in the later global optimization stages). Meanwhile, the DFT results are the outcome of two local optimizations, where the starting structures have been generated by manually placing ethyl pyruvate molecules on a surface slab. Therefore, the DFT result may or may not be the global minimum, which is impossible to tell without better knowledge of the search space, whereas the GFN-FF result is fairly likely the global minimum for this method, based on the extent of the global optimization search that has been performed.
Based on this, experimentally observed oligomers of different sizes have been investigated through global optimization. Fig. 4.22 shows the four best dimers found. While the best dimer structure shows the two molecules far apart, without any interaction of the functional groups, the other three structures show some interaction between -CH_3 groups and the carbonyl oxygen atoms. For the best dimer the ethyl groups of both molecules are the parts of the molecules that are closest to each other. For the second best dimer the ethyl group of one molecule is very close to the ester carbonyl group of the other molecule, which could be considered as a hydrogen bond. The third best dimer shows the same interaction of the functional groups, while the molecules are close to parallel to each other. The fourth best dimer does not show any hydrogen bond interactions, only the two ethyl groups are close to each other.

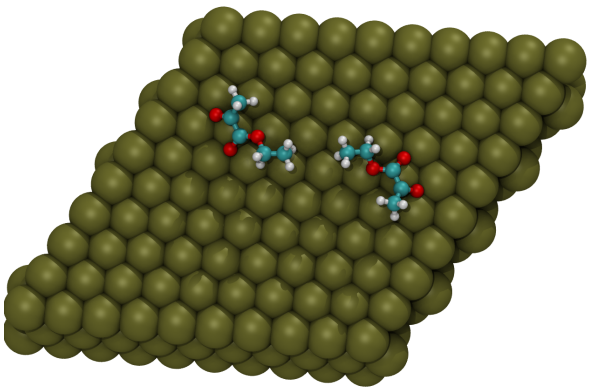

a) Rank0

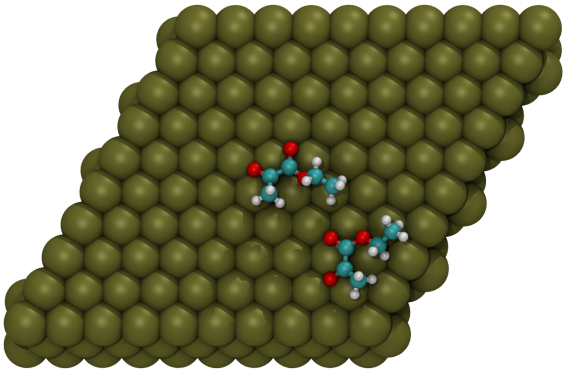

b) Rank1

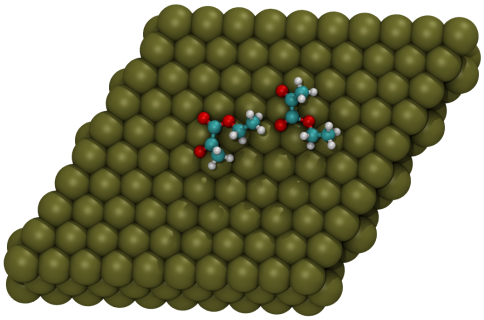

c) Rank2

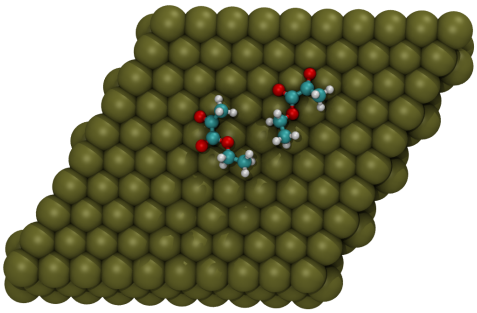

d) Rank3

Figure 4.22: The four best ethyl pyruvate dimers found by global optimization with the GFN-FF backend in descending order.

While all of the results shown so far have the molecule in the cis-configuration (which has also been the supplied seeding structure), other individuals from the global optimization show the trans-configuration as well. This shows that the global optimization scheme allows for a lot of internal flexibility of the molecules, not constraining the solutions to only the cis-configuration. Additionally, when more molecules are being optimized there are many clusters of mixed variety, even though the seeding structure for the molecule has always been the same. Subsequently, trimers and tetramers have also been globally optimized, which led to the structures given in Figs. 4.23 and 4.24. The trimers already display mixed cis- and trans-isomers, for example in Fig. 4.23b the bottom-most molecule in the image is a trans-isomer. In the best individuals found the ethyl groups are always pointing towards each other, mostly forming the shape of a three-pointed star. Only the second best cluster (b) shows a more compact structure. While the dimers and trimers have displayed some sort of ordering, the tetramers do not form any well-ordered structures. At this point it might be easier to consider the best tetramer as two dimers: one dimer is formed by the two molecules top-left, and the second dimer is formed by the two bottom-right molecules. Similarly the second tetramer (Fig. 4.24b could be seen as a trimer formed by the top three molecules and a solo molecule at the bottom. Since the ethyl pyruvate molecules generally adsorb in the same adsorption geometry as the monomer, and the monomer is really similar it can be argued that the STM image of those molecules would also look like the one of the monomer (see Chapter 5). A statistical analysis of the oligomers can therefore be made in order to compare the theoretical results with the STM images of the oligomers as well. Table 4.3 shows the dimer minima, ordered by their total energy and the distance between the centers of mass of the molecules and the angle between their molecule axes. The molecule axes are defined by the central C-C bond since this aligns well with the electron density in the STM image. Fig. 4.25 illustrates the distance between the centers of mass (dashed line) and the angle between the molecule axes (solid lines, θ).

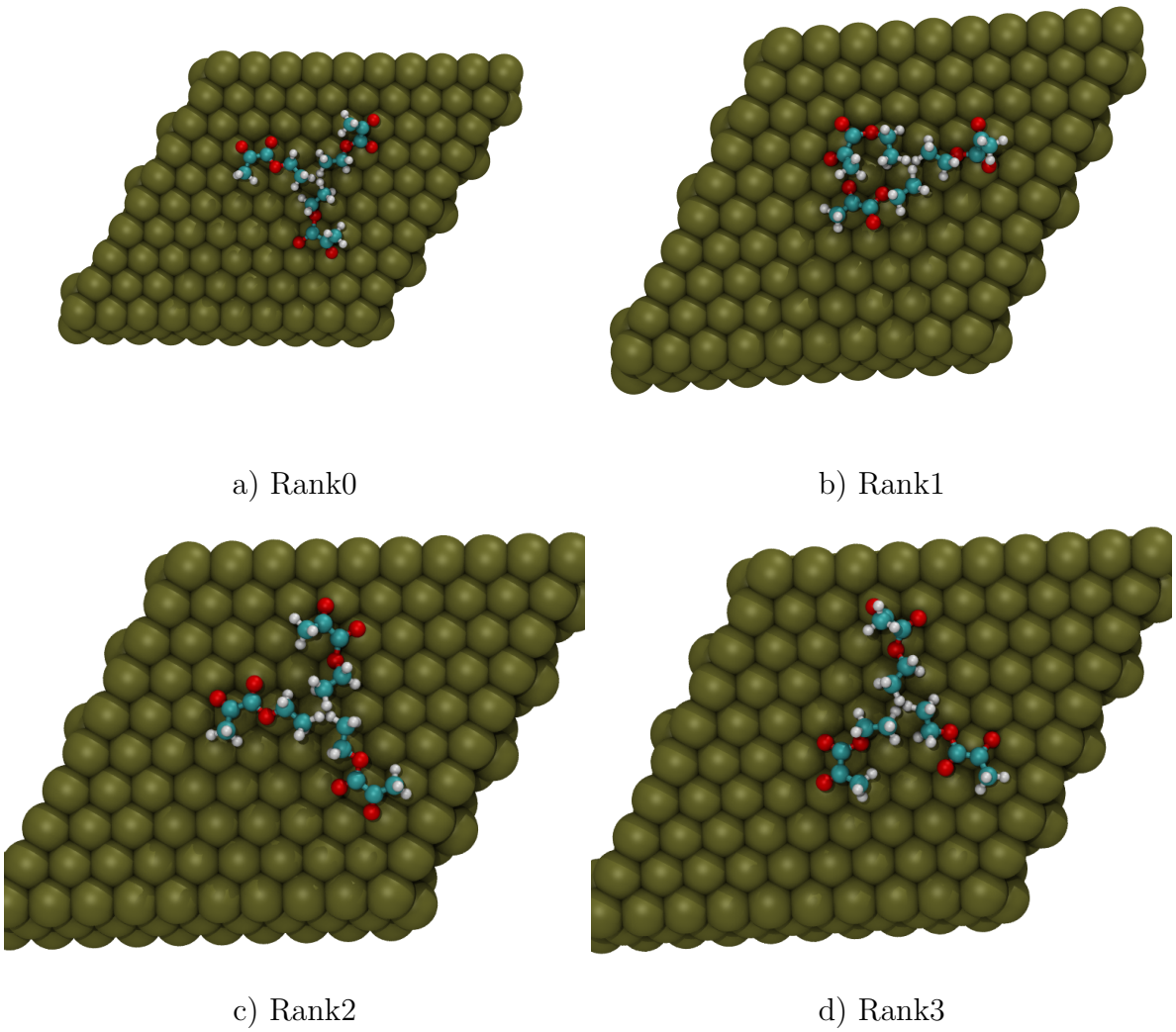

a) Rank0 b) Rank1

c) Rank2 d) Rank3

Figure 4.23: The four best trimers found by global optimization with OGOLEM and GFN-FF from best (a) to worst (d).

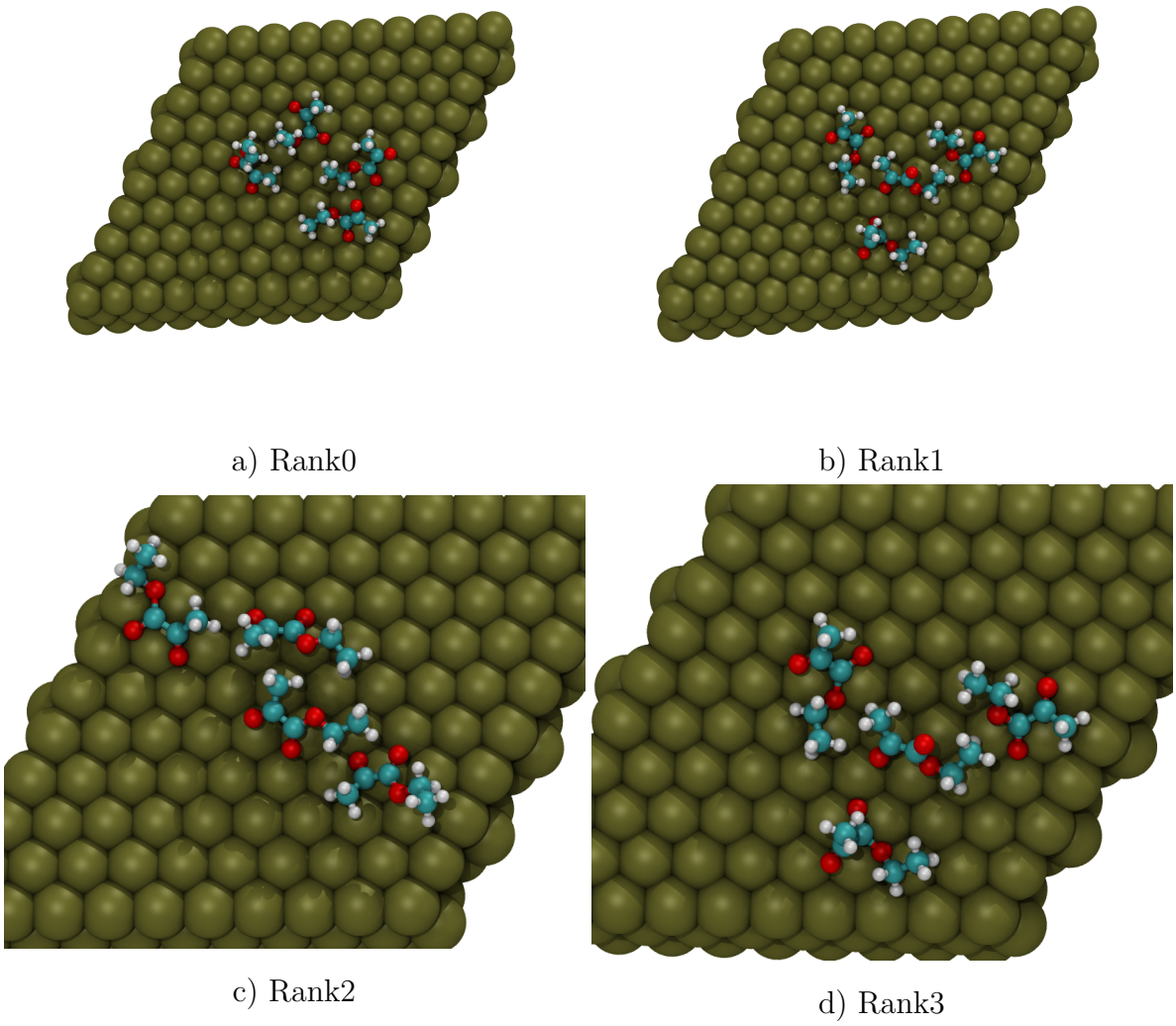

a) Rank0 b) Rank1

c) Rank2 d) Rank3

Figure 4.24: The four best tetramers found by global optimization with OGOLEM and GFN-FF from best (a) to worst (d).

The distance between the centers of mass can be used to determine whether the molecules are actually close enough to each other to interact, while the angle delivers information about the orientation of the molecules with respect to each other. Of these first twenty minima, the ones that have not been categorized (NA) all are more than 8 Å apart, which has been chosen as a cutoff distance. The full table can be found in the Appendix. To illustrate how well these minimum structures relate to the STM images, a few examples for the different dimers are shown in Fig. 4.26[2]. The three dimer structures from global optimization are ranked among the best that have been found. In table 4.3 they are the second to fourth best ranked structures. The labels under each image (D1-D3) are descriptors for the STM oligomers in chapter 5, Rank1-3 is a reference to the ranking of the minima, which is also found in Fig. 4.22.

[2]I would like to thank Marvin C. Schmidt for providing the STM images.

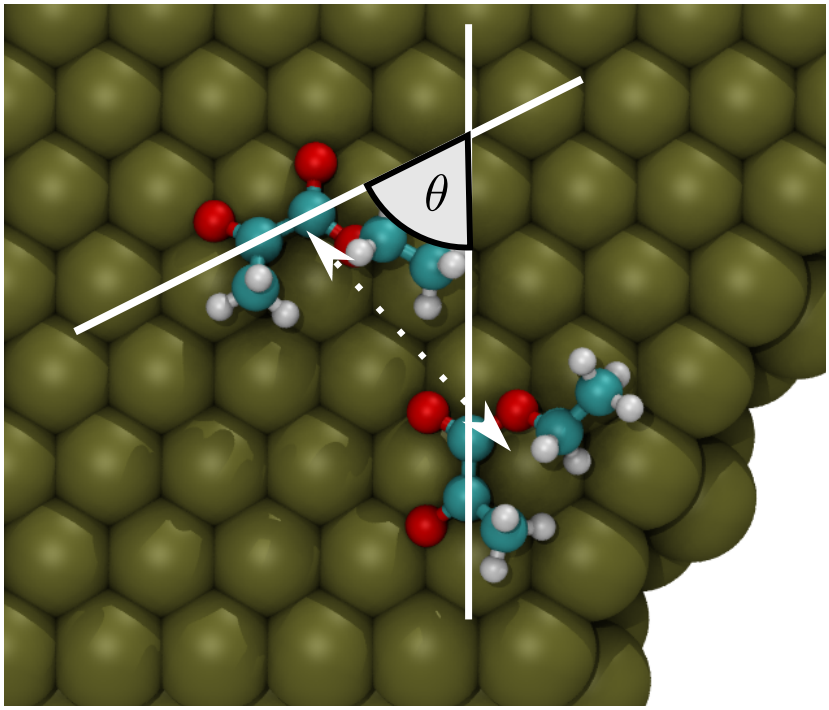

Figure 4.25: Illustration of the distance (dashed line) and angle (solid lines) between molecules.

Table 4.3: Center-of-mass distances and molecule axis angles for the 20 lowest lying minima and the dimer type based on the distances and angles.

Filename	Energy kJ/mol	dist / Å	Angle / °	STM Geo
ep.pt111.2/rank0individual98921.xyz	-33007.5007	10.94	176.76	NA
ep.pt111.6/rank0individual35570.xyz	-32954.2032	7.59	59.22	Butterfly
ep.pt111.8/rank0individual9660.xyz	-32874.9889	7.24	167.19	Alternating
ep.pt111.2/rank1individual88615.xyz	-32804.5395	7.53	113.04	Allenkey
ep.pt111.4/rank0individual12786.xyz	-32786.4786	8.59	111.61	NA
ep.pt111.3/rank0individual89583.xyz	-32785.8648	9.78	130.59	NA
ep.pt111.2/rank2individual92746.xyz	-32758.6161	9.91	20.69	NA
ep.pt111.4/rank1individual81322.xyz	-32701.8859	6.10	123.62	Allenkey
ep.pt111.8/rank1individual20698.xyz	-32700.3902	7.57	147.28	Allenkey
ep.pt111.2/rank3individual40770.xyz	-32697.5358	7.92	147.92	Allenkey
ep.pt111.8/rank2individual40024.xyz	-32692.5944	6.15	60.15	Butterfly
ep.pt111.3/rank1individual86470.xyz	-32678.4915	6.80	146.55	Allenkey
ep.pt111.8/rank3individual94993.xyz	-32676.926	8.22	154.54	NA
ep.pt111.4/rank2individual44303.xyz	-32673.5994	6.07	126.62	Allenkey
ep.pt111.8/rank4individual27954.xyz	-32670.8629	5.82	77.49	Butterfly
ep.pt111.4/rank3individual18113.xyz	-32670.1312	6.04	75.45	Butterfly
ep.pt111.4/rank4individual26416.xyz	-32666.1334	6.64	83.47	Allenkey
ep.pt111.9/rank0individual3309.xyz	-32661.9405	5.62	127.78	Allenkey
ep.pt111.4/rank5individual27560.xyz	-32660.4456	5.84	64.14	Butterfly
ep.pt111.9/rank1individual4173.xyz	-32651.8185	9.88	111.63	NA

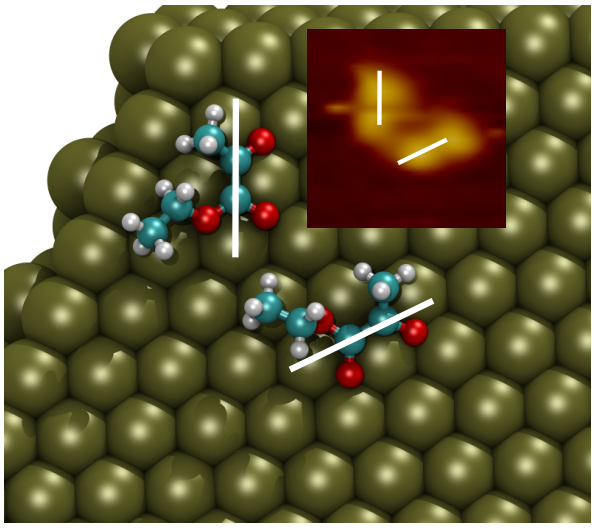

D3, Rank1

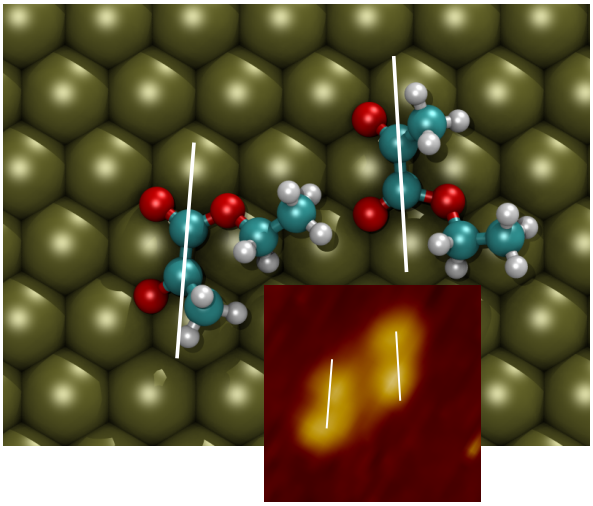

D2, Rank2

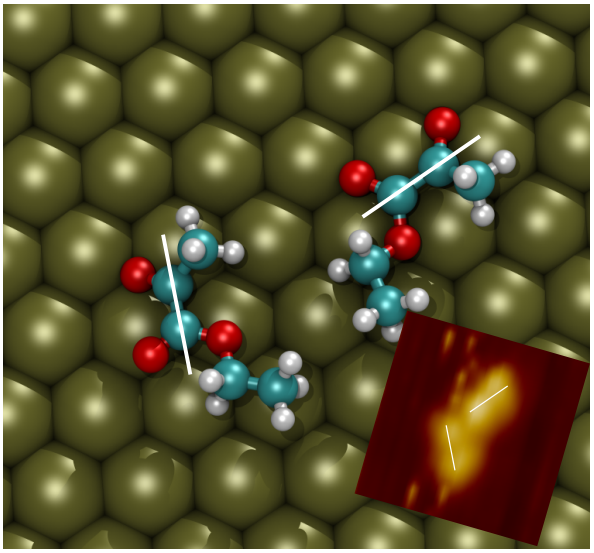

D1, Rank3

Figure 4.26: Comparison of three different dimer species from STM and global optimization.

5 | Publication: Tuning the strength of molecular bond in oxygenates via surface-assisted intermolecular interactions: atomistic insights

5.1 Scope of the project

The scope of the project was to improve the understanding of the surface adsorption of ethyl pyruvate on a Pt(111) surface. The computational contribution of the present author is the DFT calculation of the adsorbed geometry of ethyl pyruvate with Quantum Espresso [91, 92] and the STM images thereof.

5.2 Publication Data and Reprint

Reference: C. Schröder, M. C. Schmidt, C. Witt, S. Attia, J. Weber, A.-K. Baumann, B. Hartke, S. Schauermann, submitted to J. Phys. Chem. C in October 2020

Submitted: 26.10.2020

Accepted: 07.12.2020

Contribution: Calculations of surface adsorbed molecules and STM images. Text about the computational setup.

Graphic: -

Supporting Information: see Appendix A.1

THE JOURNAL OF PHYSICAL CHEMISTRY C

pubs.acs.org/JPCC Article

Tuning the Strength of Molecular Bonds in Oxygenates via Surface-Assisted Intermolecular Interactions: Atomistic Insights

Carsten Schröder, Marvin C. Schmidt, Christopher Witt, Smadar Attia, Jann Weber, Ann-Katrin Baumann, Bernd Hartke, and Swetlana Schauermann*

Cite This: J. Phys. Chem. C 2020, 124, 28159−28168 Read Online

ACCESS | Metrics & More | Article Recommendations | Supporting Information

ABSTRACT: Lateral interactions between coadsorbed hydrocarbon species play an important role in their chemical transformations on catalytic metal surfaces. In this report, we present a mechanistic study on mutual lateral interactions of the α-ketoester ethyl pyruvate adsorbed on a well-defined Pt(111) surface, resulting in a strong weakening of ester bonds. By employing a combination of surface-sensitive spectroscopic and microscopic techniques as well as theoretical calculations, we address the atomistic-level structure of surface assemblies containing several ethyl pyruvate species. We report formation of different types of surface oligomers comprising topologically different dimer, trimer, and tetramer species. Based on a combination of spectroscopic and microscopic observations, all species can be attributed to two large classes of oligomers exhibiting different types of intermolecular bonding. In the first class of species, the intermolecular interaction is realized via H-bonding between two acetyl groups of ethyl pyruvate, that is, a carbonyl and a methyl group of the neighboring molecules, while in the second type of species the bonding interaction involves the ester-O of one molecule and the acetyl group of a neighboring adsorbate. For the latter type of species, a strong IR frequency shift of the ester C−O vibration was observed pointing to a significant weakening of the related ester bonds, which might exert a strong impact on the chemical transformations involving this group. We demonstrate that the particular type of intermolecular interaction in ethyl pyruvate assemblies can be effectively tuned by controlling the adsorption parameters, such as surface coverage and the presence of coadsorbed hydrogen. Obtained results provide important insights into the details of lateral interactions of complex multifunctional molecules adsorbed on catalytically relevant surfaces. We show that the parameter space in a catalytic process involving ester compounds can be purposefully varied to tune the strength of the ester bond toward improving the catalytic performance.

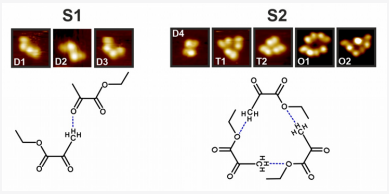

INTRODUCTION

Lateral interactions between molecular species adsorbed on a metal surface might play a crucial role in controlling activity and selectivity of heterogeneously catalyzed multipathway reactions. Particularly for reactions involving hydrocarbons, the selectivity often depends on subtle differences in the activation barriers of individual reaction routes,[1] which are determined not only by the bonding of the reactants to the underlying catalyst but also by their intermolecular interactions with the surrounding adsorbates. The latter type of interactions can greatly modify the overall energy landscape and by this strongly alter the selectivity toward the desired reaction. There are two types of new emerging fields in heterogeneous catalysis based on this phenomenon—enantioselective[2,3] and ligand-assisted[4,5] heterogeneous catalysis—that strongly rely on intermolecular interactions between coadsorbed reactants and the modifier molecules. The latter species are employed for surface functionalization rendering the catalyst highly active and selective toward the desired reaction path. Recently, an atomistic-level understanding of such complex functionalized catalysts was achieved in studies combining surface-sensitive spectroscopies and microscopy with the theoretical approach for a number of enantio- and chemoselective catalytic systems,[2,3,5−17] allowing to develop first rational ideas for optimizing lateral interactions in this type of reaction.

Despite this recent progress in the field, the deep fundamental-level understanding of adsorbate−adsorbate interactions is available only for a very limited number of reactive systems because of their vast complexity and numerous possibilities to build molecular complexes comprising two or more adsorbates. Experimental identification of adsorbed surface species and a microscopic-level understanding of the mutual lateral interactions between single adsorbates still remain a highly challenging task.

One of the most important reactive systems in the field of enantioselective heterogeneous catalysis involves α-ketoesters, which can be efficiently hydrogenated over chirally modified

Received: October 26, 2020
Revised: December 3, 2020
Published: December 15, 2020

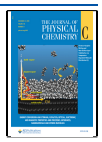

https://dx.doi.org/10.1021/acs.jpcc.0c09659
J. Phys. Chem. C 2020, 124, 28159−28168

surface to corresponding chiral lactates. Several groups reported atomistic-level studies on surface chemistry of the simplest α-ketoester methyl pyruvate (MP), over either pristine or chirally modified Pd(111)[18−20] and Pt(111)[21,22] metal surfaces. On pristine Pd(111), formation of enol species as a result of keto−enol tautomerization of the carbonyl group of MP was proposed.[18] The same enol form of MP was also suggested to be the active species in the 1:1 chiral docking complexes between MP and the chiral modifier (1-naphthyl)-ethylamine (NEA).[19] On Pt(111), formation of enediolate species was put forward,[22] in which both carbonyl groups directly interact with two underlying Pt atoms. These and some other studies[23] provided first valuable ideas about the interaction of α-ketoesters with transition metal surfaces. However, a number of important questions still remain unresolved. Specifically, there is no general agreement on the chemical nature of the adsorbed surface species and on the possibility of keto−enol tautomerization vs enediolate formation upon adsorption on transition metal surfaces. Also, the interaction of structurally more complex α-ketoesters and the details of their lateral interaction with coadsorbed molecular species remain largely unexplored.

To address the details of mutual lateral interactions in structurally more complex α-ketoesters, we performed a mechanistic study of ethyl pyruvate (EP) adsorbed on a well-defined Pt(111) surface, both pristine and H-containing. We employed a unique combination of experimental techniques[24] including molecular beams, infrared reflection−absorption spectroscopy (IRAS), and scanning tunneling microscopy (STM), capable of providing both spectroscopic information about the chemical nature of adsorbed surface species and microscopic information about their distribution in real space. Complementarily, theoretical modeling of the adsorption structure of EP monomer and modeling of the STM images were performed at the density functional theory (DFT) level to understand the details of lateral interactions between neighboring surface species. Specifically, we show that EP forms a large number of oligomers including different types of dimer, trimer, and tetramer species, the relative abundance of which strongly depends on the adsorption parameters such as surface coverage and the presence of hydrogen. Based on a combination of spectroscopic and microscopic observations, all species can be attributed to two large classes of oligomers exhibiting different types of intermolecular bonding. In the first class of species the intermolecular interaction involves two acetyl groups of neighboring EP species, while in the second type of species the bonding interaction is realized via H-bonding between the ester-O of one molecule and the acetyl group of a neighboring EP species. This latter type of interaction significantly weakens the ester bond as suggested by a strong frequency shift of the related C−O ester vibration, which might potentially exert a strong impact on the chemical transformations involving the ester group. The intermolecular interaction in ethyl pyruvate assemblies can be effectively tuned by changing the adsorption parameters, such as surface coverage and the presence of coadsorbed hydrogen, providing by this an experimentally accessible tool to affect the strength of the ester bond by changing the nature and the concentration of coadsorbed species. Additionally, by performing spectroscopic investigation with isotopically labeled (^{13}C)EP, we addressed the previously proposed adsorption models put forward for α-ketoester MP with transitions metal surfaces. The spectroscopic observations obtained in our study suggest that both previously discussed models suggesting enol or enediolate formation are not valid for a structurally more complex α-ketoester EP.

The obtained results provide important benchmarks for theoretical modeling of mutual lateral interactions in complex molecular assemblies formed on transition metal surfaces. Currently, theoretical modeling of mutual lateral interaction in large assemblies of ethyl pyruvate is being performed by global structure optimization employing a combination of semi-empirical and force-field approaches.

METHODS

All experiments were performed in two independent ultrahigh-vacuum (UHV) apparatuses—UHV-IRAS/molecular beam and UHV-STM apparatus—each equipped with a dedicated preparation chamber. After the preparation the samples were transferred *in situ* in the main part of each apparatus.

Sample Preparation. The Pt(111) single crystal (MaTeck GmbH) was cleaned prior to use in a dedicated preparation chamber (base pressure < 2×10^{-10} mbar) by repeated cycles of Ar^+ ion bombardment at room temperature, followed by annealing at 1200 K and subsequent oxidation in 1×10^{-7} mbar of O_2 at 650−750 K to remove residual carbon. The last step contains the rapid flash of the sample to 1000 K. Shortly before each experiment the sample was flashed to 600−800 K before cooling to the required temperature to remove CO adsorbates. The long-range order and cleanliness of the Pt(111) single-crystal were checked by low-energy electron diffraction (LEED), Auger electron spectroscopy (AES), and additionally IRAS of adsorbed CO to probe the abundance of adsorption sites.

Ethyl pyruvate (Sigma-Aldrich, purity >97%) and ^{13}C-ethyl pyruvate (Sigma-Aldrich, 99% ^{13}C, purity 98%) were purified prior to each experiment by repeated freeze−pump−thaw cycles.

IRAS/Molecular Beam Experiments. The IRAS/molecular beam experiments were performed in a specially designed UHV apparatus (base pressure > 2×10^{-10} mbar). The apparatus contains two effusive doubly differentially pumped multichannel array sources operated at room temperature. Further details on the apparatus can be found elsewhere.[25] Ethyl pyruvate and hydrogen were independently dosed via two molecular beams at typical fluxes of 7.2×10^{12} and 5×10^{14} molecules s^{-1} cm^{-2}, respectively.

IRAS data have been acquired by using a vacuum Fourier transform infrared (FT-IR) spectrometer (Bruker Vertex 80v) with a spectral resolution of 2 cm^{-1}, a mid-infrared (MIR) polarizer, and using p-polarized IR light. The spectrometer is equipped with a narrow-band mercury cadmium telluride (MCT) detector. All IRAS spectra were acquired at the same surface temperature that was used for ethyl pyruvate deposition (100 K). An automated quadrupole mass spectrometer (QMS) system (Hiden, HAL 301/3F) was employed for continuous monitoring of the partial pressures of gaseous species.

STM Experiments. The STM measurements were performed in an UHV (base pressure < 1×10^{-10} mbar) apparatus by employing a variable temperature (90−300 K) Aarhus 150 SPM (SPECS). All measurements were performed in a constant current mode, and the bias voltage UT was applied to the sample. The etched W-Tip was commercially produced by SPECS and *in situ* sharpened by repeated cycles of 1.25 keV Ar^+ bombardment with 5×10^{-6} mbar back-

https://dx.doi.org/10.1021/acs.jpcc.0c09659
J. Phys. Chem. C 2020, 124, 28159−28168

pressure for 5 min. The sharpness of the W-Tip was validated on the pristine Pt(111) surface. The quality of the sample was additionally verified by acquiring STM images prior to the deposition. EP was dosed through an individual gas doser onto the Pt(111) surface kept at the desired deposition temperature and then transferred to the STM chamber for measurements. For the hydrogen deposition, the measurement chamber was backfilled with hydrogen through an individual gas doser with 1×10^{-6} mbar during the STM experiment.

DFT Calculations. DFT calculations of the adsorption geometry of EP monomer adsorbed on Pt(111) were performed by using a Quantum ESPRESSO26-27 with the PBE28 functional and projector-augmented-wave pseudopotential Pt.pbe-n-kjpaw_psl.1.0.0.UPF from ref 29, and the analogue pseudopotentials for the other elements have been used. The kinetic energy cutoff for the wave functions was set to 50 Ry, and a $2 \times 2 \times 2$ k-point grid was used to sample the Brillouin zone. These values have been arrived at by sampling different values for a platinum slab until the energy was converged to within 10^{-4} Ry. To separate the images in the z-direction, a 90 Å vacuum was used. The energy convergence cutoff for the optimization itself was set to 10^{-6} Ry. For the STM calculation, the Tersoff–Hamann[30] approach was used. The sample bias was 120 meV, and the isovalue was set to 0.5×10^{-6}.

Vibrational frequencies of an isolated EP molecule were calculated within the harmonic approximation at the B3LYP level with the aug-cc-pvqz basis set and gd3 correction of single molecules in the gas phase using the Gaussian16 software.[31]

RESULTS AND DISCUSSION

Experimentally, interaction of EP with the Pt(111) surface was investigated by a combination of molecular beam techniques, IRAS and STM in two independent ultrahigh-vacuum apparatuses.[24] Figure 1 shows the IR spectrum theoretically calculated at the DFT level for the gas phase (spectrum 1) and experimentally measured spectra of EP adsorbed on Pt(111) at 100 K (spectra 2–5). The assignment of the vibrational bands

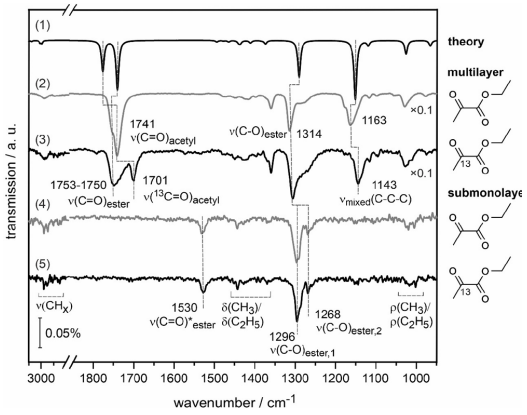

Figure 1. (1) Calculated gas phase spectrum of EP using DFT. IR spectra of EP adsorbed on Pt(111) at 100 K: (2, 3) EP and ^{13}C-EP multilayer (total exposure 2.9×10^{15} and 1.1×10^{15} molecules cm^{-2}); (4, 5) EP and ^{13}C-EP at submonolayer coverage (7.2×10^{13} molecules cm^{-2}).

was performed based on the comparison of the theoretical spectrum with the experimental spectra (2, regular EP) and spectra (3, ^{13}C-labeled EP) obtained for multilayer coverages. The spectra of EP multilayers, in which the absolute majority of the molecules is not in immediate contact with the underlying metal, serve as a reference for the nearly unperturbed molecular state of EP. In the isotopically labeled component, the carbon atom involved in the carbonyl group of the acetyl entity ($CH_3(\mathbf{C{=}O})-$) was labeled with ^{13}C (see Figure 1). In the further discussion, we will denote this carbonyl group as the acetyl–carbonyl group, while the carbonyl group involved into the ester entity ($-(\mathbf{C{=}O})C-O-C_2H_5$) of EP will be denoted as ester–carbonyl. Table S1 of the Supporting Information summarizes the experimentally observed and theoretically computed vibrational bands.

The most important vibrational bands in the multilayer spectrum comprise the C=O stretching vibration at 1741 cm^{-1} (1701 cm^{-1} for the ^{13}C-isotope) in the acetyl–carbonyl group ($\nu(C{=}O)_{acetyl}$),[20] the C=O stretching vibration at 1749–1753 cm^{-1} in ester–carbonyl ($\nu(C{=}O)_{ester}$),[20,25] and the mixed vibration at 1314 cm^{-1} including mostly the stretching mode of the C–O single bond ($-(C{=}O)\mathbf{C-O}-C_2H_5$) in the ester group ($\nu(C-O)_{ester}$).[20,26] Further visible vibrations are related to the deformation vibrations of the $-CH_2-$ and $-CH_3$ groups in the range 1360–1476 cm^{-1} ($\delta(CH_x)$), a mixed mode at 1162 cm^{-1} ($\nu_{mixed}(C-C-C)$) mostly involving the stretching vibration of all skeletal carbons, and the stretching vibration of the CH_x groups ($\nu(CH_x)$) lying around 3000 cm^{-1}. Upon isotopic labeling of the acetyl–carbonyl group by ^{13}C, the vibrational band ($\nu(C{=}O)_{acetyl}$) shifts from 1741 to 1701 cm^{-1}. The shift by 40 cm^{-1} is in an excellent agreement with the previously reported values of 30–40 cm^{-1} for simple carbonyl compounds, for example, acetophenone.[9,10] As expected, the other major vibrational bands related to the ester group ($\nu(C{=}O)_{ester}$ and $\nu(C-O)_{ester}$) do not experience any major shifts upon isotopic labeling of the acetyl–carbonyl group. The band at 1162 cm^{-1} assigned to the mixed mode vibration $\nu_{mixed}(C-C-C)$ shifts by 19 cm^{-1}. The displacement vectors related to this vibrational band $\nu_{mixed}(C-C-C)$ are shown in the Supporting Information (Figure S1), demonstrating that the labeled ^{13}C atom is strongly involved in this vibrational mode.

Adsorption of EP at submonolayer coverages was investigated at the same temperature both with regular and ^{13}C-labeled species. Spectra 4 and 5 in Figure 1 are related to the coverage close to saturation for the regular and ^{13}C-labeled EP, respectively. In this coverage range, the intensity distribution of the most important vibrational peaks drastically changes: while both bands at 1753 and 1741 cm^{-1} completely vanish, the band $\nu(C-O)_{ester}$ remains very pronounced and shifts from 1314 to 1296 cm^{-1}. Additionally, two new bands at 1268 and 1530 cm^{-1} evolve; their positions are not affected by isotopic labeling of the acetyl–carbonyl group.

Vanishing of the bands involving both carbonyl groups might be potentially related to two microscopic reasons: (i) the orientation of the C=O bonds can be nearly parallel to the underlying metal and the related vibrations becomes invisible because of the metal surface selection rule;[27] (ii) the C=O bond is considerably perturbed due to strong interaction with the underlying metal and/or coadsorbed species and the related vibrational band significantly shifts. The red-shift of the $\nu(C-O)_{ester}$ vibration (from the gas phase value 1314 cm^{-1} to 1296 cm^{-1}) lies in the range typical for adsorption of gaseous

https://dx.doi.org/10.1021/acs.jpcc.0c09659
J. Phys. Chem. C 2020, 124, 28159–28168

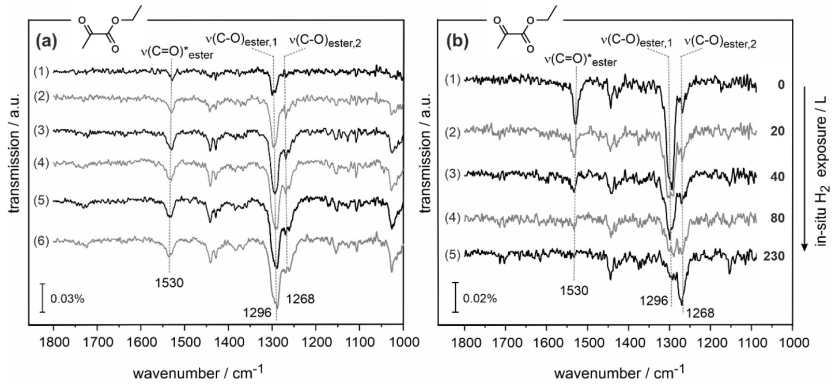

Figure 2. IRAS spectra of EP adsorbed on Pt(111) at 100 K. The spectra were obtained for (a) increasing EP exposure and (b) during *in situ* H_2 exposure at a constant coverage of EP (full details are given in the Supporting Information).

hydrocarbon species on metal surfaces[28−30] and can be explained by possible rehybridization of the related molecular orbitals upon interaction with the underlying metal as well as by the wall effect.[27] The band at 1268 cm^{-1} lies close to the band $\nu(C{-}O)_{ester}$ 1296 cm^{-1} and can be assigned to the same vibrational mode, which is red-shifted from the less perturbed state (1296 cm^{-1}) due to, for example, H-bonding. Previously, pronounced red-shifts due to H-bonding between an O atom and a H atom of two neighboring molecules were reported for a number of different hydrocarbon compounds,[31,32] for example, adsorbed acetophenone forming dimer species on Pt(111).[9,11] In the following, we will distinguish between two $\nu(C{-}O)_{ester}$ vibrational bands and will denote the band at 1296 cm^{-1} as $\nu(C{-}O)_{ester,1}$ and the band at 1268 cm^{-1} as $\nu(C{-}O)_{ester,2}$.

The band at 1530 cm^{-1} is present neither in the multilayer nor in the gas phase spectra of EP and therefore must arise from a strong interaction of the adsorbed EP species with Pt. Importantly, this vibrational band does not shift upon isotopic labeling of the acetyl−carbonyl group, indicating that the C atom of the acetyl−carbonyl is not involved into the appearance of this new band. The exact assignment of the band at 1530 cm^{-1} is rather ambiguous. In the previous studies on structurally more simple MP adsorbed on Pt(111) by McBreen et al., a band at a similar frequency (1543 cm^{-1}) was assigned to $\nu(C{-}O)$ or the mixed $\nu(C{-}O) + \nu(C{-}C)$ mode of an enediolate species,[22] in which both carbonyl groups establish two bonds to underlying two Pt atoms forming a structural fragment Pt···O···C···C···O···Pt. In the latter studies from the same group performed at higher temperatures (300 K), a band in a similar frequency range was observed at 1594 cm^{-1} on Pt(111), which was interpreted as a $\nu C{=}C$ mixed mode of enol species formed after keto−enol tautomerization of the acetyl groups of MP.[21] The group of Tysoe investigated MP adsorption on Pd(111), where formation of a weak band in the same frequency range (1558 cm^{-1}) was observed.[20] In this report, the band was assigned to a C=C bond formed in the enol or enolate form of MP, implying that keto−enol tautomerization of the acetyl group of MP must have occurred. The hypothesis of enol or enolate formation was supported by a study from the same group, combining STM and theoretical modeling of MP species adsorbed on Pd(111).[18] On the basis of the comparison of the experimentally measured STM line profiles across the adsorbates and theoretically modeled profiles for ketone and enol forms of MP, the authors concluded that only the enol form of the adsorbed species can explain the experimental observations.

It should be emphasized that both models recently proposed in the literature−formation of enol or enediolate species−are in strong disagreement with our experimental observations obtained by IR spectroscopy. If the band at 1530 cm^{-1} observed in our study would originate either from the C=C bond (as suggested by the enol model) or from enediolate species, it must shift upon ^{13}C isotopic labeling of acetyl−carbonyl since this ^{13}C atom would be directly involved in the corresponding C=C bond of the enol species or the Pt···O···C···C···O···Pt fragment of enediolate. No isotopic shift of the band at 1530 cm^{-1} was observed in our IR spectra, so it can be quite safely concluded that the labeled ^{13}C atom is not involved in the related vibration. The only remaining possibility to assign this band is the hypothesis that this vibration originates from the ester−carbonyl, which must be strongly shifted from its unperturbed value due to pronounced mixing of its molecular orbitals with the d-orbitals of underlying Pt atom(s). Such a scenario for interaction of carbonyl compounds with transition metals is in agreement with the adsorption model of acetone previously suggested by Ibach et al. Investigating acetone adsorption on Pt(111) by a combination of IRAS and off-specular high-resolution electron energy loss spectroscopy (HREELS), the authors observed formation of vibrational peaks in the range 1520−1585 cm^{-1} (IRAS) and 1550 cm^{-1} (HREELS), which were assigned to a side-on $\eta_2(CO)$ adsorption configuration of acetone,[33] in which the carbonyl group forms a fragment Pt···C···O···Pt, in either the π or di-σ configuration. This conclusion was additionally corroborated by the earlier studies on decomposition of isopropanol, producing the $\eta_2(CO)$ configuration in the same frequency range (1584 cm^{-1}).[34] The band at 1530 cm^{-1} observed in our study can be thus most likely related to the $\eta_2(CO)$ configuration, that is, to the fragment Pt···C···O···Pt formed for the ester−carbonyl group. In the studies by the Tysoe and McBreen groups, the bands in the frequency range 1540−1590 cm^{-1} were rather assigned to the C=C bond of enols, enolates, or enediolates. While this might be true for MP, in the case of EP adsorption on Pt(111) the assignment of the band at 1530 cm^{-1} to the C=C bond (formed in the

https://dx.doi.org/10.1021/acs.jpcc.0c09659
J. Phys. Chem. C 2020, 124, 28159−28168

original acetyl−carbonyl group) can be excluded as in the opposite case an isotopic shift must be observed for the labeled component.

Summarizing the observations obtained in this coverage range, the absence of the C═O vibrational band related to acetyl−carbonyl arises from the nearly parallel the orientation of this band with respect to the metal surface.[27] In contrast, the C═O vibration of the ester−carbonyl is most likely visible but significantly red-shifted due to strong rehybridization of the related molecular orbital with the d-orbitals of underlying Pt leading to formation of η_2(CO) adsorption configuration. The earlier suggested models based on formation of enol, enolate, or enediolate species involving the original acetyl−carbonyl groups are inconsistent with the obtained IR spectra for isotopically labeled EP.

To further address the chemical nature of the adsorbed species and the origin of the band at 1530 cm^{-1}, the IR spectra were recorded at different EP coverages on pristine Pt(111) (Figure 2a) and on the same surface continuously exposed to H_2 at a constant EP coverage (Figure 2b). On pristine Pt(111), a combination of bands at 1530 and 1296 cm^{-1} is observed at the lowest coverage, while the band at 1268 cm^{-1} is missing. With increasing coverage, both bands at 1530 and 1296 cm^{-1} simultaneously grow in intensity (spectrum 2) and eventually saturate (spectra 3 and 4). The vibrational band $\nu(C-O)_{ester,2}$ at 1268 cm^{-1} appears at higher coverages (spectra 2 and 3) and grows in intensity when the EP coverage increases. It should be emphasized that the intensity distribution between the peaks at 1268 and 1296 cm^{-1} is clearly changing with increasing coverage. While at the lowest coverage the peak at 1268 cm^{-1} is not seen and the peak at 1296 cm^{-1} has a noticeable intensity, this difference becomes less pronounced at the highest coverage, at which the intensity of the band at 1268 cm^{-1} is just about factor of 2 lower than that of the band at 1296 cm^{-1}. This observation suggest that the species related to the band at 1268 cm^{-1} is either not present at the lowest coverage or is present at a negligibly small concentration. Interestingly, if the EP-containing surface is continuously exposed to H_2, the intensity distribution of these bands drastically changes: while the bands at 1530 and 1296 cm^{-1} gradually and simultaneously disappear, the band at 1268 cm^{-1} grows in intensity and becomes the dominant vibrational peak after prolonged H_2 exposure (Figure 2b).

The observed evolution of the vibrational bands suggests that at least two distinct types of surface species exist on Pt(111): (i) the species $S1_{(IRAS)}$, exhibiting a combination of two characteristic peaks at 1530 and 1296 cm^{-1}, and (ii) the species $S2_{(IRAS)}$, showing a prominent vibrational band at 1268 cm^{-1}. The relative abundance of these species strongly depends on the coverage conditions and the presence of coadsorbed H: (i) species $S1_{(IRAS)}$ appears already at the lowest coverage on pristine Pt(111) surface, while the species $S2_{(IRAS)}$ starts evolving with growing coverage of EP; (ii) the species $S1_{(IRAS)}$ almost completely converts into the species $S2_{(IRAS)}$ after prolonged H_2 exposure. It should be noted that quantitative information about the relative population of both types of EP species cannot be unambiguously deduced from the IR spectra. First, because of the metal surface selection rule,[27] the IR intensity depends on the projection of the dynamic dipole moment on the surface normal. With this, if a given bond is only slightly inclined with respect to the metal surface, the related vibrational band is seen as a low-intensity vibration. Additionally, dipole coupling effects, such as for example intensity transfer to high-frequency bands,[27,35] might result in diminishing the IR intensity of the low-frequency vibration. Despite these complications, it can be quite safely concluded that surface species with two distinctly different spectroscopic signatures can be distinguished on Pt(111), which exhibit different dependencies on the coverage condition and the presence of coadsorbed H.

The appearance of two distinct vibrational bands related to C−O vibration in the ester group suggests that this group can be involved in different type of interactions with the underlying metal and/or with the coadsorbed species. The adsorption configuration of these species was investigated by STM under temperature conditions nearly identical with those of the IRAS experiments (118 and 100 K, respectively). Figure 3a displays

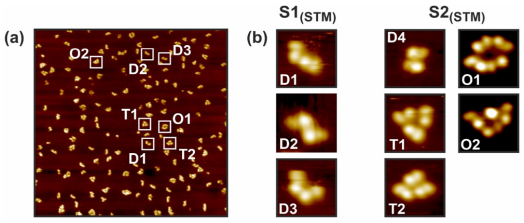

Figure 3. (a) STM image of EP adsorbed on pristine Pt(111) at 118 K (52.2 × 52.2 nm^2, full details in the Supporting Information). (b) Close-up images of different oligomers divided in $S1_{(STM)}$ (dimers D1, D2, and D3) and $S2_{(STM)}$ (dimer D4, trimers T1 and T2, tetramers O1 and O2) species. The dimer D4 was observed only on H-covered Pt(111) surface.

an image obtained on pristine Pt(111) showing the overview of different surface assemblies. Interestingly, nearly all adsorbed species are agglomerated in assemblies of two, three, or four individual molecules. The close-up images of these structures measured with submolecular resolution are displayed in Figure 3b. Generally, all assemblies consist of a combination of elongated protrusions exhibiting a brighter spot and a darker area. Specifically, four types of dimers (D1−D4), two types of trimers (T1, T2), and two types of tetramers (O1, O2) were identified in our studies. Note that dimer D4 evolves only on H-covered surface and is not present on pristine Pt(111). Figure 4a−c shows the full data set of STM images obtained as a function of coverage on pristine Pt(111), which changes in the range (1.8−70.7) × 10^{12} molecules/cm^2 as well as the statistical evaluation of the abundance of different types of oligomers. The STM images obtained on Pt(111) precovered with EP during continuous H_2 exposure and the statistical evaluation of the oligomer distribution obtained during this treatment are displayed in Figure 5a,b.

To find a correlation between the structure of the molecular assemblies as observed by STM and the type of intermolecular bonding in these assemblies deduced from IR spectra, we analyzed the structure of the assemblies with respect to the intermolecular intensity distribution. All molecular assemblies can be divided into two classes: (i) species $S1_{(STM)}$—the species interacting exclusively via the bright spots (D1−D3) and (ii) species $S2_{(STM)}$—the species interacting via the bright spot and a darker protrusion either exclusively (D4, T1, O1) or at least at part (T2, O2). For the latter species (T2, O2), the interaction between the bright and the dark protrusions is present as well as the interaction between two bright spots.

https://dx.doi.org/10.1021/acs.jpcc.0c09659
J. Phys. Chem. C 2020, 124, 28159−28168

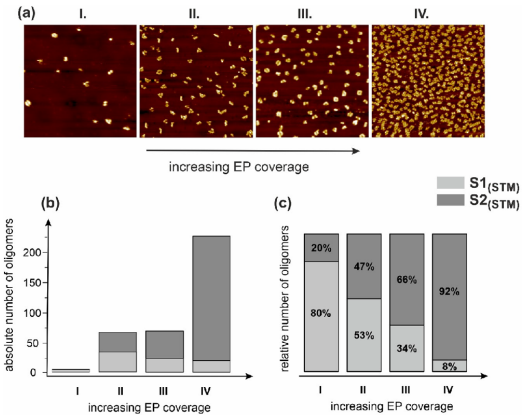

Figure 4. (a) STM images (37.3 × 37.3 nm^2) of EP adsorbed on pristine Pt(111) at different coverages at 100 K (full details in the Supporting Information). (b) Absolute number and (c) relative abundance of two types of surface species $S1_{(STM)}$ and $S2_{(STM)}$ shown for different EP surface coverages.

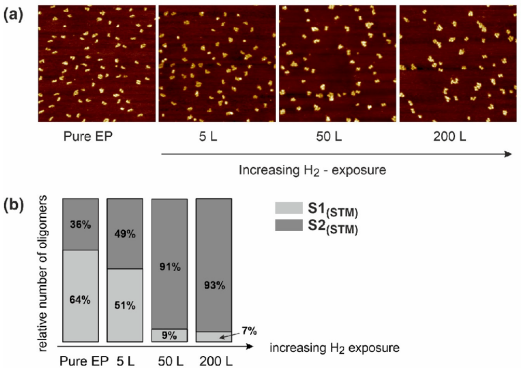

Figure 5. (a) STM images (32.9 × 32.9 nm^2) of EP adsorbed on Pt(111) obtained after different H_2 exposures indicated on the horizontal axis (full details in the Supporting Information). (b) Relative abundance of two types of surface species $S1_{(STM)}$ and $S2_{(STM)}$ shown for different H_2 exposures.

Figures 4b,c and 5b show the relative abundance of the species $S1_{(STM)}$ and $S2_{(STM)}$ as a function of increasing coverage (Figure 4b,c) and increasing H_2 exposure (Figure 5b). There is a clear trend observed in these plots on pristine Pt: the species $S1_{(STM)}$ prevails at low coverages, while at higher coverages the concentration of $S2_{(STM)}$ starts growing and this species eventually dominates. Note that the absolute amount of species $S1_{(STM)}$ in Figure 4b rather quickly levels off and remains almost constant up to the highest coverage (IV), while the abundance of species $S2_{(STM)}$ grows almost by 2 orders of magnitude between the lowest and the highest coverages (I and IV). For a series of the experiments involving H_2 exposure, the initial coverage distribution is chosen such that the relative population of surface oligomers on pristine Pt(111) surface amounts to 64% for the species $S1_{(STM)}$ (Figure 5a,b). During a continuous H_2 exposure, nearly full conversion of the species $S1_{(STM)}$ to $S2_{(STM)}$ is observed, while the overall concentration of adsorbed EP molecules does not notably change during H_2 treatment.

A strong correlation between the evolution of the surface assemblies detected by STM and the vibrational bands in the IR spectra can be established. The combination of two peaks appearing first on the pristine Pt(111) surface (1530 and 1296 cm^{-1}, species $S1_{(IRAS)}$) can be clearly correlated to the evolution of the species $S1_{(STM)}$, while the band at 1268 cm^{-1} (species $S2_{(IRAS)}$), evolving at higher coverages, correlates with the appearance of the species $S2_{(STM)}$. The evolution of the surface species on the H-containing surface is also in very good agreement with this assignment: while on the pristine surface the bands at 1530 and 1296 cm^{-1} are clearly visible in IR spectra and a large fraction of the microscopically observed assemblies are $S1_{(STM)}$ species, prolonged H_2 exposure results in nearly full conversion of the assemblies to $S2_{(STM)}$ species accompanied by the full conversion of the bands at 1530 and 1296 cm^{-1} ($S1_{(IRAS)}$) to the band 1268 cm^{-1} ($S2_{(IRAS)}$). With this, both investigated adsorption systems suggest a clear correlation between the spectroscopically detected species $S1_{(IRAS)}$ and microscopically observed assemblies $S1_{(STM)}$. Similarly, the appearance of the species $S2_{(IRAS)}$ correlates with the evolution of the surface assemblies $S2_{(STM)}$. On the basis of these correlations, it can be concluded that the lateral interaction typical for the species $S1_{(STM)}$ occurring via two bright spots leads to the vibrational signature comprising a combination of the bands 1530 and 1296 cm^{-1}, while the interaction via the bright sport and the dark protrusion results in the evolution of the vibrational band at 1268 cm^{-1}.

Based purely on intensity distribution in the STM data, it is not possible to assign a specific fragment of the EP molecule—the ester—or the acetyl—part of EP—to a bright or a dark protrusion seen in the STM images. In the previous studies on MP adsorbed on Pd(111), assignment of the STM intensity distribution was performed based on theoretical modeling of STM images.[18] Specifically, adsorption of the original MP molecule was found to result in a homogeneous intensity distribution, while the pattern comprising a bright and a dark protrusion was predicted for the enol form of MP, in which the acetyl−carbonyl group undergoes keto−enol tautomerization. In this enol species, the bright part of adsorbed MP was assigned to the ester part of the molecule. This assignment cannot be, however, transfer to EP adsorbed on Pt(111), as we can safely exclude formation of enol species involving the original acetyl−carbonyl group of EP on this surface.

It is important to note that the intensity distribution in the individual molecules constituting all oligomer species is very similar. Figure 6 shows three selected oligomers—dimer, trimer, and tetramer species (Figure 6a)—and the corresponding line profiles measured along the main axes connecting the bright and the dark protrusions (Figure 6b). All line profiles exhibit two maxima with typical distances between them indicated in Figure 6b. Each value was obtained from the statistical evaluation of line scans measured for 10−15 oligomers with the same structure. It can be seen that the intensity distribution and the distances between the intensity peaks in each individual molecule are very similar for all oligomers, suggesting that the chemical nature of the monomer species does not drastically alter due to lateral intermolecular interactions in the particular oligomer species. To address the intensity distribution in these individual EP molecules, we performed theoretical modeling of EP adsorption geometry in monomer species adsorbed on Pt(111) and the corresponding

https://dx.doi.org/10.1021/acs.jpcc.0c09659
J. Phys. Chem. C 2020, 124, 28159−28168

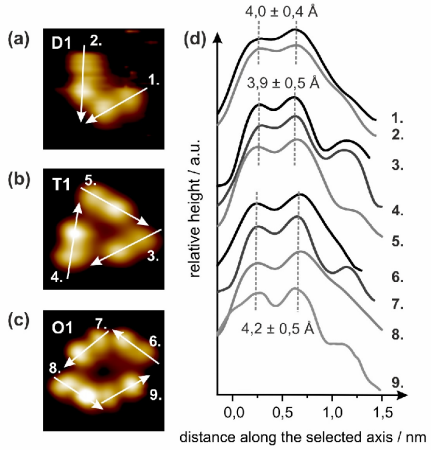

Figure 6. (a–c) Close-up images of selected oligomer species: dimer D1, trimer T1, and oligomer O1. (d) Line profiles measured along the axes 1–9 indicated at the close-up images.

STM image at the DFT level. The structural calculations were performed with the PBE functional and projector-augmented wave pseudopotentials; the STM images were simulated with the Tersoff–Hamann approach (for more details see the Methods section). Figure 7 shows the calculated structure of

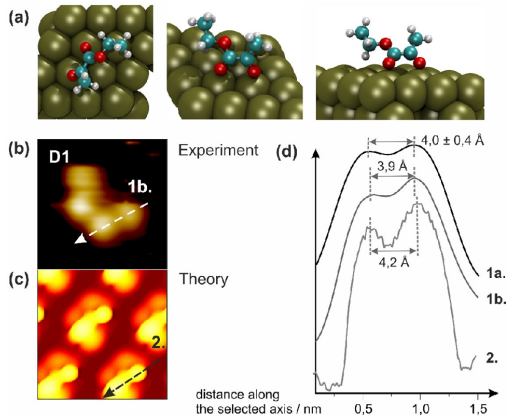

Figure 7. (a) Adsorption geometry of EP monomer calculated at the DFT level. (b, c) Experimental and theoretically calculated STM images. (d) STM line profiles along the axes shown in (b) and (c): (1a) is an average of 14 line profiles in individual EP monomers agglomerated in dimers D1 as shown in (b); (1b) is measured for a single EP monomer along the axis 1b; (2) is derived from the computed STM image shown in (c).

the EP monomer (Figure 7a) together with the experimental (Figure 7b) and modeled STM image (Figure 7c). Figure 7d displays the line profile derived from the experimental (lines 1a and 1b) and modeled (line 2) STM images along the main axis. Note that line 1b is related to the experimental STM image shown in Figure 7b, while line 1a is an average from 14 experimental line scans measured for D1 species. In the computed configuration both carbonyl groups are inclined and point down toward two Pt atoms, while the $(C_2H_5)C-O-$ group is lifted above the surface. It should be noted that the adsorption configuration of EP agglomerated in oligomers might differ from the one calculated for a monomer species. Currently, we perform detailed theoretical calculations at DFT, semiempirical, and force field levels to describe the intermolecular interactions in the whole variety of oligomer species, which will be the subject of upcoming reports. In this study, we mostly focus on the intensity distribution in the monomer species to draw conclusions on the position of brighter vs darker spots seen by STM in the individual molecule. For the computed adsorption configuration of the monomer, the modeled STM image exhibits an inhomogeneous intensity distribution with the higher intensity positioned at the acetyl part and the lower intensity relating to the ester part of EP. If this intensity distribution remains the same in the individual EP molecules involved in oligomers, the following conclusion can be made on the two observed types of lateral interactions. First, in the STM species $S1_{(STM)}$ exhibiting interaction between two bright spots, a H of the methyl group of one monomer is bonded to the acetyl–carbonyl of the other monomer. In this case, the ester groups are not directly involved in H-bonding between two monomers, which is consistent with the spectroscopic observation that the C–O bond of the ester group remains nearly unperturbed and the corresponding vibrational band has only a minor frequency shift with respect to the multilayer value (19 cm^{-1}). Second, in the STM species $S2_{(STM)}$ showing the interaction between the bright and the dark protrusions, a methyl group of one monomer must be H-bonded to one of the O atoms of the ester group. Taking into account the fact that the frequency of the C–O single bond (1268 cm^{-1}) is strongly red-shifted in this type of species (by 47 cm^{-1} as compared to the multilayer value), it can be quite safely concluded that the ester-O is involved in H-bonding with the H atom of the methyl group. This hypothesis is in excellent agreement with earlier IR studies reported for a large variety of O-containing hydrocarbon compounds in the liquid phase, in which the effects of H-bonding on vibrational frequencies of CO bonds were investigated.[31,32] Generally, the CO bonds show frequency shifts of 10–40 cm^{-1} from their unperturbed value upon establishing a H bond with a foreign molecule. Also in our earlier studies on adsorption of acetophenone on Pt(111), frequency shifts of 20–50 cm^{-1} were found for C=O vibration involved in H-bonding with one or two neighboring molecules.[9,11] The frequency shift of 28 cm^{-1} observed in this study (as compared to the value of nearly unperturbed species $S1_{(IRAS)}$ 1296 cm^{-1}) is in good quantitative agreement with the earlier reported typical range of a few tens of wavenumbers.

On the basis of these considerations, we propose adsorption configurations for different types of surface species shown in Figure 8, which are consistent with all experimental observations made in this study. Figure 8 shows a proposed configuration of the dimer species D1 and D3 (Figure 8a) and D2 (Figure 8b), in which the interaction is established between two acetyl groups of EP, which are predicted to appear as a bright protrusion in STM images (species $S1_{(IRAS)}/S1_{(STM)}$). Here, a H atom of the methyl group establishes H-bonding with the acetyl–carbonyl group of the second EP molecule. In this configuration, the ester C–O bond is not directly involved in intermolecular interaction, which is consistent with the spectroscopic observation that its vibrational frequency (1296

https://dx.doi.org/10.1021/acs.jpcc.0c09659
J. Phys. Chem. C 2020, 124, 28159–28168

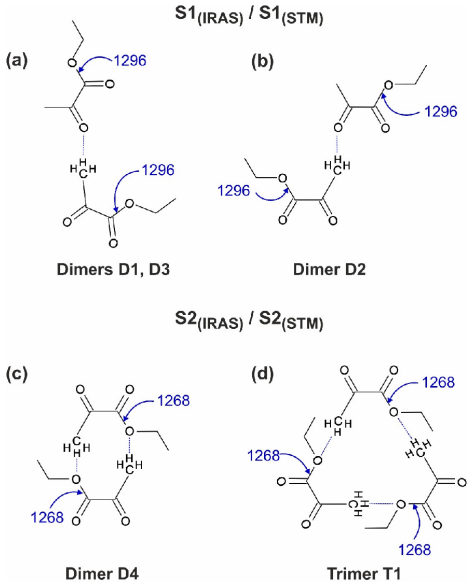

Figure 8. Proposed models for different types of EP oligomers: (a, b) the dimer assemblies formed between two acetyl groups related to the species $S1_{(IRAS)}/S1_{(STM)}$; (c, d) selected dimer and trimer assemblies formed between the acetyl and ester groups related to the species $S2_{(IRAS)}/S2_{(STM)}$.

cm^{-1}) is only slightly shifted as compared to the multilayer value (1314 cm^{-1}). The frequencies of the $\nu(C{-}O)_{ester}$ vibrational bands are highlighted in the models with blue color. Both acetyl−carbonyl groups of the dimer are most likely oriented close to parallel to the underlying metal surface, since the corresponding vibrational bands are not seen in the spectra. The only other observed prominent band at 1530 cm^{-1} is most likely related to one or both ester−carbonyl(s) of EP. As discussed above, the strong red-shift of this band can arise from substantial rehybridization of the related molecular orbital with the d-electrons of Pt and might be indicative of a $\eta_2(CO)$ configuration suggested in earlier studies for acetone adsorption. The experimentally observed configurations of the dimers D1 and D3 differ slightly with respect to the relative orientation of the individual molecules (see Figure 3b), which is most likely dictated by the underlying metal support. The stabilities of D1, D2, and D3 dimers on Pt(111) seem to be similar as these species are observed simultaneously.

The second type of interaction based on establishing a connection between the brighter and the darker protrusions of the surface species is exemplified for selected oligomer structures D4 and T1 (Figure 8c,d). In this type of species ($S2_{(IRAS)}/S2_{(STM)}$), the ester group of one molecule is involved into H-bonding with the methyl group of the neighboring species. This interaction results in a strong red-shift of the $\nu(C{-}O)_{ester}$ vibration to 1268 cm^{-1} observed spectroscopically. Because no other vibrational bands in the range of carbonyl groups could be observed for this species, it can be concluded that all C═O groups are oriented nearly parallel to the surface for this type of adsorption configuration. It should be noted that the species T2 and O2 exhibit not only the interaction between the bright and the dark protrusions but also the interaction between the bright and the bright protrusions. In this case, one molecule with be involved on one side into the acetyl−carbonyl/acetyl−methyl interaction, the same as in species $S1_{(IRAS)}$, and on the other side, the ester-O will be involved in the interaction with the methyl group of the acetyl entity of the neighboring species, the same as in species $S2_{(IRAS)}$.

It should be emphasized that the strong red-shift of the $\nu(C{-}O)_{ester}$ vibration observed for the second type of surface species $S2_{(IRAS)}/S2_{(STM)}$ implies that this bond is significantly weakened by the lateral interaction with the neighboring molecules as compared to the less perturbed $S1_{(IRAS)}/S1_{(STM)}$ state. This observation suggests that the chemical transformations involving this notably weakened ester bond might be significantly facilitated in the second type of complex. This phenomenon opens a prospect of rational control of the catalytic transformations involving ester groups by tuning the parameter space of a catalytic reaction, such as the concentration of surface adsorbates and the presence of coadsorbed H to create the second type of EP assembly with strongly weakened ester bonds.

Exposure of the EP-precovered surface to H_2 results in a complete switching of the intermolecular interaction from type $S1_{(IRAS)}/S1_{(STM)}$ to type $S2_{(IRAS)}/S2_{(STM)}$. In terms of the model discussed above, this means that H-bonding involving an acetyl−carbonyl group disappears, and the other type of bonding involving the ester-O atom evolves. This hypothesis is in an excellent agreement with our earlier studies on a the simple carbonyl compound acetophenone adsorbed on the Pt(111) surface.[9,12] While acetophenone was observed to form two types of dimers involving a carbonyl group on pristine Pt(111), exposure to H_2 below 240 K resulted in rupture of all H bonds and falling apart of all dimer species. This phenomenon originates most likely from a high propensity of carbonyl groups to build a quasi-H-bonding to H atoms adsorbed on the metal. In this case, the bonding of the carbonyl groups to surface-adsorbed H seems to produce a more stable surface species than acetophenone dimers connected via H-bonding between the carbonyl and the methyl group of the neighboring molecules. In the case of EP, a similar behavior is observed−in the presence of surface-adsorbed H the bonding involving a carbonyl group disappears. However, a different type of H-bonding involving the ester-O is possible in EP, which cannot be realized in a simple carbonyl acetophenone. As a result, a new type of intermolecular interaction prevails on H-covered surfaces, producing the $S2_{(IRAS)}/S2_{(STM)}$ species binding via the ester-O atom.

CONCLUSIONS

Summarizing, in this study the details of mutual lateral interactions in ethyl pyruvate oligomers adsorbed on well-defined Pt(111) surface were addressed by a combination of IRAS, STM, molecular beam techniques, and theoretical modeling at the DFT level. It was shown that EP forms a large number of different oligomer species including different types of dimers, trimers, and tetramers. Based on a combination of spectroscopic and microscopic observations, all species can be attributed to two large classes of oligomers exhibiting different types of intermolecular binding. The first class of species—$S1_{(IRAS)}/S1_{(STM)}$—comprising three topologically different types of dimers, shows two characteristic vibrational bands, related to nearly unperturbed C−O

https://dx.doi.org/10.1021/acs.jpcc.0c09659
J. Phys. Chem. C 2020, 124, 28159−28168

stretching vibration of the ester group and most likely strongly perturbed ester−carbonyl vibration. Intermolecular interaction in these species is realized via H-bonding between two acetyl groups, in which an O atom of the carbonyl group is bonded to a H atom of the methyl group of a neighboring molecule. In STM images, this species appears as dimers connected to each other via two bright protrusions. DFT modeling of the STM images performed for EP monomer species confirms that the position of the bright protrusion is related to the acetyl group of EP. The second class of species—$S2_{(IRAS)}/S2_{(STM)}$—comprising a dimer and four different types of trimers and tetramers, exhibits a characteristic vibrational band related to a strongly red-shifted C−O stretching vibration of an ester group $\nu(CO)_{ester,2}$. The shift is proposed to arise from a second type if intermolecular interaction involving H-bonding between the ester-O and the methyl group of neighboring EP. In STM images, the corresponding surface species show an interaction between the bright and the dark protrusions of the neighboring molecules. The latter type of interaction significantly weakens the ester bond as evidenced by a strong frequency shift, which might exert a considerable impact on the chemical transformations involving the ester group.

The abundance of both types of surface species depends on surface coverage of EP and on the presence of coadsorbed H. On the pristine surface, the species $S1_{(IRAS)}/S1_{(STM)}$ prevail at low coverages, while the species $S2_{(IRAS)}/S2_{(STM)}$ dominate in the high coverage regime. In the presence of H, the species $S1_{(IRAS)}/S1_{(STM)}$ become fully converted into the species $S2_{(IRAS)}/S2_{(STM)}$, suggesting that the binding via acetyl groups converts to binding via the acetyl−ester entities on H-containing surfaces. With this, the type of intermolecular interaction in ethyl pyruvate assemblies can be effectively tuned by changing the adsorption parameters, such as surface coverage and the presence of coadsorbed hydrogen, providing by this an experimentally accessible way to affect the strength of the ester bond by changing the nature and concentration of coadsorbed species.

The obtained results provide important insights into the details of lateral interactions of complex multifunctional molecules adsorbed on catalytically relevant surfaces. We show that the parameter space in a catalytic process involving ester compounds can be purposefully varied to tune the strength of the ester bond toward improving the catalytic performance.

■ ASSOCIATED CONTENT

Supporting Information

The Supporting Information is available free of charge at https://pubs.acs.org/doi/10.1021/acs.jpcc.0c09659.

Assignment of vibrational modes of ethyl pyruvate (Table S1); full figure caption for Figures 2−5 (PDF)

■ AUTHOR INFORMATION

Corresponding Author

Swetlana Schauermann − *Institut für Physikalische Chemie, Christian-Albrechts-Universität zu Kiel, 24118 Kiel, Germany*; orcid.org/0000-0002-9390-2024; Email: schauermann@pctc.uni-kiel.de

Authors

Carsten Schröder − *Institut für Physikalische Chemie, Christian-Albrechts-Universität zu Kiel, 24118 Kiel, Germany*

Marvin C. Schmidt − *Institut für Physikalische Chemie, Christian-Albrechts-Universität zu Kiel, 24118 Kiel, Germany*

Christopher Witt − *Institut für Physikalische Chemie, Christian-Albrechts-Universität zu Kiel, 24118 Kiel, Germany*

Smadar Attia − *Institut für Physikalische Chemie, Christian-Albrechts-Universität zu Kiel, 24118 Kiel, Germany*

Jann Weber − *Institut für Physikalische Chemie, Christian-Albrechts-Universität zu Kiel, 24118 Kiel, Germany*

Ann-Katrin Baumann − *Institut für Physikalische Chemie, Christian-Albrechts-Universität zu Kiel, 24118 Kiel, Germany*

Bernd Hartke − *Institut für Physikalische Chemie, Christian-Albrechts-Universität zu Kiel, 24118 Kiel, Germany*; orcid.org/0000-0001-8480-0862

Complete contact information is available at: https://pubs.acs.org/10.1021/acs.jpcc.0c09659

Notes

The authors declare no competing financial interest.

■ ACKNOWLEDGMENTS

Financial support by the German Science Foundations (DFG, Grants SCHA 1477/3-1 and HA 2498/16-2) is gratefully acknowledged.

■ REFERENCES

(1) Somorjai, G. A. *Introduction to Surface Chemistry and Catalysis*, 2nd ed.; John Wiley & Sons: New York, 2010.

(2) Meemken, F.; Baiker, A. Recent Progress in Heterogeneous Asymmetric Hydrogenation of C═O and C═C Bonds on Supported Noble Metal Catalysts. *Chem. Rev.* **2017**, *117*, 11522−11569.

(3) Gellman, A. J.; Tysoe, W. T.; Zaera, F. Surface Chemistry for Enantioselective Catalysis. *Catal. Lett.* **2015**, *145*, 220−232.

(4) Marshall, S. T.; O'Brien, M.; Oetter, B.; Corpuz, A.; Richards, R. M.; Schwartz, D. K.; Medlin, J. W. Controlled Selectivity for Palladium Catalysts Using Self-Assembled Monolayers. *Nat. Mater.* **2010**, *9*, 853−858.

(5) Marshall, S. T.; Medlin, J. W. Surface-Level Mechanistic Studies of Adsorbate−Adsorbate Interactions in Heterogeneous Catalysis by Metals. *Surf. Sci. Rep.* **2011**, *66*, 173−184.

(6) Tysoe, W. *Molecular-Level Design of Heterogeneous Chiral Catalysts*, 2018; DOI: 10.2172/1160339.

(7) Ernst, J. B.; Schwermann, C.; Yokota, G.-i.; Tada, M.; Muratsugu, S.; Doltsinis, N. L.; Glorius, F. Molecular Adsorbates Switch on Heterogeneous Catalysis: Induction of Reactivity by N-Heterocyclic Carbenes. *J. Am. Chem. Soc.* **2017**, *139*, 9144−9147.

(8) Dostert, K.-H.; O'Brien, C. P.; Ivars-Barceló, F.; Schauermann, S.; Freund, H.-J. Spectators Control Selectivity in Surface Chemistry: Acrolein Partial Hydrogenation over Pd. *J. Am. Chem. Soc.* **2015**, *137*, 13496−13502.

(9) Attia, S.; Schmidt, M.-C.; Schröder, C.; Pessier, P.; Schauermann, S. Surface-Driven Keto−Enol Tautomerization: Atomistic Insights into Enol Formation and Stabilization Mechanisms. *Angew. Chem., Int. Ed.* **2018**, *57*, 16659−16664.

(10) Attia, S.; Schauermann, S. Coverage-Dependent Adsorption Geometry of Acetophenone on Pt(111). *J. Phys. Chem. C* **2020**, *124*, 557−566.

(11) Attia, S.; Schmidt, M. C.; Schröder, C.; Schauermann, S. Formation and Stabilization Mechanisms of Enols on Pt through Multiple Hydrogen Bonding. *ACS Catal.* **2019**, *9*, 6882−6889.
(12) Attia, S.; Schmidt, M. C.; Schröder, C.; Weber, J.; Baumann, A.-K.; Schauermann, S. Keto−Enol Tautomerization as a First Step in Hydrogenation of Carbonyl Compounds. *J. Phys. Chem. C* **2019**, *123*, 29271−29277.
(13) Attia, S.; Spadafora, E. J.; Schmidt, M. C.; Schröder, C.; Baumann, A.-K.; Schauermann, S. Adsorption Geometry and Self-Assembling of Chiral Modifier (R)-(+)-1-(1-Naphthylethylamine) on Pt(111). *Phys. Chem. Chem. Phys.* **2020**, *22*, 15696−15706.
(14) Schmidt, M. C.; Attia, S.; Schröder, C.; Baumann, A.-K.; Pessier, P.; Schauermann, S. Temperature-Dependent Formation of Acetophenone Oligomers Accompanied by Keto−Enol Tautomerism: Real Space Distribution. *J. Phys. Chem. C* **2020**, *124*, 14262−14271.
(15) Dostert, K.-H.; O'Brien, C. P.; Mirabella, F.; Ivars-Barceló, F.; Attia, S.; Spadafora, E.; Schauermann, S.; Freund, H.-J. Selective Partial Hydrogenation of Acrolein on Pd: A Mechanistic Study. *ACS Catal.* **2017**, *7*, 5523−5533.
(16) Schauermann, S.; Freund, H.-J. Model Approach in Heterogeneous Catalysis: Kinetics and Thermodynamics of Surface Reactions. *Acc. Chem. Res.* **2015**, *48*, 2775−2782.
(17) Liu, W.; Savara, A.; Ren, X.; Ludwig, W.; Dostert, K.-H.; Schauermann, S.; Tkatchenko, A.; Freund, H.-J.; Scheffler, M. Toward Low-Temperature Dehydrogenation Catalysis: Isophorone Adsorbed on Pd(111). *J. Phys. Chem. Lett.* **2012**, *3*, 582−586.
(18) Garvey, M.; Bai, Y.; Boscoboinik, J. A.; Burkholder, L.; Sorensen, T. E.; Tysoe, W. T. Identifying Molecular Species on Surfaces by Scanning Tunneling Microscopy: Methyl Pyruvate on Pd(111). *J. Phys. Chem. C* **2013**, *117*, 4505−4514.
(19) Mahapatra, M.; Burkholder, L.; Garvey, M.; Bai, Y.; Saldin, D. K.; Tysoe, W. T. Enhanced Hydrogenation Activity and Diastereomeric Interactions of Methyl Pyruvate Co-Adsorbed with R-1-(1-Naphthyl)Ethylamine on Pd(111). *Nat. Commun.* **2016**, *7*, 12380.
(20) Burkholder, L.; Tysoe, W. T. Structure and Reaction Pathways of Methyl Pyruvate on Pd(111). *J. Phys. Chem. C* **2009**, *113*, 15298−15306.
(21) Lavoie, S.; Laliberté, M.-A.; Mahieu, G.; Demers-Carpentier, V.; McBreen, P. Keto-Enol Driven Assembly of Methyl Pyruvate on Pt(111). *J. Am. Chem. Soc.* **2007**, *129*, 11668−11669.
(22) Lavoie, S.; Laliberté, M. A.; McBreen, P. H. Adsorption States and Modifier−Substrate Interactions on Pt(111) Relevant to the Enantioselective Hydrogenation of Alkyl Pyruvates in the Orito Reaction. *J. Am. Chem. Soc.* **2003**, *125*, 15756−15757.
(23) Bürgi, T.; Atamny, F.; Knop-Gericke, A.; Hävecker, M.; Schedel-Niedrig, T.; Schlögl, R.; Baiker, A. Adsorption Mode of Ethyl Pyruvate on Platinum: An in Situ Xanes Study. *Catal. Lett.* **2000**, *66*, 109−112.
(24) Attia, S.; Spadafora, E. J.; Hartmann, J.; Freund, H.-J.; Schauermann, S. Molecular Beam/Infrared Reflection-Absorption Spectroscopy Apparatus for Probing Heterogeneously Catalyzed Reactions on Functionalized and Nanostructured Model Surfaces. *Rev. Sci. Instrum.* **2019**, *90*, 053903.
(25) Demers-Carpentier, V.; Rasmussen, A. M. H.; Goubert, G.; Ferrighi, L.; Dong, Y.; Lemay, J.-C.; Masini, F.; Zeng, Y.; Hammer, B.; McBreen, P. H. Stereodirection of an A-Ketoester at Sub-Molecular Sites on Chirally Modified Pt(111): Heterogeneous Asymmetric Catalysis. *J. Am. Chem. Soc.* **2013**, *135*, 9999−10002.
(26) Castonguay, M.; Roy, J. R.; Rochefort, A.; McBreen, P. H. Orientation and Conformation of Methyl Pyruvate on Ni(111). *J. Am. Chem. Soc.* **2000**, *122*, 518−524.
(27) Hoffmann, F. M. Infrared Reflection-Absorption Spectroscopy of Adsorbed Molecules. *Surf. Sci. Rep.* **1983**, *3*, 107−192.
(28) Dostert, K.-H.; O'Brien, C. P.; Liu, W.; Riedel, W.; Savara, A.; Tkatchenko, A.; Schauermann, S.; Freund, H.-J. Adsorption of Isophorone and Trimethyl-Cyclohexanone on Pd(111): A Combination of Infrared Reflection Absorption Spectroscopy and Density Functional Theory Studies. *Surf. Sci.* **2016**, *650*, 149−160.
(29) Zaera, F. An Organometallic Guide to the Chemistry of Hydrocarbon Moieties on Transition Metal Surfaces. *Chem. Rev.* **1995**, *95*, 2651−2693.
(30) Ma, Z.; Zaera, F. Organic Chemistry on Solid Surfaces. *Surf. Sci. Rep.* **2006**, *61*, 229−281.
(31) Fried, S. D.; Bagchi, S.; Boxer, S. G. Measuring Electrostatic Fields in Both Hydrogen-Bonding and Non-Hydrogen-Bonding Environments Using Carbonyl Vibrational Probes. *J. Am. Chem. Soc.* **2013**, *135*, 11181−11192.
(32) Nolasco, M. M.; Ribeiro-Claro, P. J. A.; Paulo, J. A. C-H···O Hydrogen Bonds in Cyclohexenone Reveal the Spectroscopic Behavior of C_{sp3}-H and C_{sp2}-H Donors. *ChemPhysChem* **2005**, *6*, 496−502.
(33) Vannice, M. A.; Erley, W.; Ibach, H. A Rairs and HREELS Study of Acetone on Pt(111). *Surf. Sci.* **1991**, *254*, 1−11.
(34) Vannice, M. A.; Erley, W.; Ibach, H. A Rairs and Hreels Study of Isopropyl Alcohol on Pt(111). *Surf. Sci.* **1991**, *254*, 12−20.
(35) Hollins, P. The Influence of Surface Defects on the Infrared Spectra of Adsorbed Species. *Surf. Sci. Rep.* **1992**, *16*, 51−94.

https://dx.doi.org/10.1021/acs.jpcc.0c09659
J. Phys. Chem. C 2020, 124, 28159−28168

6 | Summary and Outlook

In this thesis global optimization with evolutionary algorithms has been applied to molecules on surfaces, following up on the adsorption of Lennard-Jones clusters on Lennard-Jones surfaces. Several FF and SEQM methods have been considered and tested on multiple molecules. For benzene, ReaxFF clearly described the adsorption geometry of a single molecule best with respect to DFT reference data. For acetophenone, the adsorption of monomers from ReaxFF and GFN-FF were similar and both did not fully represent the DFT reference. The acetophenone dimers that have been optimized with GFN-FF were adsorbed next to each other and the functional groups were pointing outward. This does not agree well with experimental results. For ethyl pyruvate, the adsorbed minima have all been optimized with GFN-FF. The global minimum for the monomer agrees well with DFT data that has been calculated using Quantum ESPRESSO with the PBE functional. At this point the argument should be made that the globally optimized monomer could easily have been cut out of the surface with a small slab, which could then have been optimized with Quantum ESPRESSO to obtain the same structure and STM results. This then constitutes the full workflow as postulated in the Introduction.

In this thesis only a few select molecules have been analyzed and Pt(111) surfaces have been used almost exclusively. The reason for this choice was on the one hand motivated by having collaborators who were working on the same molecules on Pt(111) surface slabs in their experiments. On the other hand the availability of ReaxFF parameters for the Pt(111) surface was also an initial factor. The main conclusion is that Ogolem in combination with an appropriate method can deliver promising adsorption geometries without any prior information about the adsorption. Of the tested methods GFN-FF and ReaxFF have shown to be the most promising. There are now multiple avenues to continue improving upon this presented work. One possibility would be to improve the parametrization of GFN-FF with a focus on surface adsorption. Another option would be to create additional ReaxFF parametrizations for more surfaces analogously to Ref. 56. The performance of these methods on a broader variety of molecules could also be tested. One such example is naphthyl ethyl amine (NEA), which is a larger aromatic system (Fig. 6.1). The coadsorption of different molecules and their interaction on a surface could also be investigated by these tools. An example of this is shown in Fig. 6.2 where an acetophenone molecule and an NEA molecule are adsorbed next to each other.

But additional attention should also be paid to the semiempirical methods, both for the adsorption of metal clusters on metals and of molecules on surfaces. In addition to the

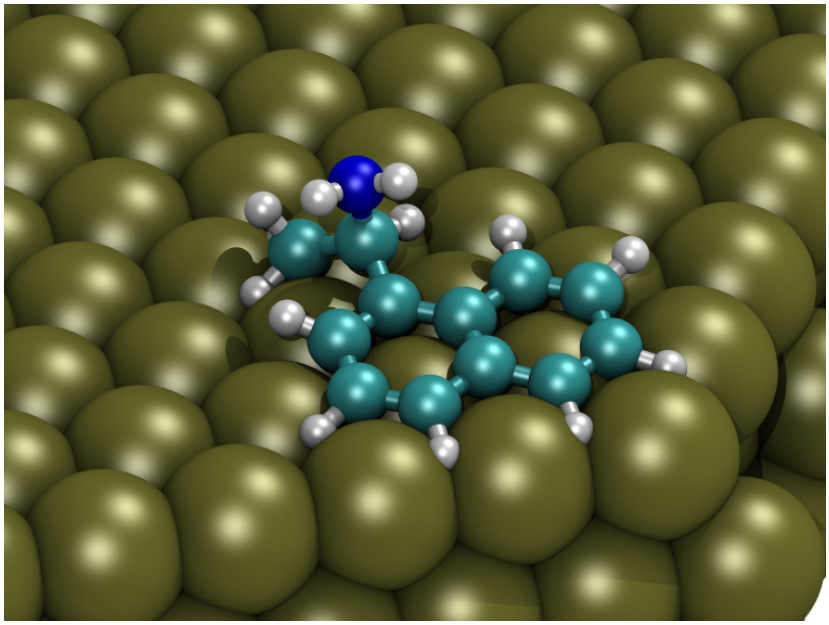

Figure 6.1: Globally optimized naphthyl ethyl amine adsorbed on a Pt(111) surface.

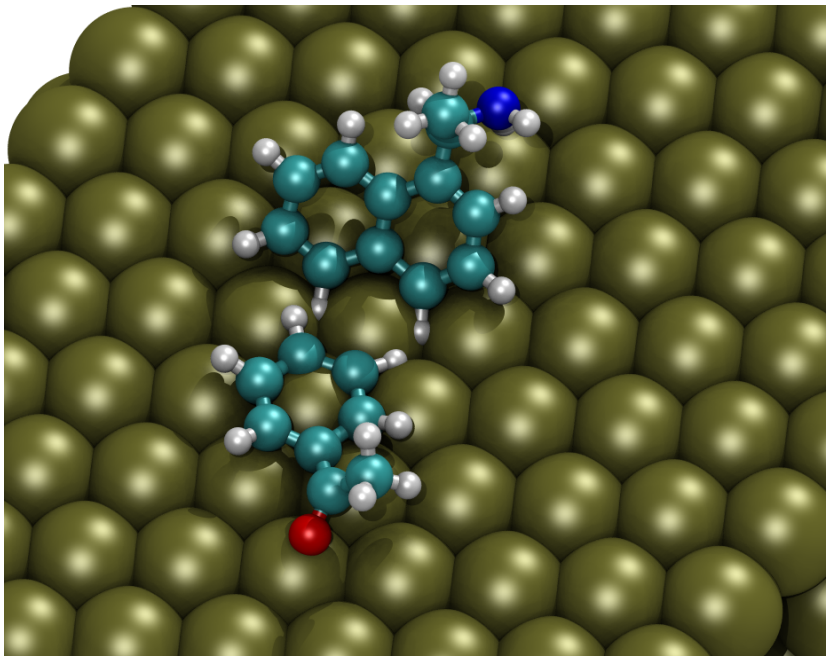

Figure 6.2: An acetophenone and an NEA molecule coadsorbed on a Pt(111) surface.

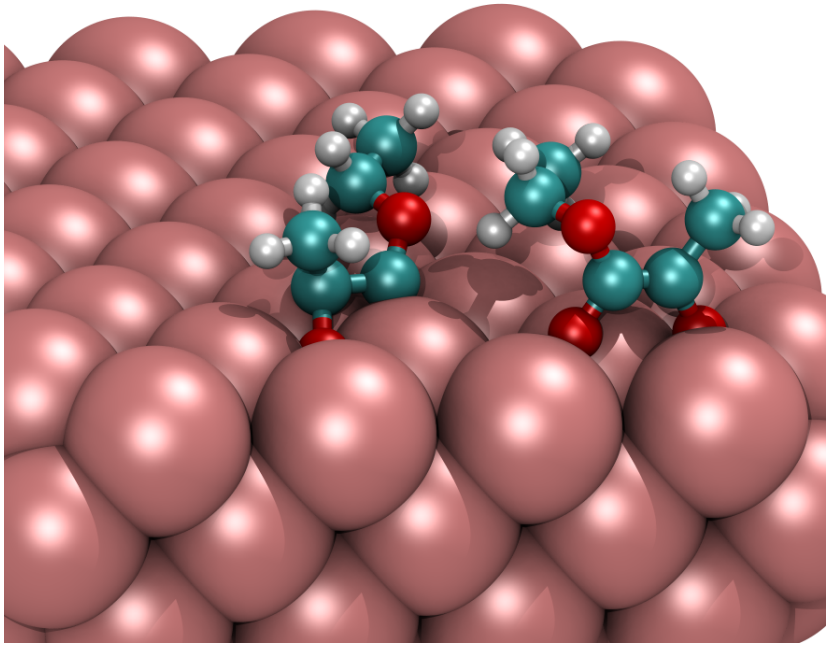

Figure 6.3: Ethyl pyruvate dimer on an Al(100) surface optimized with Ogolem and GFN1.

optimization of Al atoms on an Al(100) surface in section 4.2 the optimization of ethyl pyruvate molecules on the same surface was possible with this method (Fig. 6.3). For DFTB there were parameters for C, H, O, Au and Ag mentioned in Ref. 16 that should be available upon request from the authors of that publication. A recent publication has shown the promise of global optimization of nanoclusters with DFTB [96], the combination of promising global optimization and parameters suitable for molecules on surfaces makes this an interesting method to consider.

In addition to improvements to the backend methods, the global optimization method could also possibly be improved. Following the arguments made in Ref. 14 biasing the optimization algorithms towards surface-adsorbed molecules could reduce the computational cost significantly. In the case of Ogolem there are already surface-specific algorithms implemented, but the initialization of the individuals still occurs in a spherical shape. This could be replaced by e.g. a cuboid shape by modifying the packing algorithm[1].

[1] To the authors knowledge there is already ongoing work in this area.

Bibliography

[1] G. Ertl, "Reactions at Surfaces: From Atoms to Complexity (Nobel Lecture)," *Angewandte Chemie International Edition*, vol. 47, no. 19, pp. 3524–3535, 2008.

[2] P. B. Weisz, "Polyfunctional Heterogeneous Catalysis," vol. 13 of *Advances in Catalysis*, pp. 137–190, Academic Press, 1962.

[3] R. M. Laine, "Comments on the Mechanisms of Heterogeneous Catalysis of the Hydrodenitrogenation Reaction," *Catalysis Reviews*, vol. 25, no. 3, pp. 459–474, 1983.

[4] N. Mizuno and M. Misono, "Heterogeneous Catalysis," *Chemical Reviews*, vol. 98, pp. 199—218, February 1998.

[5] M. Bowker, "The Basis and Applications of Heterogeneous Catalysis," *Oxford Chemistry Primers*, vol. 53, no. 1, 1998.

[6] J. V. Lauritsen, R. T. Vang, and F. Besenbacher, "From atom-resolved scanning tunneling microscopy (STM) studies to the design of new catalysts," *Catalysis Today*, vol. 111, no. 1, pp. 34–43, 2006.

[7] C. Lamberti, A. Zecchina, E. Groppo, and S. Bordiga, "Probing the surfaces of heterogeneous catalysts by in situ IR spectroscopy," *Chemical Society Reviews*, vol. 39, pp. 4951—5001, December 2010.

[8] H. Kim, K. M. Kosuda, R. P. Van Duyne, and P. C. Stair, "Resonance Raman and surface- and tip-enhanced raman spectroscopy methods to study solid catalysts and heterogeneous catalytic reactions.," *Chemical Society Reviews*, vol. 39, 1 2010.

[9] A. M. H. Rasmussen, M. N. Groves, and B. Hammer, "Remote Activation of Chemical Bonds in Heterogeneous Catalysis," *ACS Catalysis*, vol. 4, no. 4, pp. 1182–1188, 2014.

[10] A. Freibert, J. M. Dieterich, and B. Hartke, "Exploring self-organization of molecular tether molecules on a gold surface by global structure optimization," *Journal of Computational Chemistry*, vol. 40, no. 22, pp. 1978–1989, 2019.

[11] A. A. Peterson, "Global Optimization of Adsorbate–Surface Structures While Preserving Molecular Identity," *Topics in Catalysis*, vol. 57, no. 1-4, pp. 40–53, 2014.

[12] B. Hartke, "Global optimization," *WIREs Computational Molecular Science*, vol. 1, no. 6, pp. 879–887, 2011.

[13] T. Weise, "Global optimization algorithms-theory and application," *Self-Published Thomas Weise*, 2009.

[14] B. Hartke, "Non-deterministic global structure optimization: An introductory tutorial," No. 32 in Reviews in Computational Chemistry, Wiley, 2020(estd.).

[15] V. Obersteiner, M. Scherbela, L. Hörmann, D. Wegner, and O. T. Hofmann, "Structure Prediction for Surface-Induced Phases of Organic Monolayers: Overcoming the Combinatorial Bottleneck," *Nano Letters*, vol. 17, no. 7, pp. 4453–4460, 2017.

[16] K. Krautgasser, C. Panosetti, D. Palagin, K. Reuter, and R. J. Maurer, "Global structure search for molecules on surfaces: Efficient sampling with curvilinear coordinates," *The Journal of Chemical Physics*, vol. 145, no. 8, p. 084117, 2016.

[17] G. Copie, Y. Makoudi, C. Krzeminski, F. Cherioux, F. Palmino, S. Lamare, B. Grandidier, and F. Cleri, "Atomic scale modeling of two-dimensional molecular self-assembly on a passivated si surface," *The Journal of Physical Chemistry C*, vol. 118, no. 24, pp. 12817–12825, 2014.

[18] G. Copie, F. Cleri, Y. Makoudi, C. Krzeminski, M. Berthe, F. Cherioux, F. Palmino, and B. Grandidier, "Surface-induced optimal packing of two-dimensional molecular networks," *Physical Review Letters*, vol. 114, no. 6, p. 066101, 2015.

[19] Y. Zhao, Q. Wu, Q. Chen, and J. Wang, "Molecular self-assembly on two-dimensional atomic crystals: insights from molecular dynamics simulations," *The Journal of Physical Chemistry Letters*, vol. 6, no. 22, pp. 4518–4524, 2015.

[20] J. van der Lit, J. L. Marsman, R. S. Koster, P. H. Jacobse, S. A. den Hartog, D. Vanmaekelbergh, R. J. Klein Gebbink, L. Filion, and I. Swart, "Modeling the self-assembly of organic molecules in 2D molecular layers with different structures," *The Journal of Physical Chemistry C*, vol. 120, no. 1, pp. 318–323, 2016.

[21] H. D. Castillo, J. M. Espinosa-Duran, J. R. Dobscha, D. C. Ashley, S. Debnath, B. E. Hirsch, S. R. Schrecke, M.-H. Baik, P. J. Ortoleva, K. Raghavachari, *et al.*, "Amphiphile self-assembly dynamics at the solution-solid interface reveal asymmetry in head/tail desorption," *Chemical Communications*, vol. 54, no. 72, pp. 10076–10079, 2018.

[22] S. Fortuna, D. L. Cheung, and K. Johnston, "Phase behaviour of self-assembled monolayers controlled by tuning physisorbed and chemisorbed states: A lattice-model view," *The Journal of Chemical Physics*, vol. 144, no. 13, p. 134707, 2016.

[23] C. Gobbo, I. Beurroies, D. de Ridder, R. Eelkema, S. J. Marrink, S. De Feyter, J. H. van Esch, and A. H. de Vries, "MARTINI model for physisorption of organic molecules on graphite," *The Journal of Physical Chemistry C*, vol. 117, no. 30, pp. 15623–15631, 2013.

[24] T. J. Roussel, E. Barrena, C. Ocal, and J. Faraudo, "Predicting supramolecular self-assembly on reconstructed metal surfaces," *Nanoscale*, vol. 6, no. 14, pp. 7991–8001, 2014.

[25] B. E. Hirsch, K. P. McDonald, A. H. Flood, and S. L. Tait, "Living on the edge: Tuning supramolecular interactions to design two-dimensional organic crystals near the boundary of two stable structural phases," *The Journal of Chemical Physics*, vol. 142, no. 10, p. 101914, 2015.

[26] A. Franke and E. Pehlke, "First-principles study of 1, 4-butanedithiol molecules and radicals adsorbed on unreconstructed au (111) and au (100)," *Physical Review B*, vol. 81, no. 7, p. 075409, 2010.

[27] J. C. Schön, C. Oligschleger, and J. Cortes, "Prediction and clarification of structures of (bio) molecules on surfaces," *Zeitschrift für Naturforschung B*, vol. 71, no. 5, pp. 351–374, 2016.

[28] A. S. Bazhenov and K. Honkala, "Globally optimized equilibrium shapes of zirconia-supported Rh and Pt nanoclusters: insights into site assembly and reactivity," *The Journal of Physical Chemistry C*, vol. 123, no. 12, pp. 7209–7216, 2019.

[29] G. Sun, A. N. Alexandrova, and P. Sautet, "Pt8 cluster on alumina under a pressure of hydrogen: Support-dependent reconstruction from first-principles global optimization," *The Journal of Chemical Physics*, vol. 151, no. 19, p. 194703, 2019.

[30] V. Gorbunov, S. Akimenko, and A. Myshlyavtsev, "Cross-impact of surface and interaction anisotropy in the self-assembly of organic adsorption monolayers: a monte carlo and transfer-matrix study," *Physical Chemistry Chemical Physics*, vol. 19, no. 26, pp. 17111–17120, 2017.

[31] C.-H. Su, H.-L. Chen, S.-J. Sun, S.-P. Ju, T.-H. Hou, and C.-H. Lin, "Observing the three-dimensional terephthalic acid supramolecular growth mechanism on a

stearic acid buffer layer by molecular simulation methods," *RSC Advances*, vol. 10, no. 3, pp. 1319–1330, 2020.

[32] H.-W. Yang, S.-P. Ju, C.-H. Cheng, Y.-T. Chen, Y.-S. Lin, and S.-T. Pang, "Aptasensor designed via the stochastic tunneling-basin hopping method for biosensing of vascular endothelial growth factor," *Biosensors and Bioelectronics*, vol. 119, pp. 25–33, 2018.

[33] S. N. Fejer, "Minimalistic coarse-grained modeling of viral capsid assembly," in *Progress in Molecular Biology and Translational Science*, vol. 170, pp. 405–434, Elsevier, 2020.

[34] J. B. A. Davis, S. L. Horswell, and R. L. Johnston, "Global Optimization of 8–10 Atom Palladium–Iridium Nanoalloys at the DFT Level," *The Journal of Physical Chemistry A*, vol. 118, no. 1, pp. 208–214, 2014.

[35] I. Demiroglu, K. Yao, H. A. Hussein, and R. L. Johnston, "DFT Global Optimization of Gas-Phase Subnanometer Ru–Pt Clusters," *The Journal of Physical Chemistry C*, vol. 121, no. 20, pp. 10773–10780, 2017.

[36] C. G. Broyden, "The Convergence of a Class of Double-rank Minimization Algorithms 1. General Considerations," *IMA Journal of Applied Mathematics*, vol. 6, pp. 76–90, 03 1970.

[37] R. Fletcher, "A new approach to variable metric algorithms," *The Computer Journal*, vol. 13, pp. 317–322, 01 1970.

[38] D. Goldfarb, "A family of variable metric methods derived by variations means," *Mathematics of Computation*, vol. 24, pp. 23–26, 1970.

[39] D. Shanno, "Conditioning of quasi-newton methods for function minimization," *Mathematics of Computation*, vol. 24, pp. 647–656, 1970.

[40] J. M. Dieterich and B. Hartke, "OGOLEM: Global cluster structure optimisation for arbitrary mixtures of flexible molecules. a multiscaling, object-oriented approach," *Molecular Physics*, vol. 108, no. 3-4, pp. 279–291, 2010.

[41] F. A. Momany and R. Rone, "Validation of the general purpose QUANTA® 3.2/CHARMm® force field," *Journal of Computational Chemistry*, vol. 13, no. 7, pp. 888–900, 1992.

[42] P. Bjelkmar, P. Larsson, M. A. Cuendet, B. Hess, and E. Lindahl, "Implementation of the CHARMM force field in GROMACS: analysis of protein stability effects from correction maps, virtual interaction sites, and water models," *Journal of Chemical Theory and Computation*, vol. 6, no. 2, pp. 459–466, 2010.

[43] W. L. Jorgensen, D. S. Maxwell, and J. Tirado-Rives, "Development and Testing of the OPLS All-Atom Force Field on Conformational Energetics and Properties of Organic Liquids," *Journal of the American Chemical Society*, vol. 118, no. 45, pp. 11225–11236, 1996.

[44] H. A. Lorentz, "Ueber die Anwendung des Satzes vom Virial in der kinetischen Theorie der Gase," *Annalen der Physik*, vol. 248, no. 1, pp. 127–136, 1881.

[45] D. Berthelot, "Sur le melánge des gaz," *Comptes rendu hebdomadaires des séances de l'Académie des Sciences*, no. 126, pp. 1703–1855, 1898.

[46] R. J. Good and C. J. Hope, "New Combining Rule for Intermolecular Distances in Intermolecular Potential Functions," *The Journal of Chemical Physics*, vol. 53, no. 2, pp. 540–543, 1970.

[47] "https://lammps.sandia.gov/doc/dihedral_opls.html, accessed Nov 09th 2020."

[48] S. J. Weiner, P. A. Kollman, D. A. Case, U. C. Singh, C. Ghio, G. Alagona, S. Profeta, and P. Weiner, "A new force field for molecular mechanical simulation of nucleic acids and proteins," *Journal of the American Chemical Society*, vol. 106, no. 3, pp. 765–784, 1984.

[49] J. Wang, R. M. Wolf, J. W. Caldwell, P. A. Kollman, and D. A. Case, "Development and testing of a general AMBER force field," *Journal of Computational Chemistry*, vol. 25, no. 9, pp. 1157–1174, 2004.

[50] A. C. T. van Duin, S. Dasgupta, F. Lorant, and W. A. Goddard, "ReaxFF: A Reactive Force Field for Hydrocarbons," *The Journal of Physical Chemistry A*, vol. 105, no. 41, pp. 9396–9409, 2001.

[51] K. Chenoweth, A. C. T. van Duin, and W. A. Goddard, "ReaxFF Reactive Force Field for Molecular Dynamics Simulations of Hydrocarbon Oxidation," *The Journal of Physical Chemistry A*, vol. 112, no. 5, pp. 1040–1053, 2008.

[52] M. Dittner, J. Müller, H. M. Aktulga, and B. Hartke, "Efficient global optimization of reactive force-field parameters," *Journal of Computational Chemistry*, vol. 36, no. 20, pp. 1550–1561, 2015.

[53] G. Shchygol, A. Yakovlev, T. Trnka, A. C. T. van Duin, and T. Verstraelen, "ReaxFF Parameter Optimization with Monte-Carlo and Evolutionary Algorithms: Guidelines and Insights," *Journal of Chemical Theory and Computation*, vol. 15, no. 12, pp. 6799–6812, 2019.

[54] D. Furman and D. J. Wales, "Transforming the Accuracy and Numerical Stability of ReaxFF Reactive Force Fields," *The Journal of Physical Chemistry Letters*, vol. 10, no. 22, pp. 7215–7223, 2019.

[55] D. Furman and D. J. Wales, "A well-behaved theoretical framework for ReaxFF reactive force fields," *The Journal of Chemical Physics*, vol. 153, no. 2, p. 021102, 2020.

[56] Y. K. Shin, L. Gai, S. Raman, and A. C. T. van Duin, "Development of a ReaxFF Reactive Force Field for the Pt–Ni Alloy Catalyst," *The Journal of Physical Chemistry A*, vol. 120, no. 41, pp. 8044–8055, 2016.

[57] D. Porezag, T. Frauenheim, T. Köhler, G. Seifert, and R. Kaschner, "Construction of tight-binding-like potentials on the basis of density-functional theory: Application to carbon," *Physical Review B*, vol. 51, pp. 12947–12957, May 1995.

[58] S. Grimme, C. Bannwarth, and P. Shushkov, "A robust and accurate tight-binding quantum chemical method for structures, vibrational frequencies, and noncovalent interactions of large molecular systems parametrized for all spd-block elements (z= 1–86)," *Journal of Chemical Theory and Computation*, vol. 13, no. 5, pp. 1989–2009, 2017.

[59] C. Bannwarth, S. Ehlert, and S. Grimme, "GFN2-xTB— An accurate and broadly parametrized self-consistent tight-binding quantum chemical method with multipole electrostatics and density-dependent dispersion contributions," *Journal of Chemical Theory and Computation*, vol. 15, no. 3, pp. 1652–1671, 2019.

[60] S. Spicher and S. Grimme, "Robust atomistic modeling of materials, organometallic, and biochemical systems," *Angewandte Chemie International Edition*, vol. 132, pp. 2–11, 2020.

[61] O. K. Andersen and O. Jepsen, "Explicit, First-Principles Tight-Binding Theory," *Physical Review Letters*, vol. 53, pp. 2571–2574, Dec 1984.

[62] P. Koskinen and V. Mäkinen, "Density-functional tight-binding for beginners," *Computational Materials Science*, vol. 47, no. 1, pp. 237–253, 2009.

[63] B. Aradi, B. Hourahine, and T. Frauenheim, "DFTB+, a Sparse Matrix-Based Implementation of the DFTB Method," *The Journal of Physical Chemistry A*, vol. 111, no. 26, pp. 5678–5684, 2007.

[64] S. Grimme and C. Bannwarth, "Ultra-fast computation of electronic spectra for large systems by tight-binding based simplified Tamm-Dancoff approximation (sTDA-xTB)," *The Journal of Chemical Physics*, vol. 145, no. 5, p. 054103, 2016.

[65] S. Grimme, J. Antony, S. Ehrlich, and H. Krieg, "A consistent and accurate ab initio parametrization of density functional dispersion correction (DFT-D) for the 94 elements H-Pu," *The Journal of Chemical Physics*, vol. 132, no. 15, p. 154104, 2010.

[66] A. S. Christensen, T. Kubař, Q. Cui, and M. Elstner, "Semiempirical Quantum Mechanical Methods for Noncovalent Interactions for Chemical and Biochemical Applications," *Chemical Reviews*, vol. 116, no. 9, pp. 5301–5337, 2016.

[67] B. Axilrod and E. Teller, "Interaction of the van der Waals Type Between Three Atoms," *The Journal of Chemical Physics*, 1943.

[68] Y. Muto, "Force between nonpolar molecules," *Journal of the Physico-Mathematical Society of Japan*, vol. 17, pp. 629–631, 1943.

[69] E. Caldeweyher, S. Ehlert, A. Hansen, H. Neugebauer, S. Spicher, C. Bannwarth, and S. Grimme, "A generally applicable atomic-charge dependent london dispersion correction," *The Journal of Chemical Physics*, vol. 150, no. 15, p. 154122, 2019.

[70] P. Hohenberg and W. Kohn, "Density functional theory (DFT)," *Physical Review*, vol. 136, p. B864, 1964.

[71] W. Kohn and L. J. Sham, "Self-Consistent Equations Including Exchange and Correlation Effects," *Physical Review*, p. A1133, 1965.

[72] F. Jensen, *Introduction to Computational Chemistry*. John wiley & sons, 2008.

[73] A. D. Becke, "Density-functional thermochemistry. iii. the role of exact exchange," *The Journal of Chemical Physics*, vol. 98, no. 7, pp. 5648–5652, 1993.

[74] A. D. Becke, "Density-functional exchange-energy approximation with correct asymptotic behavior," *Physical Review A*, vol. 38, no. 6, p. 3098, 1988.

[75] C. Lee, W. Yang, and R. G. Parr, "Development of the colle-salvetti correlation-energy formula into a functional of the electron density," *Physical Review B*, vol. 37, no. 2, p. 785, 1988.

[76] C. Møller and M. S. Plesset, "Note on an approximation treatment for many-electron systems," *Physical Review*, vol. 46, no. 7, p. 618, 1934.

[77] J. Tersoff and D. R. Hamann, "Theory of the scanning tunneling microscope," *Physical Review B*, vol. 31, pp. 805–813, 1985.

[78] J. Tersoff and D. R. Hamann, "Theory and Application for the Scanning Tunneling Microscope," *Physical Review Letters*, vol. 50, pp. 1998–2001, 1983.

[79] C. Witt, J. M. Dieterich, and B. Hartke, "Cluster structures influenced by interaction with a surface," *Physical Chemistry Chemical Physics (Incorporating Faraday Transactions)*, vol. 20, pp. 15661–15670, Jan. 2018.

[80] M. Elstner, D. Porezag, G. Jungnickel, J. Elsner, M. Haugk, T. Frauenheim, S. Suhai, and G. Seifert, "Self-consistent-charge density-functional tight-binding method for simulations of complex materials properties," *Physical Review B*, vol. 58, no. 11, p. 7260, 1998.

[81] M. Gaus, A. Goez, and M. Elstner, "Parametrization and benchmark of DFTB3 for organic molecules," *Journal of Chemical Theory and Computation*, vol. 9, no. 1, pp. 338–354, 2013.

[82] W. Humphrey, A. Dalke, and K. Schulten, "VMD: Visual molecular dynamics," *Journal of Molecular Graphics*, vol. 14, no. 1, pp. 33–38, 1996.

[83] W. Liu, V. G. Ruiz, G.-X. Zhang, B. Santra, X. Ren, M. Scheffler, and A. Tkatchenko, "Structure and energetics of benzene adsorbed on transition-metal surfaces: density-functional theory with van der waals interactions including collective substrate response," *New Journal of Physics*, vol. 15, no. 5, p. 053046, 2013.

[84] W. Liu, A. Tkatchenko, and M. Scheffler, "Modeling adsorption and reactions of organic molecules at metal surfaces," *Accounts of Chemical Research*, vol. 47, no. 11, pp. 3369–3377, 2014.

[85] P. Hobza, H. Selzle, and E. Schlag, "Structure and Properties of Benzene-Containing Molecular Clusters - Nonempirical Ab-Initio Calculations and Experiments," *Chemical Reviews*, vol. 94, no. 7, pp. 1767–1785, 1994.

[86] A. S. Mahadevi, A. P. Rahalkar, S. R. Gadre, and G. N. Sastry, "Ab initio investigation of benzene clusters: Molecular tailoring approach," *The Journal of Chemical Physics*, vol. 133, no. 16, p. 164308, 2010.

[87] M. Saeys, M.-F. Reyniers, G. B. Marin, and M. Neurock, "Density Functional Study of Benzene Adsorption on Pt(111)," *The Journal of Physical Chemistry B*, vol. 106, no. 30, pp. 7489–7498, 2002.

[88] A. Vargas, T. Bürgi, and A. Baiker, "Adsorption of activated ketones on platinum and their reactivity to hydrogenation: A DFT study," *Journal of Catalysis*, vol. 222, no. 2, pp. 439–449, 2004.

[89] M. C. Schmidt, S. Attia, C. Schroeder, A.-K. Baumann, P. Pessier, and S. Schauermann, "Temperature dependent formation of acetophenone oligomers accompanied by keto-enol tautomerism: Real space distribution," *The Journal of Physical Chemistry C*, 2020.

[90] S. Attia, M. C. Schmidt, C. Schröder, and S. Schauermann, "Formation and Stabilization Mechanisms of Enols on Pt through Multiple Hydrogen Bonding," *ACS Catalysis*, vol. 9, no. 8, pp. 6882–6889, 2019.

[91] K. F. Garrity, J. W. Bennett, K. M. Rabe, and D. Vanderbilt, "Pseudopotentials for high-throughput DFT calculations," *Computational Materials Science*, vol. 81, pp. 446–452, 2014.

[92] P. Giannozzi, O. Baseggio, P. Bonfà, D. Brunato, R. Car, I. Carnimeo, C. Cavazzoni, S. de Gironcoli, P. Delugas, F. Ferrari Ruffino, A. Ferretti, N. Marzari, I. Timrov, A. Urru, and S. Baroni, "Quantum ESPRESSO toward the exascale," *The Journal of Chemical Physics*, vol. 152, no. 15, p. 154105, 2020.

[93] D. Ferri, T. Bürgi, and A. Baiker, "Conformational isomerism of α-ketoesters. A FTIR and ab initio study," *Journal of the Chemical Society, Perkin Transactions 2*, no. 2, pp. 221–227, 2000.

[94] T. Bürgi, F. Atamny, R. Schlögl, and A. Baiker, "Adsorption of ethyl pyruvate on Pt (111) studied by XPS and UPS," *The Journal of Physical Chemistry B*, vol. 104, no. 25, pp. 5953–5960, 2000.

[95] C. Schröder, M. C. Schmidt, C. Witt, S. Attia, J. Weber, A.-K. Baumann, B. Hartke, and S. Schauermann, "Tuning the strength of molecular bonds in oxygenates via surface-assisted intermolecular interactions: Atomistic insights," *The Journal of Physical Chemistry C*, 2020.

[96] B. R. Galvão, L. P. Viegas, D. R. Salahub, and M. P. Lourenço, "Reliability of semiempirical and DFTB methods for the global optimization of the structures of nanoclusters," *Journal of Molecular Modeling*, vol. 26, no. 11, pp. 1–8, 2020.

[97] "https://www.ogolem.org/manual/, accessed Nov 20th 2020."

[98] "xtb-docs.readthedocs.io, accessed Nov 20th 2020."

A | Appendix

A.1 Supporting Information for Tuning the strength of molecular bond in oxygenates via surface-assisted intermolecular interactions: atomistic insights

Supporting information for the manuscript

Tuning the strength of molecular bonds in oxygenates via surface-assisted intermolecular interactions: atomistic insights

Carsten Schröder, Marvin C. Schmidt, Christopher Witt, Smadar Attia, Jann Weber, Ann-Katrin Baumann, Bernd Hartke and Swetlana Schauermann*

Institut für Physikalische Chemie, Christian-Albrechts-Universität zu Kiel

Max-Eyth-Str. 2, 24118 Kiel, Germany

1. TABLE S1: Assignment of vibrational modes of ethyl pyruvate

The assignment of the vibrational bands was performed based on the theoretically computed spectrum as well as experimentally measured spectra of isotopically labelled ^{13}C-EP. The references cited in the table demonstrate that the assignment performed in this study is in agreement with the previously published one.

Frequency cm^{-1}					**Assignment**	**Ref.**
^{12}C		**^{13}C**		**B3LYP**		
Sub-monolayer [95 K]	Multilayer [95 K]	Sub-monolayer [95 K]	Multilayer [95 K]	aug-cc-pVTZ scaled (f=0.9858)		
2988 2972	2987 2981	2989 2974	2986 2978	3104 - 2996	ν(C-H)$_x$	[8]
1530	1753	1529	1750	1739	ν(C=O)$_{ester}$	[9]
	1741		1701	1775	ν(C=O)$_{acetyl}$	[10]
	1476		1474	1477	δ_{as}(**CH$_2$**-CH$_3$)	[8, 11]
1465	1465	1460	1460	1464	δ_s(**CH$_2$**-CH$_3$)	[11]
1444	1447	1442	1445	1440	δ_{as}(CH$_2$-**CH$_3$**)	[8, 10-13]
1428	1424	1428	1426	1436	δ_{as}(CH$_3$)	[10-11]
	1360		1360	1373	δ_s(CH$_3$)	[8, 10, 13-14]
1296 1268	1313	1296 1268	1306	1290	ν(C-O)$_{ester,1}$ ν(C-O)$_{ester,2}$	[10, 13]
	1162		1143	1150	ν_{mixed}(C-C-C)	
	1116		1116	1118	ρ(O-C$_2$H$_5$)	[10]
1020	1028	1018	1027	1026	ρ(C$_2$H$_5$)/ν(C-C)	[8]
1006	1010	1002	1010	1024	ν(C-C)	[10, 13]
	975		975	965	ρ(CH$_3$)	[12]

2. Graphical illustration of the calculated mixed mode vibration at 1150 cm^{-1} of gaseous ethyl pyruvate.

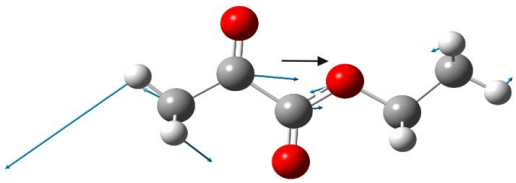

Figure 1_SI. Graphical illustration of the calculated mixed mode vibration at 1150 cm^{-1} of gaseous ethyl pyruvate. Blue arrows show the displacement vectors of the atoms participating in the vibration. The resulting dynamic dipole moment vector lies in the C-C-C-O plane is shown as a black arrow.

3. Full experimental details for Figures 2-5.

Figure 2. IRAS spectra of EP adsorbed on Pt(111) at 100 K obtained after dosing of EP at a flux of $7.2 \cdot 10^{12}$ molecules$\cdot s^{-1} \cdot cm^{-2}$. The spectra were obtained for (a) increasing EP exposure: (1) $1.4 \cdot 10^{13}$, (3) $4.3 \cdot 10^{13}$, (3) $7.2 \cdot 10^{13}$, (4) $1.0 \cdot 10^{14}$, (5) $1.1 \cdot 10^{14}$, (6) $1.3 \cdot 10^{14}$ molecules$\cdot cm^{-2}$; and (b) during in-situ H_2 exposure at a constant coverage of EP. The initial coverage of EP (spectrum 1) amounts to $7.2 \cdot 10^{13}$ molecules$\cdot cm^{-2}$. The spectra (2)-(5) were acquired after H_2 exposures indicated on the right side of (b).

Figure 3. (a) STM image of EP adsorbed on pristine Pt(111) (exposure at 135 K, acquisition temperature 118 K, 611 mV, 0.267 nA, 52.2×52.2 nm^2). (b) Close-up images of different oligomers divided in $S1_{(STM)}$ (dimers D1, D2 and D3) and $S2_{(STM)}$ (dimer D4, trimers T1 and T2, tetramers O1 and O2) species. Note that the dimer D4 was observed only on H-covered Pt(111) surface.

Figure 4. (a) STM images (37.3×37.3 nm^2) of EP adsorbed on pristine Pt(111) at different coverages. The images were obtained at 105 – 120 K for the following surface coverages of EP: (I) $1.8 \cdot 10^{12}$, (II) $10.5 \cdot 10^{12}$, (III) $13.5 \cdot 10^{12}$, (IV) $70.7 \cdot 10^{12}$ molecules$\cdot cm^{-2}$. Imaging conditions: 130 – 800 mV, typical tunnelling currents of 0.1 - 0.5 nA. (b) Absolute number of two types of surface species $S1_{(STM)}$ and $S2_{(STM)}$ shown for different EP surface coverages. (c) Relative abundance of two types of surface species $S1_{(STM)}$ and $S2_{(STM)}$ shown for different EP surface coverages. In both cases, statistical evaluation was done for an area larger than shown in (a) (52.2×52.2 nm^2)

Figure 5 (a) STM images (32.9×32.9 nm^2) of EP adsorbed on Pt(111) obtained after different H_2 exposures indicated on the horizontal axis. The images were obtained at 110 K after the exposure to EP followed by in situ H_2 exposure in the STM chamber. Imaging conditions: 127-144 mV, typical tunnelling currents of 0.2 - 0.3 nA. (b) Relative abundance of two types of surface species $S1_{(STM)}$ and $S2_{(STM)}$ shown for different H_2 exposures. Statistical evaluation was done for an area larger than shown in (a) (52.2×52.2 nm^2)

REFERENCES

1. Attia, S.; Spadafora, E. J.; Hartmann, J.; Freund, H.-J.; Schauermann, S., Molecular Beam/Infrared Reflection-Absorption Spectroscopy Apparatus for Probing Heterogeneously Catalyzed Reactions on Functionalized and Nanostructured Model Surfaces. *Rev. Sci. Instrum.* **2019**, *90*, 053903.
2. Giannozzi, P., et al., Advanced Capabilities for Materials Modelling with Quantum Espresso. *J. Phys.: Condens. Matter* **2017**, *29*, 465901.
3. Giannozzi, P., et al., Quantum Espresso: A Modular and Open-Source Software Project for Quantum Simulations of Materials. *J. Phys.: Condens. Matter* **2009**, *21*, 395502.
4. Perdew, J. P.; Burke, K.; Ernzerhof, M., Generalized Gradient Approximation Made Simple. *Phys. Rev. Lett.* **1996**, *77*, 3865-3868.
5. Dal Corso, A., Pseudopotentials Periodic Table: From H to Pu. *Comput. Mater. Sci.* **2014**, *95*, 337-350.
6. Tersoff, J.; Hamann, D. R., Theory of the Scanning Tunneling Microscope. *Phys. Rev. B* **1985**, *31*, 805-813.
7. Frisch, M. J., et al. *Gaussian 16 Rev. C.01*, Wallingford, CT, 2016.
8. Maes, I. I.; Herrebout, W. A.; van der Veken, B. J., Vibrational Conformational Analysis of Ethyl Formate. *J. Ram. Spec.* **1994**, *25*, 679-691.
9. Demers-Carpentier, V.; Rasmussen, A. M. H.; Goubert, G.; Ferrighi, L.; Dong, Y.; Lemay, J.-C.; Masini, F.; Zeng, Y.; Hammer, B.; McBreen, P. H., Stereodirection of an A-Ketoester at Sub-Molecular Sites on Chirally Modified Pt(111): Heterogeneous Asymmetric Catalysis. *J. Amer. Chem. Soc.* **2013**, *135*, 9999-10002.
10. Burkholder, L.; Tysoe, W. T., Structure and Reaction Pathways of Methyl Pyruvate on Pd(111). *J. Phys. Chem. C* **2009**, *113*, 15298-15306.
11. Nolin, B.; Jones, R. N., The Infrared Absorption Spectra of Deuterated Esters: I. Methyl Acetate. *Can. J. Chem.* **1956**, *34*, 1382-1391.
12. George, W. O.; Houston, T. E.; Harris, W. C., Vibrational Spectra and Structure of Esters—I. Infrared and Raman Spectra of CH_3COOCH_3, CH_3COOCD_3, CD_3COOCH_3 and CD_3COOCD_3. *Spectrochim. Acta A: Mol. Spec.* **1974**, *30*, 1035-1057.
13. Castonguay, M.; Roy, J. R.; Rochefort, A.; McBreen, P. H., Orientation and Conformation of Methyl Pyruvate on Ni(111). *J. Amer. Chem. Soc.* **2000**, *122*, 518-524.
14. Burkholder, L.; Tysoe, W. T., Structure and Reaction Pathways of Methyl Lactate on Pd(111). *Surf. Sc.* **2009**, *603*, 2714-2720.
15. Attia, S.; Schauermann, S., Coverage-Dependent Adsorption Geometry of Acetophenone on Pt(111). *J. Phys. Chem. C* **2020**, *124*, 557-566.
16. Attia, S.; Schmidt, M.-C.; Schröder, C.; Pessier, P.; Schauermann, S., Surface-Driven Keto–Enol Tautomerization: Atomistic Insights into Enol Formation and Stabilization Mechanisms. *Angew. Chem. Int. Edit.* **2018**, *57*, 16659-16664.

A.2 Global Optimization Example Input

A global optimization as done in this work requires the following input files:

- A *.ogo file for OGOLEM.
- A *.xyz file for the molecule and the surface, respectively.
- An xcontrol file, describing which atoms to fix.

The *.ogo file can look like this for an optimization with GFN-FF:

```
###OGOLEM###
DebugLevel=42
GlobOptAlgo=cluster{xover(multiple:10%vinland:mode=surface,moveperstep=0.2,maxmoves
LocOptAlgo=xtb:method=gfn-ff,xcontrol=fix.surf
PoolSize=20
NumberOfGlobIterations=20000
GrowCell=false
CellSize=25;25;25
BlowFacDissoc=3.5
BlowInitialBonds=1.45
BlowBondDetect=1.45
CollisionDetection=simplepairwise
DiversityCheck=percfitnessbased:0.03
GeometryChoice=fitnessrankbased:bothfitness,gausswidth1=0.5,gausswidth2=0.01
ThreshLocOptGradient=1E-7
PostSanityCD=true
PostSanityDD=true
GeneticRecordsToSerial=10000
GeometriesToSerial=10000
<GEOMETRY>
NumberOfParticles=2
<MOLECULE>
MoleculeRepetitions=2
MoleculePath=ethylpyruvate.xyz
</MOLECULE>
</GEOMETRY>
<ENVIRONMENT>
EnvironmentCartes=pt111_5x5_sorted.xyz
```

```
EnvironmentKind=simpleenvironment
ReferencePoints=35;53;59
AllowedSpace=halfspherespace:0.0,0.0,0.0;9.0
BlowFacEnvInit=0.9
</ENVIRONMENT>
```

Most of these keywords are used for controlling the global optimization setup itself. The part encased by ⟨GEOMETRY⟩ describes the molecules that are to be optimized, while the part encased by ⟨ENVIRONMENT⟩ describes the surface[1]. For GFN-FF optimizations an xcontrol file may be used to hold the surface fixed. In this example the xcontrol file has the following content:

```
$fix
   elements: Pt
$end
```

More options for fixing atoms are given in the xTB online manual [98] in the "Detailed Input" section.

A.3 Full tables for ethyl pyruvate dimer data

Table A.1: Full table of ethyl pyruvate dimer distances and angles.

Filename	E_{tot}	COM distance / Å	Angle / °
workdir/ethylpyruvate_at_pt111.1/rank0individual70659.xyz	-32471.5621	6.326146627532364	13.40380587514173
workdir/ethylpyruvate_at_pt111.1/rank1individual35226.xyz	-32448.2620	8.056261433751004	166.3595675754906
workdir/ethylpyruvate_at_pt111.1/rank2individual6339.xyz	-32431.3019	7.604812330499141	120.74533485374036
workdir/ethylpyruvate_at_pt111.1/rank3individual69747.xyz	-32417.7973	4.441494060787305	9.054347977859456
workdir/ethylpyruvate_at_pt111.1/rank4individual56120.xyz	-32410.0875	4.909594550589581	161.7885113726111
workdir/ethylpyruvate_at_pt111.1/rank5individual3089.xyz	-32403.1360	4.617713824999868	172.2928724010728
workdir/ethylpyruvate_at_pt111.1/rank6individual54265.xyz	-32396.3780	8.233492300441537	162.90777138346903
workdir/ethylpyruvate_at_pt111.1/rank7individual54945.xyz	-32392.8207	8.030708364755997	91.89257565934349
workdir/ethylpyruvate_at_pt111.1/rank8individual2983.xyz	-32379.8735	6.44582891010129	162.05831371217462
workdir/ethylpyruvate_at_pt111.1/rank9individual52145.xyz	-32367.7365	7.4387784189510535	146.9529821951671
workdir/ethylpyruvate_at_pt111.1/rank10individual26601.xyz	-32356.1576	5.598962488059518	98.55032730902752
workdir/ethylpyruvate_at_pt111.1/rank11individual68732.xyz	-32341.7738	5.256490381342559	148.05596194925906
workdir/ethylpyruvate_at_pt111.1/rank12individual31866.xyz	-32315.9116	6.791993786611863	110.61531656965839
workdir/ethylpyruvate_at_pt111.1/rank13individual10982.xyz	-32309.7171	6.980254847189523	66.45339853075049
workdir/ethylpyruvate_at_pt111.1/rank14individual5031.xyz	-32299.9660	5.913529642846762	155.69345562294623
workdir/ethylpyruvate_at_pt111.1/rank15individual263.xyz	-32288.9153	4.23163369229529	84.38002872872535
workdir/ethylpyruvate_at_pt111.1/rank16individual85414.xyz	-32284.1633	6.588005070268523	62.20324053656668
workdir/ethylpyruvate_at_pt111.1/rank17individual69482.xyz	-32260.8003	6.472560005724991	155.46026193939227
workdir/ethylpyruvate_at_pt111.1/rank18individual36521.xyz	-32225.7281	7.5964780922884465	105.93450034155435
workdir/ethylpyruvate_at_pt111.1/rank19individual52579.xyz	-32216.8333	6.7940188240348105	150.23479005960687
workdir/ethylpyruvate_at_pt111.2/rank0individual98921.xyz	-33007.5007	10.935977235769972	176.75893288438115
workdir/ethylpyruvate_at_pt111.2/rank1individual88615.xyz	-32804.5395	7.531333272947113	113.0412599010888
workdir/ethylpyruvate_at_pt111.2/rank2individual92746.xyz	-32758.6161	9.914557751802185	20.686941703009456
workdir/ethylpyruvate_at_pt111.2/rank3individual40770.xyz	-32697.5358	7.924448230846278	147.92067144504549
workdir/ethylpyruvate_at_pt111.2/rank4individual40587.xyz	-32604.2856	8.347922673765853	176.0667413130713
workdir/ethylpyruvate_at_pt111.2/rank5individual55697.xyz	-32521.3251	4.884410662874251	128.15339611601968
workdir/ethylpyruvate_at_pt111.2/rank6individual83884.xyz	-32500.8948	5.421276211309141	113.31190190118114
workdir/ethylpyruvate_at_pt111.2/rank7individual83985.xyz	-32472.4373	5.591023889267396	118.25201851322112
workdir/ethylpyruvate_at_pt111.2/rank8individual50608.xyz	-32434.7566	5.686251460918367	128.05313962615935
workdir/ethylpyruvate_at_pt111.2/rank9individual64680.xyz	-32413.1957	5.248337571988544	82.02906009407366

[1]More detailed descriptions of the Input keywords may be found in the Ogolem manual [97]

workdir/ethylpyruvate_at_pt111.2/rank10individual94988.xyz	-32400.6004	6.008392361576589	71.03606836728162
workdir/ethylpyruvate_at_pt111.2/rank11individual99373.xyz	-32390.3312	5.141374656948395	106.69861347163642
workdir/ethylpyruvate_at_pt111.2/rank12individual51898.xyz	-32383.0451	8.659467981410899	117.39361968462947
workdir/ethylpyruvate_at_pt111.2/rank13individual51127.xyz	-32378.7144	5.121063077413614	103.32995239531758
workdir/ethylpyruvate_at_pt111.2/rank14individual48828.xyz	-32373.3011	5.233399007691317	94.18245545530723
workdir/ethylpyruvate_at_pt111.2/rank15individual55830.xyz	-32369.2018	7.431204827453837	162.68618822726654
workdir/ethylpyruvate_at_pt111.2/rank16individual46071.xyz	-32365.8467	5.469830027466216	26.950685722546
workdir/ethylpyruvate_at_pt111.2/rank17individual28610.xyz	-32360.4269	5.6910019409367205	140.53815779556658
workdir/ethylpyruvate_at_pt111.2/rank18individual38957.xyz	-32355.3017	5.12546727114713	142.77949201535893
workdir/ethylpyruvate_at_pt111.2/rank19individual46809.xyz	-32352.0070	5.96155883968199	98.56587543085851
workdir/ethylpyruvate_at_pt111.3/rank0individual89583.xyz	-32785.8648	9.781660988185058	130.59280333679087
workdir/ethylpyruvate_at_pt111.3/rank1individual86470.xyz	-32678.4915	6.795654571615569	146.55327914668723
workdir/ethylpyruvate_at_pt111.3/rank2individual54167.xyz	-32639.9789	7.575207107221135	61.45187899508009
workdir/ethylpyruvate_at_pt111.3/rank3individual58190.xyz	-32621.8022	9.574713122191499	162.70469770957692
workdir/ethylpyruvate_at_pt111.3/rank4individual72815.xyz	-32615.4751	4.487436911989242	174.15398355850724
workdir/ethylpyruvate_at_pt111.3/rank5individual89172.xyz	-32569.0094	7.216994928712038	118.61924509303005
workdir/ethylpyruvate_at_pt111.3/rank6individual80831.xyz	-32524.1527	6.101649593441331	106.93137809097668
workdir/ethylpyruvate_at_pt111.3/rank7individual99499.xyz	-32509.9737	5.481312830487709	116.56234404694267
workdir/ethylpyruvate_at_pt111.3/rank8individual88319.xyz	-32468.3021	7.480773114809026	129.09890705947717
workdir/ethylpyruvate_at_pt111.3/rank9individual56703.xyz	-32421.5334	3.923827060410342	86.42018725145942
workdir/ethylpyruvate_at_pt111.3/rank10individual60108.xyz	-32413.9512	5.745379774932219	47.184545318927086
workdir/ethylpyruvate_at_pt111.3/rank11individual37209.xyz	-32399.0898	5.3323010573753145	150.82641431464728
workdir/ethylpyruvate_at_pt111.3/rank12individual67167.xyz	-32389.4148	5.105371228982088	137.03723689348587
workdir/ethylpyruvate_at_pt111.3/rank13individual60292.xyz	-32378.8214	5.333276046410429	76.57954278940514
workdir/ethylpyruvate_at_pt111.3/rank14individual92746.xyz	-32373.2133	8.048225197834041	60.62611753354282
workdir/ethylpyruvate_at_pt111.3/rank15individual25872.xyz	-32364.3595	8.388470973785816	38.683625366621634
workdir/ethylpyruvate_at_pt111.3/rank16individual89587.xyz	-32360.9997	9.440360909758192	174.4045218948967
workdir/ethylpyruvate_at_pt111.3/rank17individual72983.xyz	-32356.5179	5.012568230116333	150.17591844403677
workdir/ethylpyruvate_at_pt111.3/rank18individual26115.xyz	-32350.9399	7.178265724608085	126.28614269007217
workdir/ethylpyruvate_at_pt111.3/rank19individual67374.xyz	-32343.6598	7.054943430891859	36.27706836102643
workdir/ethylpyruvate_at_pt111.4/rank0individual12786.xyz	-32786.4786	8.588156337489742	111.610432244898
workdir/ethylpyruvate_at_pt111.4/rank1individual81322.xyz	-32701.8859	6.100015675786429	123.615659430463
workdir/ethylpyruvate_at_pt111.4/rank2individual44303.xyz	-32673.5994	6.070124859505269	126.61962015155235
workdir/ethylpyruvate_at_pt111.4/rank3individual18113.xyz	-32670.1312	6.036122656578654	75.44713323615724
workdir/ethylpyruvate_at_pt111.4/rank4individual26416.xyz	-32666.1334	6.641521859159913	83.46601834636677
workdir/ethylpyruvate_at_pt111.4/rank5individual27560.xyz	-32660.4456	5.836677490258163	64.13555061252625
workdir/ethylpyruvate_at_pt111.4/rank6individual47754.xyz	-32649.1169	4.937765479983238	138.3029159400553
workdir/ethylpyruvate_at_pt111.4/rank7individual18457.xyz	-32643.7513	4.854191563000551	147.15067610052546
workdir/ethylpyruvate_at_pt111.4/rank8individual71599.xyz	-32637.8227	4.3567284528039405	80.49475766649397
workdir/ethylpyruvate_at_pt111.4/rank9individual76358.xyz	-32625.2942	4.908892042146852	110.11677690268081
workdir/ethylpyruvate_at_pt111.4/rank10individual97183.xyz	-32621.2299	4.820495237705831	107.14809445336809
workdir/ethylpyruvate_at_pt111.4/rank11individual24963.xyz	-32615.7314	7.007686770316332	132.93365549485753
workdir/ethylpyruvate_at_pt111.4/rank12individual54016.xyz	-32610.1503	4.384086340723369	61.84391877582529
workdir/ethylpyruvate_at_pt111.4/rank13individual18064.xyz	-32604.5921	7.013614557903743	84.69078552452756
workdir/ethylpyruvate_at_pt111.4/rank14individual18512.xyz	-32600.2956	4.513318035626462	113.88189915721874
workdir/ethylpyruvate_at_pt111.4/rank15individual99227.xyz	-32595.8017	6.124768623281098	138.01533427649116
workdir/ethylpyruvate_at_pt111.4/rank16individual41454.xyz	-32583.0895	8.847159875956116	156.4600502194217
workdir/ethylpyruvate_at_pt111.4/rank17individual65712.xyz	-32578.1942	8.51456170490642	140.2159048088635
workdir/ethylpyruvate_at_pt111.4/rank18individual31265.xyz	-32574.5844	5.460196515704626	109.06808066832092
workdir/ethylpyruvate_at_pt111.4/rank19individual33321.xyz	-32562.2363	5.942794513280081	55.7981029873431
workdir/ethylpyruvate_at_pt111.5/rank0individual29389.xyz	-32635.6954	8.644456667599169	77.92110717457635
workdir/ethylpyruvate_at_pt111.5/rank1individual67119.xyz	-32618.1265	4.90304312877531	113.14978528192103
workdir/ethylpyruvate_at_pt111.5/rank2individual96394.xyz	-32613.4290	6.756625715255576	103.39878288276982
workdir/ethylpyruvate_at_pt111.5/rank3individual93257.xyz	-32605.9184	6.952668678626309	102.81431500391025
workdir/ethylpyruvate_at_pt111.5/rank4individual91055.xyz	-32600.9694	7.070529644011659	41.84464011486121
workdir/ethylpyruvate_at_pt111.5/rank5individual40539.xyz	-32592.4575	8.26089782723372	91.97945863553132
workdir/ethylpyruvate_at_pt111.5/rank6individual74321.xyz	-32562.6433	6.429228942041435	83.5445112911864
workdir/ethylpyruvate_at_pt111.5/rank7individual50704.xyz	-32556.8512	4.8343690236474615	159.9059391313305
workdir/ethylpyruvate_at_pt111.5/rank8individual69202.xyz	-32551.6942	6.937230683013701	107.56723191307948
workdir/ethylpyruvate_at_pt111.5/rank9individual59940.xyz	-32547.1746	8.07893799738643	135.49985912818983
workdir/ethylpyruvate_at_pt111.5/rank10individual70366.xyz	-32538.4942	4.548705597032945	103.55744146283482
workdir/ethylpyruvate_at_pt111.5/rank11individual78411.xyz	-32533.2602	6.882176120539386	149.41685870423115
workdir/ethylpyruvate_at_pt111.5/rank12individual50462.xyz	-32509.5045	4.2599992409587415	47.88150801109505
workdir/ethylpyruvate_at_pt111.5/rank13individual85902.xyz	-32504.1161	8.049513243736238	139.1566391617858
workdir/ethylpyruvate_at_pt111.5/rank14individual47647.xyz	-32494.5513	4.397681298645167	139.847523822608
workdir/ethylpyruvate_at_pt111.5/rank15individual93121.xyz	-32490.6273	5.136054083413098	51.44342866422558
workdir/ethylpyruvate_at_pt111.5/rank16individual57468.xyz	-32480.1146	5.562550891403685	76.68445647688047
workdir/ethylpyruvate_at_pt111.5/rank17individual70146.xyz	-32468.7277	5.242687043095637	61.54309051994173
workdir/ethylpyruvate_at_pt111.5/rank18individual81652.xyz	-32437.4823	5.3091121395323455	156.185219210641
workdir/ethylpyruvate_at_pt111.5/rank19individual57268.xyz	-32433.5998	8.606593778537997	66.36559524266585
workdir/ethylpyruvate_at_pt111.6/rank0individual35570.xyz	-32954.2032	7.587505821847836	59.22290647397377
workdir/ethylpyruvate_at_pt111.6/rank1individual10884.xyz	-32642.3184	7.253015228350482	116.98723494592667
workdir/ethylpyruvate_at_pt111.6/rank2individual22889.xyz	-32573.5227	7.8212107058626	137.24524307028284
workdir/ethylpyruvate_at_pt111.6/rank3individual13467.xyz	-32529.9951	5.860841211698005	94.30388276551402
workdir/ethylpyruvate_at_pt111.6/rank4individual7429.xyz	-32475.3089	4.376203894949614	83.91996927722103
workdir/ethylpyruvate_at_pt111.6/rank5individual40892.xyz	-32459.1260	7.153371692865916	89.39079592412061

workdir/ethylpyruvate_at_pt111.6/rank6individual38299.xyz	-32412.7494	7.325687948672761	120.67037121125819
workdir/ethylpyruvate_at_pt111.6/rank7individual90026.xyz	-32394.9752	6.454977840972652	131.01220208972896
workdir/ethylpyruvate_at_pt111.6/rank8individual96622.xyz	-32377.4764	5.9894875722789775	57.13417040048242
workdir/ethylpyruvate_at_pt111.6/rank9individual75929.xyz	-32361.6739	5.238021163287622	89.52512127458446
workdir/ethylpyruvate_at_pt111.6/rank10individual86776.xyz	-32354.4113	5.559025436312794	125.3718717530719
workdir/ethylpyruvate_at_pt111.6/rank11individual38725.xyz	-32345.3496	9.57310642429557	135.09007981257108
workdir/ethylpyruvate_at_pt111.6/rank12individual65888.xyz	-32340.6023	6.94025952942539	124.00527414384565
workdir/ethylpyruvate_at_pt111.6/rank13individual2306.xyz	-32333.3053	7.296911849799128	147.11829221434863
workdir/ethylpyruvate_at_pt111.6/rank14individual66440.xyz	-32327.7296	5.1263597157776895	86.95591276360828
workdir/ethylpyruvate_at_pt111.6/rank15individual42813.xyz	-32324.4350	5.32528087384191	167.64621050619155
workdir/ethylpyruvate_at_pt111.6/rank16individual63898.xyz	-32311.9749	4.981483640907558	160.28199595091124
workdir/ethylpyruvate_at_pt111.6/rank17individual30253.xyz	-32307.0982	8.473705795397555	95.86847548320834
workdir/ethylpyruvate_at_pt111.6/rank18individual3854.xyz	-32290.8819	6.211350284023602	118.23750050408584
workdir/ethylpyruvate_at_pt111.6/rank19individual60597.xyz	-32287.2776	4.852506675927054	55.61674764056588
workdir/ethylpyruvate_at_pt111.7/rank0individual56078.xyz	-32414.8720	8.325298953398134	106.24369336404416
workdir/ethylpyruvate_at_pt111.7/rank1individual46485.xyz	-32397.9719	6.6961690463659265	162.2633001194179
workdir/ethylpyruvate_at_pt111.7/rank2individual35420.xyz	-32366.3704	6.484076254221387	34.038186977185894
workdir/ethylpyruvate_at_pt111.7/rank3individual38417.xyz	-32346.7534	8.566974434978894	135.11424251572612
workdir/ethylpyruvate_at_pt111.7/rank4individual52800.xyz	-32338.8659	7.9429916772659865	120.3818211525409
workdir/ethylpyruvate_at_pt111.7/rank5individual37013.xyz	-32286.8290	9.094798398274028	81.77515868287219
workdir/ethylpyruvate_at_pt111.7/rank6individual4215.xyz	-32257.3865	5.294486138857476	101.81392398876244
workdir/ethylpyruvate_at_pt111.7/rank7individual38568.xyz	-32232.1850	5.441492711641032	120.28482016584296
workdir/ethylpyruvate_at_pt111.7/rank8individual81155.xyz	-32216.7439	7.42506717084657	84.12036449811336
workdir/ethylpyruvate_at_pt111.7/rank9individual864.xyz	-32198.7157	6.727144749855902	138.32373995169604
workdir/ethylpyruvate_at_pt111.7/rank10individual41299.xyz	-32174.3018	8.892531251283685	35.18564596711978
workdir/ethylpyruvate_at_pt111.7/rank11individual603.xyz	-32167.1527	6.158312095419614	122.93855089377868
workdir/ethylpyruvate_at_pt111.7/rank12individual38999.xyz	-32163.7911	6.72486940866021	166.0774820736581
workdir/ethylpyruvate_at_pt111.7/rank13individual39069.xyz	-32151.7715	6.842682536839547	137.2936548500836
workdir/ethylpyruvate_at_pt111.7/rank14individual44060.xyz	-32147.4984	7.0349621173847545	154.9690599021796
workdir/ethylpyruvate_at_pt111.7/rank15individual54597.xyz	-32140.0276	6.85825503881436	55.001907620032654
workdir/ethylpyruvate_at_pt111.7/rank16individual71925.xyz	-32132.1753	8.397202585979237	17.084968155465056
workdir/ethylpyruvate_at_pt111.7/rank17individual79563.xyz	-32121.7525	9.99696385335667	139.91617769474618
workdir/ethylpyruvate_at_pt111.7/rank18individual34763.xyz	-32115.4807	9.610984334397306	147.31333826924293
workdir/ethylpyruvate_at_pt111.7/rank19individual20987.xyz	-32109.4847	7.802459607110492	126.38762974090906
workdir/ethylpyruvate_at_pt111.8/rank0individual9660.xyz	-32874.9889	7.236514265482202	167.19043097481944
workdir/ethylpyruvate_at_pt111.8/rank1individual20698.xyz	-32700.3902	7.570881443580535	147.27637771112921
workdir/ethylpyruvate_at_pt111.8/rank2individual40024.xyz	-32692.5944	6.150772346052841	60.14617304094791
workdir/ethylpyruvate_at_pt111.8/rank3individual94993.xyz	-32676.9260	8.218572821098919	154.53809856707704
workdir/ethylpyruvate_at_pt111.8/rank4individual27954.xyz	-32670.8629	5.8168297561378415	77.48749649390479
workdir/ethylpyruvate_at_pt111.8/rank5individual7532.xyz	-32647.5926	6.909225774550764	61.180081516922705
workdir/ethylpyruvate_at_pt111.8/rank6individual74436.xyz	-32643.7080	4.335040285988399	173.1988414187368
workdir/ethylpyruvate_at_pt111.8/rank7individual50868.xyz	-32631.9066	8.295978252126517	59.10001460438476
workdir/ethylpyruvate_at_pt111.8/rank8individual9924.xyz	-32604.7452	5.9429895117673	87.35300444440784
workdir/ethylpyruvate_at_pt111.8/rank9individual9063.xyz	-32597.9076	6.791977871274952	153.35887708276368
workdir/ethylpyruvate_at_pt111.8/rank10individual8305.xyz	-32592.3824	7.817729596005012	87.45297836654659
workdir/ethylpyruvate_at_pt111.8/rank11individual29173.xyz	-32586.8398	7.219920788985374	118.90069723216871
workdir/ethylpyruvate_at_pt111.8/rank12individual40003.xyz	-32581.9294	5.269282141266872	84.71815183502218
workdir/ethylpyruvate_at_pt111.8/rank13individual34974.xyz	-32569.2888	5.117932581013279	63.739664535388926
workdir/ethylpyruvate_at_pt111.8/rank14individual35285.xyz	-32553.7886	8.991940585367882	155.59790246568002
workdir/ethylpyruvate_at_pt111.8/rank15individual11651.xyz	-32547.6810	6.900072397780853	104.39528064305851
workdir/ethylpyruvate_at_pt111.8/rank16individual20996.xyz	-32526.1674	6.605483579647262	108.57733390593785
workdir/ethylpyruvate_at_pt111.8/rank17individual40959.xyz	-32510.2112	9.366783507835382	161.82229968768056
workdir/ethylpyruvate_at_pt111.8/rank18individual50952.xyz	-32505.2876	6.462555110087451	168.72981023680248
workdir/ethylpyruvate_at_pt111.8/rank19individual37436.xyz	-32491.7254	5.988547524251449	173.40099035582264
workdir/ethylpyruvate_at_pt111.9/rank0individual3309.xyz	-32661.9405	5.624861830984283	127.77652795525526
workdir/ethylpyruvate_at_pt111.9/rank1individual4173.xyz	-32651.8185	9.877404195509762	111.62976749417162
workdir/ethylpyruvate_at_pt111.9/rank2individual3779.xyz	-32633.9136	8.790612012081382	131.32826435318174
workdir/ethylpyruvate_at_pt111.9/rank3individual31973.xyz	-32563.7191	5.048492454336488	78.38110604832268
workdir/ethylpyruvate_at_pt111.9/rank4individual10715.xyz	-32467.2586	5.355566300924535	171.91017253925648
workdir/ethylpyruvate_at_pt111.9/rank5individual14826.xyz	-32432.7299	8.948444346283786	110.98050185916836
workdir/ethylpyruvate_at_pt111.9/rank6individual10107.xyz	-32419.1163	5.914914385801341	26.74546628694578
workdir/ethylpyruvate_at_pt111.9/rank7individual67066.xyz	-32392.5238	6.481540365969349	32.37660129133053
workdir/ethylpyruvate_at_pt111.9/rank8individual4529.xyz	-32377.5574	9.217755921139323	113.73301127127111
workdir/ethylpyruvate_at_pt111.9/rank9individual94446.xyz	-32362.0661	5.786784558640617	145.03878357409565
workdir/ethylpyruvate_at_pt111.9/rank10individual33685.xyz	-32333.8618	5.80003244746093	40.349784727263994
workdir/ethylpyruvate_at_pt111.9/rank11individual32085.xyz	-32324.2657	6.561245908814653	101.54791977571746
workdir/ethylpyruvate_at_pt111.9/rank12individual96787.xyz	-32316.1002	8.368254681088287	164.6338812273784
workdir/ethylpyruvate_at_pt111.9/rank13individual9187.xyz	-32311.7927	4.135329682169594	43.72200195617194
workdir/ethylpyruvate_at_pt111.9/rank14individual14682.xyz	-32304.6498	5.867109448954249	125.56934523862633
workdir/ethylpyruvate_at_pt111.9/rank15individual57925.xyz	-32288.0852	5.897034862906502	20.73501051467969
workdir/ethylpyruvate_at_pt111.9/rank16individual6222.xyz	-32267.0173	7.7756174719426046	91.77463280626003
workdir/ethylpyruvate_at_pt111.9/rank17individual20029.xyz	-32256.1332	6.298469592414644	158.37489807337914
workdir/ethylpyruvate_at_pt111.9/rank18individual28323.xyz	-32239.4519	7.569082504253697	92.62810766271876
workdir/ethylpyruvate_at_pt111.9/rank19individual14689.xyz	-32233.8972	7.696310509550709	99.95379667773054
workdir/ethylpyruvate_at_pt111.10/rank0individual10409.xyz	-32598.4569	8.940987182959718	124.5033147665768
workdir/ethylpyruvate_at_pt111.10/rank1individual90564.xyz	-32494.5059	8.213500795939707	94.36010559070421

workdir/ethylpyruvate_at_pt111.10/rank2individual62637.xyz	-32421.2261	5.819425015645126	94.52207895367702
workdir/ethylpyruvate_at_pt111.10/rank3individual17367.xyz	-32405.6474	9.062939391697634	148.79253524025154
workdir/ethylpyruvate_at_pt111.10/rank4individual16703.xyz	-32398.6544	7.613979714451637	155.2100660864976
workdir/ethylpyruvate_at_pt111.10/rank5individual80960.xyz	-32389.2771	7.492733505319402	114.4392217692984
workdir/ethylpyruvate_at_pt111.10/rank6individual61067.xyz	-32364.0814	6.5156666900702955	97.08092152414481
workdir/ethylpyruvate_at_pt111.10/rank7individual12541.xyz	-32351.4938	8.20573203745464	93.64230325042496
workdir/ethylpyruvate_at_pt111.10/rank8individual3238.xyz	-32347.7555	7.858471754926042	71.16469212348858
workdir/ethylpyruvate_at_pt111.10/rank9individual29738.xyz	-32342.4594	6.164751337120746	121.07455718195445
workdir/ethylpyruvate_at_pt111.10/rank10individual68764.xyz	-32338.7319	6.196933273050696	132.03766021788744
workdir/ethylpyruvate_at_pt111.10/rank11individual94349.xyz	-32331.9877	4.957493638137457	157.4289847347388
workdir/ethylpyruvate_at_pt111.10/rank12individual70417.xyz	-32328.5867	6.165514833985392	143.0696230340952
workdir/ethylpyruvate_at_pt111.10/rank13individual64291.xyz	-32315.3774	6.724638827698239	134.85900677372905
workdir/ethylpyruvate_at_pt111.10/rank14individual27840.xyz	-32311.8081	4.960717389340434	116.26287793975062
workdir/ethylpyruvate_at_pt111.10/rank15individual20471.xyz	-32303.9723	8.711634862569275	174.12167406230185
workdir/ethylpyruvate_at_pt111.10/rank16individual59890.xyz	-32300.2605	4.791054498372248	130.84470988259181
workdir/ethylpyruvate_at_pt111.10/rank17individual58340.xyz	-32287.5907	5.260129017043115	47.06082886296502
workdir/ethylpyruvate_at_pt111.10/rank18individual34190.xyz	-32283.0264	4.896178572047459	161.70944398529323
workdir/ethylpyruvate_at_pt111.10/rank19individual41163.xyz	-32274.3560	4.777068355281667	39.01378114854481

Declaration

I, Christopher Witt, hereby declare that the work presented in this thesis with the title ... was done by me regarding the content and form, under supervision of Prof. Dr. Bernd Hartke, with no other help than the cited sources. This is my first dissertation and the work has never been used in other dissertation attempts. I have never been deprived of any academic titles. This work complies to the rules of good scientific practice as proposed by the Deutsche Forschungsgesellschaft (DFG).

Kiel, November 2020

_____

Christopher Witt

Danksagung

An dieser Stelle möchte ich mir die Zeit nehmen, den Personen zu danken, ohne die diese Arbeit nicht möglich gewesen wäre. Zuallererst möchte ich Prof. Dr. Bernd Hartke für die Bereitstellung des Themas, die Betreuung und die Anstellung als Doktorand danken. Ich konnte mein Thema vollständig in Eigenregie bearbeiten, während er jederzeit für Nachfragen und Hilfestellungen verfügbar war. Einen besseren Betreuer könnte ich mir nicht vorstellen.

Desweiteren möchte ich Prof. Dr. Swetlana Schauermann und ihrem Arbeitskreis – insbesondere Carsten Schröder und Marvin Schmidt – für hilfreiche Besprechungen und den wissenschaftlichen Austausch im Allgemeinen danken.

Ebenso danke ich dem gesamten ehemaligen und jetzigen AK Hartke für die immer freundliche und positive Atmosphäre bei der Arbeit. Dabei kamen wissenschaftliche, politische, aber auch Freizeitgespräche nie zu kurz. Dabei möchte ich mich nochmal besonders bei meinen Bürokollegen Tim Raeker und Julien Steffen bedanken, die bei Schwierigkeiten oft mit Ratschlägen helfen konnten. Mit und neben euch zu arbeiten hat in all der Zeit immer Spaß gemacht.

Außerdem möchte ich meiner Familie für die finanzielle und mentale Unterstützung während des gesamten Studiums danken. Ohne euch wäre dies alles nie möglich gewesen.

Ich danke auch allen Freunden, die mich in all den Jahren meines Studiums begleitet und unterstützt haben.

Ein besonderer Dank gilt ebenfalls meinen Korrekturlesern: Meiner Frau Lydia Witt, Tim Raeker und Florian Spenke. Ohne euch wäre diese Arbeit sicherlich weniger verständlich gewesen. Ebenso danke ich hier allen anderen, die ihre Hilfe beim Korrekturlesen anboten.

Lydia danke ich besonders für die mentale Unterstützung während all der Jahre. Sie und unser Sohn Anton stellen den großen Ausgleich gegenüber der Arbeit für mich dar. – Ich freue mich schon darauf, dass wir bald zu viert sein werden!